Spring 2015

Asymptotic modelling of a thermopiezoelastic anisotropic smart plate

Yufei Long
Purdue University

Graduate School Form 30
Updated 1/15/2015

PURDUE UNIVERSITY
GRADUATE SCHOOL
Thesis/Dissertation Acceptance

This is to certify that the thesis/dissertation prepared

By Yufei Long

Entitled

ASYMPTOTIC MODELLING OF A THERMOPIEZOELASTIC ANISOTROPIC SMART PLATE

For the degree of Master of Science in Aeronautics and Astronautics

Is approved by the final examining committee:

Wenbin Yu
Chair

Vikas Tomar

Arun Prakash

To the best of my knowledge and as understood by the student in the Thesis/Dissertation Agreement, Publication Delay, and Certification Disclaimer (Graduate School Form 32), this thesis/dissertation adheres to the provisions of Purdue University's "Policy of Integrity in Research" and the use of copyright material.

Approved by Major Professor(s): Wenbin Yu

Approved by: Weinong Chen 4/22/2015

Head of the Departmental Graduate Program Date

ASYMPTOTIC MODELLING OF A THERMOPIEZOELASTIC ANISOTROPIC SMART PLATE

A Thesis

Submitted to the Faculty

of

Purdue University

by

Yufei Long

In Partial Fulfillment of the

Requirements for the Degree

of

Master of Science in Aeronautics and Astronautics

May 2015

Purdue University

West Lafayette, Indiana

ACKNOWLEDGMENTS

Although the study for the master's degree only lasts for two years, which is not a long time, I still want to acknowledge all the people who helped me during this period.

First of all I would like to thank my advisor, Professor Wenbin Yu, for his patient guidance, explanation, enlightening, and inspiration on my study. In addition to professional knowledge, Dr. Yu also imparts the methodology of research that benefits me a lot both during graduate study and in the future career.

I would also like to thank my other committee members, Dr. Vikas Tomar and Dr. Arun Prakash, who will take their valuable time to join my thesis defense as well as providing suggestions on improving the work.

Thanks also go to Dr. C. T. Sun and Dr. Vikas Tomar, whose classes established my fundamental knowledge for doing this work.

I am fortunate to be in Dr. Yu's research group, with a lot of colleagues, to whom I want to show my appreciation, who are delighted to share their experiences in graduate study.

Last but not least, I would like to appreciate my parent, providing me the opportunity to be educated and study abroad for a higher degree.

TABLE OF CONTENTS

Page

LIST OF TABLES v

LIST OF FIGURES vi

ABSTRACT x

1 Introduction 1
1.1 Motivation 1
1.1.1 Piezoelectric Plate Structures 1
1.1.2 Flexible Space Reflector 2
1.2 Previous Works 4
1.2.1 Piezoelectric Plate Modelling 4
1.2.2 Plate Modelling Based on Variational-Asymptotic Method . 7
1.3 Present Work and Outline 8

2 Fundamental Theories 11
2.1 Plate Kinematics 11
2.1.1 Deformation Configurations 11
2.1.2 3D Strain Field 14
2.2 Energy Formulation 17
2.2.1 Internal Potential Energy 17
2.2.2 Kinetic Energy 18
2.2.3 Virtual Work 20
2.3 Variational-Asymptotic Method 21

3 Dimensional Reduction 23
3.1 Order Assessment 23
3.2 Zeroth-Order Reduction 25
3.2.1 Reduction Formulation 25
3.2.2 Recovery Relations 31
3.3 First-Order Reduction 33
3.3.1 Reduction Formulation 34
3.3.2 Transformation to Reissner-Mindlin Model 40
3.3.3 Recovery Relations 43

4 Numerical Examples 47
4.1 Validation of the Zeroth-Order Model 47
4.1.1 Example 1: Two-Layered Simply-Supported Rectangular Plate 48
4.1.2 Example 2: Two-Layered Simply-Supported Circular Plate . 58

Page

4.2 Validation of the First-Order Model 67
4.2.1 Example 1: Three-Layered Simply-Supported Rectangular Plate 68
4.2.2 Example 2: Three-Layered Fixed Rectangular Plate 81

5 Summary 89

6 Recommendations 91

REFERENCES 92

LIST OF TABLES

Table Page

4.1 Material Properties of PVDF and Polyimide 49

4.2 Deflection of the center point of the plates (m) 63

4.3 Material Properties of PZT-4 and S glass/epoxy 69

LIST OF FIGURES

Figure Page

1.1 Piezoelectric actuator implementation. 3

1.2 Procedure of plate analysis using VAM. 9

2.1 Schematic of plate deformation. 12

4.1 Layup of the two-layered plate. 48

4.2 Geometry and boundary condition of a rectangular plate. 50

4.3 Deflection u_3 of the plate along $x_2 = 0.07$ m with electric load. 51

4.4 Distribution of strain Γ_{11} through thickness at the center with electric load. 51

4.5 Distribution of stress σ_{11} through thickness at the center with electric load. 52

4.6 Distribution of strain Γ_{22} through thickness at the center with electric load. 52

4.7 Distribution of stress σ_{22} through thickness at the center with electric load. 53

4.8 Distribution of strain Γ_{33} through thickness at the center with electric load. 53

4.9 Distribution of electric potential ϕ through thickness at the center with electric load. 54

4.10 Deflection u_3 of the plate along $x_2 = 0.07$ m with combined load. . . . 55

4.11 Distribution of strain Γ_{11} through thickness at the center with combined load. 55

4.12 Distribution of stress σ_{11} through thickness at the center with combined load. 56

4.13 Distribution of strain Γ_{22} through thickness at the center with combined load. 56

4.14 Distribution of stress σ_{22} through thickness at the center with combined load. 57

Figure Page

4.15 Distribution of strain Γ_{33} through thickness at the center with combined load. 57

4.16 Distribution of electric potential ϕ through thickness at the center with combined load. 58

4.17 Geometry and boundary condition of a circular plate. 59

4.18 Deflection u_3 of the plate along $\theta = \pi$ to $\theta = 0$ with electric load. . . . 60

4.19 Distribution of strain Γ_{11} through thickness at the center with electric load. 60

4.20 Distribution of stress σ_{11} through thickness at the center with electric load. 61

4.21 Distribution of strain Γ_{22} through thickness at the center with electric load. 61

4.22 Distribution of stress σ_{22} through thickness at the center with electric load. 62

4.23 Distribution of strain Γ_{33} through thickness at the center with electric load. 62

4.24 Distribution of electric potential ϕ through thickness at the center with electric load. 63

4.25 Deflection u_3 of the plate along $\theta = \pi$ to $\theta = 0$ with combined load. . . 64

4.26 Distribution of strain Γ_{11} through thickness at the center with combined load. 64

4.27 Distribution of stress σ_{11} through thickness at the center with combined load. 65

4.28 Distribution of strain Γ_{22} through thickness at the center with combined load. 65

4.29 Distribution of stress σ_{22} through thickness at the center with combined load. 66

4.30 Distribution of strain Γ_{33} through thickness at the center with combined load. 66

4.31 Distribution of electric potential ϕ through thickness at the center with combined load. 67

4.32 Layup of the three-layered plate. 68

4.33 Deflection u_3 of the plate along $x_2 = 0.07$ m with electric load. 70

Figure Page

4.34 Distribution of strain Γ_{11} through thickness at the center with electric load. 70

4.35 Distribution of stress σ_{11} through thickness at the center with electric load. 71

4.36 Distribution of strain Γ_{22} through thickness at the center with electric load. 71

4.37 Distribution of stress σ_{22} through thickness at the center with electric load. 72

4.38 Distribution of strain Γ_{33} through thickness at the center with electric load. 72

4.39 Distribution of strain Γ_{13} through thickness at $x_1 = 0.035$ m, $x_2 = 0.07$ m with electric load. 73

4.40 Distribution of stress σ_{13} through thickness at $x_1 = 0.035$ m, $x_2 = 0.07$ m with electric load. 73

4.41 Distribution of strain Γ_{23} through thickness at $x_1 = 0.07$ m, $x_2 = 0.105$ m with electric load. 74

4.42 Distribution of stress σ_{23} through thickness at $x_1 = 0.07$ m, $x_2 = 0.105$ m with electric load. 74

4.43 Distribution of electric potential ϕ through thickness at the center with electric load. 75

4.44 Deflection u_3 of the plate along $x_2 = 0.07$ m with combined load. . . . 76

4.45 Distribution of strain Γ_{11} through thickness at the center with combined load. 76

4.46 Distribution of stress σ_{11} through thickness at the center with combined load. 77

4.47 Distribution of strain Γ_{22} through thickness at the center with combined load. 77

4.48 Distribution of stress σ_{22} through thickness at the center with combined load. 78

4.49 Distribution of strain Γ_{33} through thickness at the center with combined load. 78

4.50 Distribution of strain Γ_{13} through thickness at $x_1 = 0.035$ m, $x_2 = 0.07$ m with combined load. 79

Figure Page

4.51 Distribution of stress σ_{13} through thickness at $x_1 = 0.035$ m, $x_2 = 0.07$ m with combined load. 79

4.52 Distribution of strain Γ_{23} through thickness at $x_1 = 0.07$ m, $x_2 = 0.105$ m with combined load. 80

4.53 Distribution of stress σ_{23} through thickness at $x_1 = 0.07$ m, $x_2 = 0.105$ m with combined load. 80

4.54 Distribution of electric potential ϕ through thickness at the center with combined load. 81

4.55 Boundary condition implementation of the fixed plate. 82

4.56 Deflection u_3 of the fixed plate along $x_2 = 0.07$ m. 83

4.57 Distribution of strain Γ_{11} through thickness at the center. 83

4.58 Distribution of stress σ_{11} through thickness at the center. 84

4.59 Distribution of strain Γ_{22} through thickness at the center. 84

4.60 Distribution of stress σ_{22} through thickness at the center. 85

4.61 Distribution of strain Γ_{33} through thickness at the center. 85

4.62 Distribution of strain Γ_{13} through thickness at $x_1 = 0.035$ m, $x_2 = 0.07$ m. 86

4.63 Distribution of stress σ_{13} through thickness at $x_1 = 0.035$ m, $x_2 = 0.07$ m. 86

4.64 Distribution of strain Γ_{23} through thickness at $x_1 = 0.07$ m, $x_2 = 0.105$ m. 87

4.65 Distribution of stress σ_{23} through thickness at $x_1 = 0.07$ m, $x_2 = 0.105$ m. 87

4.66 Distribution of electric potential ϕ through thickness at the center. . . 88

ABSTRACT

Long, Yufei MSAA, Purdue University, May 2015. Asymptotic Modelling of a Thermopiezoelastic Anisotropic Smart Plate. Major Professor: Wenbin Yu.

Motivated by the requirement of modelling for space flexible reflectors as well as other applications of plate structures in engineering, a general anisotropic laminated thin plate model and a monoclinic Reissner-Mindlin plate model with thermal deformation, two-way coupled piezoelectric effect and pyroelectric effect is constructed using the variational asymptotic method, without any ad hoc assumptions. Total potential energy contains strain energy, electric potential energy and energy caused by temperature change. Three-dimensional strain field is built based on the concept of warping function and decomposition of the rotation tensor. The feature of small thickness and large in-plane dimension of plate structure helped to asymptotically simplify the three-dimensional analysis to a two-dimensional analysis on the reference surface and a one-dimensional analysis through the thickness.

For the zeroth-order approximation, the asymptotically correct expression of energy is derived into the form of energetic equation in classical laminated plate theory, which will be enough to predict the behavior of plate structures as thin as a space flexible reflector. A through-the-thickness strain field can be expressed in terms of material constants and two-dimensional membrane and bending strains, while the transverse normal and shear stresses are not predictable yet. In the first-order approximation, the warping functions are further disturbed into a high order and an asymptotically correct energy expression with derivatives of the two-dimensional strains is acquired. For the convenience of practical use, the expression is transformed into a Reissner-Mindlin form with optimization implemented to minimize the error. Transverse stresses and strains are recovered using the in-plane strain variables.

Several numerical examples of different laminations and shapes are studied with the help of analytical solutions or shell elements in finite element codes. The constitutive relation is validated by the excellent agreement between the results from three-dimensional finite element analyses and the presented model for both thin plates using zeroth-order approximation and thick plates using first-order approximation.

1. Introduction

1.1 Motivation

1.1.1 Piezoelectric Plate Structures

Plate structures are those structures with two of their dimensions much greater than the other one and are flat in the two large dimension directions when unstressed. Plate structures are commonly used in aerospace, mechanical, civil and other engineering. Typical applications include floors and ceilings in civil engineering, doors, machine housings, chassises and bodies of cars and trains et al. In aerospace engineering, wing skins, solar boards and plane reflectors can be considered as plate structures.

Fundamentally speaking, plate structures can be modelled using three-dimensional (3D) theory that solves fifteen unknowns in terms of three coordinates using totally fifteen equations: three kinematic equations defining strains in terms of displacements, six kinetic equations describing equilibrium in the structure, and six energetic equations relating stresses and strains. Taking the advantage of small thickness of a plate structure, simplification is implemented to replace the 3D unknowns with two-dimensional (2D) unknowns. Even though the total number of equations and unknowns may remain unchanged or even becomes more, analysis cost can be greatly decreased due to the reduction of dimension. In order to reduce the number of dimensions, an analysis through the thickness is required to construct a constitutive relation which is not a function of the thickness coordinate, making the multi-layered plate as a homogeneous one. By this process of homogenization, stresses and strains can be expressed as force resultants and generalized 2D strains. Along with modified kinematics and kinetics, a plate structure can be solved using a 2D theory in terms of in-plane coordinates.

When a plate structure is laminated with smart materials such as piezoelectric or magnetostrictive materials, it can be called as a smart plate. In a smart plate, smart materials are utilized as sensors and actuators to achieve active shape and vibration control ([1], [2]and [3]). Piezoelectric plates are the most widely used smart plates. A piezoelectric smart plate will generate strain or stress under electric field, and will generate electric field in the piezoelectric material if stressed. This behavior leads to a coupling between electric energy and mechanical energy, making the modelling more difficult than conventional plates. Besides, most piezoelectric materials also have pyroelectricity, which generates electric charges when the material is heated. This effect couples the electric energy with thermal energy. Since thermal stress and strain affect the performance of laminates significantly, it is valuable to take pyroelectric effect and thermal deformation into consideration when modelling multi-layered smart plates, especially for those in space application.

1.1.2 Flexible Space Reflector

Based on the requirement of higher resolution and larger field of view in space-to-space and space-to-earth observation, large scale space reflectors are studied by researchers. A research shows that deployed on the medium earth orbit (MEO) at the altitude of 5000 km, a reflector with its diameter of 30 m can provide the same resolution of 10 cm as today's reflector deployed on the low earth orbit, while it can provide a view to almost achieve global monitoring [4]. However, reflectors at this size are too large and heavy to be sent by current launch vehicles if using traditional rigid structures. Consequently, the idea of flexible reflector is put forward to achieve low-cost, low-weight and foldability.

Flexible reflectors feature high flexibility and extremely small thickness. These help to reduce the weight and size as a launch payload while they also induce the disadvantage of being vulnerable to external disturbance and hard to maintain the shape accuracy. Early experiments on flexible reflectors concentrated on inflatable

structures [5], which can use air pressure to maintain the shape, while the shape accuracy is still limited and they are not applicable to all kinds of geometry such as a plane reflector. As a result, the concept of active control becomes attractive as it can achieve in-orbit, real-time shape adjustment with the help of actuators bonded on the reflector.

One practical way to realize active control is to laminate piezoelectric material such as polyvinylidene fluoride (PVDF) on the reflector to make it a multi-layered smart plate. Charged by DC voltage, piezoelectric actuators can generate a strain and consequently provide a in-plane bending moment to change the shape of the reflector. Common implementation includes unimorph and bimorph as shown in Figure 1.1. Bimorph makes the reflector easier to model since it is close to be symmetric through the thickness while it would lead the manufacturing to be complicated as opposite voltages need to be applied on the surface of the two piezoelectric layers.

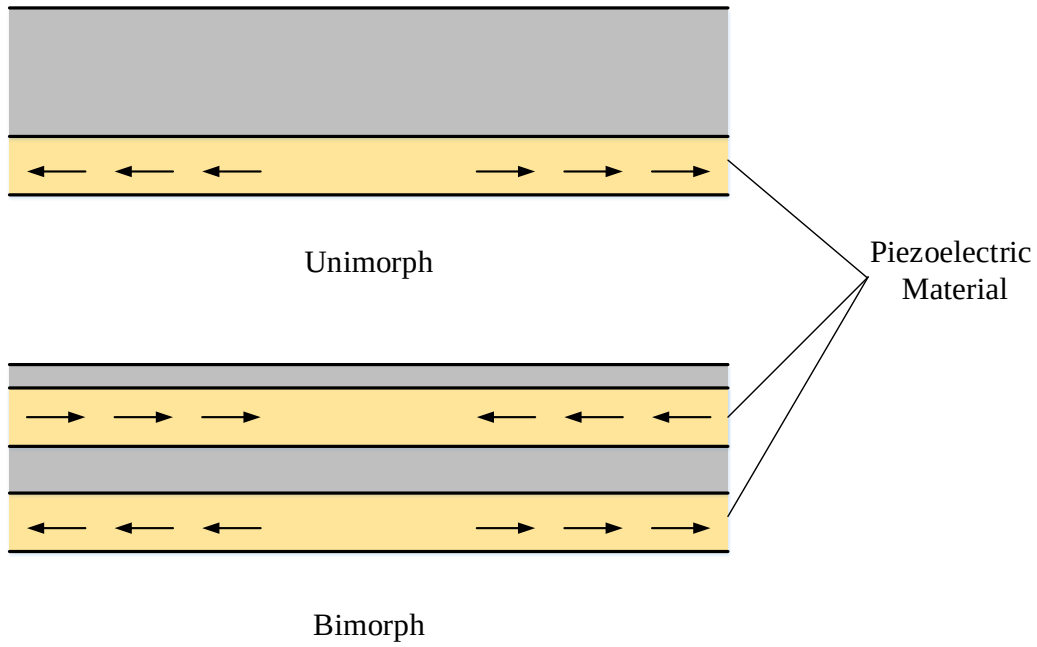

Figure 1.1. Piezoelectric actuator implementation.

Even though lots of research have achieved high shape control accuracy in both static and dynamic cases and verified the feasibility of active control ([6], [7], [8], [9] and [10]), they are still mainly based on 3D finite element analysis (FEA) and experiments. Mathematical modelling in current research usually neglects the anisotropic nature of piezoelectric materials and simplifies the reflector to be an isotropic plate. Piezoelectric to thermal analogy used in finite element analyses creates inability to induce both piezoelectric and thermal effects, which should not be neglected in space applications, especially when piezoelectric effect is considered to be two-way coupling and thermal effect to be one-way. Besides, the cost of 3D FEA makes it impossible to provide a real-time control algorithm in orbit deployment. A high-fidelity model containing the coupling of piezoelectric effect and thermal effect are required to help further improve the performance of flexible space reflectors.

1.2 Previous Works

1.2.1 Piezoelectric Plate Modelling

Modelling for piezoelectric plates has long been an interesting topic among engineers. The piezoelectric effect was first demonstrated by Pierre and Jacques Curie brothers in 1880 and the converse effect was mathematically deduced a year later by Gabriel Lippmann. Modelling for plate structures bonded with piezoelectric materials is more and more popular in recent years because of their control capability as mentioned in the previous section. Although many efforts are made to get exact 3D solutions for piezoelectric plates, they are still only available to limited cases ([11], [12], [13] and [14]). As a result, modelling is still highly relying on plate theories. However, most of the existing works are based on ad hoc assumptions on stresses and displacements for simplification, making stresses and strains in the structure unnecessarily restricted before any analyses are proceeded. Based on the limitation of transverse shear strains, these models can be classified as Kirchhoff-Love (classical) plate model, Reissner-Mindlin (refined) plate model, et al.

For thin plates, classical plate model can be applied to neglect transverse shear deformation. Ricketts [15] built a model for a piezoelectric isotropic plate in which the deformation of the plate is calculated in advance based on classical plate theory, without considering piezoelectricity. Then electric charge and stresses are calculated based on deflection. Results show that dynamic performance is limited to low frequency. Lee [16] developed an isotropic laminated plate model based on Kirchhoff-Love assumptions. Modelling is separated when piezoelectric materials are used as sensors or actuators, though reciprocal relationship is provided. Wang et al. [17] studied vibration of a piezoelectric circular plate using the Kirchhoff-Love plate model. Orthotropic properties of piezoelectric material is considered and electric and mechanical fields are fully coupled to ensure the satisfaction of Maxwell equation. The results prove a quadratic distributed electric potential along the radial direction, rather than a uniform distribution as assumed previously. Beginning from 3D formulations of a piezoelectric plate, Figueiredo and Leal [18] used asymptotic analysis to get a 2D piezoelectric model. By applying a hypothesis of zero elastic constants in thickness direction, the model converges to the Kirchhoff-Love theory when the thickness goes to zero. When plates get thicker, transverse shear strains are no longer negligible, and refined models such as the Reissner-Mindlin model and higher order shear deformation models are needed. Chandrashekhara and Agarwal [2] modified Lee's [16] formulation to a Reissner-Mindlin model and used it for vibration control of a plate with discretely distributed sensors and actuators. Huang and Wu [19] constructed a model for multi-layered laminates with both composites and piezoelectric materials. Displacements are expressed the same way as the Mindlin theory and electric potential are expanded to quadratic through the thickness. Modifications on shear correction factor and shape functions are adopted to improve accuracy. Qu [20] derived finite element formulations for composite laminated plates with coupled direct and converse piezoelectric effects. A degree of freedom (DOF) reduction process is implemented to eliminate unnecessary piezoelectric related DOFs at the part without piezoelectric sensors or actuators. By this way the computation is accelerated. Luo and Tong [1]

presented a finite element analysis for plate twisting and bending shape control using adhesively bonded orthotropic piezoelectric actuators. Pai et al. [21] proposed a refined geometrically nonlinear model for composite plates with piezoelectric sensors and actuators, but the piezoelectricity and mechanical forces are not coupled. This model has good flexibility since nonlinearity, shear deformation and anisotropic are all included. Mitchell and Reddy [22] derived a composite laminated piezoelectric plate model including the energy from electrostatic charge, using a third-order shear deformation theory [23]. Besides the classical model, results are also compared with third-order shear deformation theory without considering electrostatic charge, and shows that electrostatic charge becomes important when the ratio of thickness of piezoelectric layer to the total thickness is large. Kapuria and Achary [24] used a modified zigzag theory along with von Karman geometric nonlinearity to analyze the buckling of piezoelectric plates. Comparison of results from this work and the exact solution [25] proves its improvement to third-order theory on buckling loads and modal distribution prediction.

Many researchers also concern the effect of temperature load on piezoelectric plates. Since most piezoelectric materials also present pyroelectric effect, thermal expansion would not be the only effect to be considered when temperature changes [26]. Tauchert [27] proposed an analysis on thermal deformation of a piezoelectric laminated plate based on Kirchhoff assumptions. Heat conduction is considered while temperature is one-way coupled with electric load. Neither direct piezoelectric effect nor electrostatic charge is concerned in the work. Tzou and Ye [28] developed a solid finite element that can be used for analyzing piezothermoelastic laminated structures. Both direct and converse piezoelectric effects are considered while the temperature field is in steady state. Efficiency of the element is validated by static and dynamic control simulation. Krommer and Irschik [29] derived a Reissner-Mindlin type piezoelectric plate under thermal load. Concentration is put on the influence of direct piezoelectric and pyroelectric effect on plate stiffness. Cho and Oh [30] constructed a fully coupled thermopiezoelastic composite plate model, in which temperature and

electric field are treated as variables, using a higher order zigzag theory. Results from coupled and uncoupled thermal loads are compared and have found that uncoupled case would have overestimation. Kapuria and Achary [31] introduced another zigzag theory in third-order that can achieve the consistency of no shear traction on the top and bottom surfaces. Results are compared with conventional third-order theory under electric potential, mechanical and thermal loads. Oh et al. [32] developed a lower-order shear deformation theory averaged from higher-order zigzag theory and applied it on modelling fully coupled electro-thermo-mechanical laminated plates. Results are compared with the higher-order theory in [30] and show good agreement while lower-order theory has the advantage of being able to directly implement in commercial finite element codes. In addition to deformation and dynamics studies, a thermal fracture analysis of piezoelectric laminated plate is presented by Ueda [33].

1.2.2 Plate Modelling Based on Variational-Asymptotic Method

Even though many results from plate models with ad hoc assumptions can provide acceptable accuracy, those assumptions are mostly unnecessary and can make the models contradicting against themselves. For example, in Kirchhoff-Love plate model, 3D model is reduced to 2D by applying plane stress assumption, which means no transverse shear and normal stresses, but the Kirchhoff-Love assumption of rigid transverse normal enforces transverse shear and normal strains also to be zero. This can be true only when the Poisson's ratio is zero. Ad hoc assumptions are indeed helpful in understanding and simplifying the modelling procedure, but hard-to-predict accuracy loss caused by the incorrectness of the assumptions can largely restrict the potential of corresponding theories.

In contrast, the variational-asymptotic method (VAM), developed by Berdichevsky [34] in 1979, is a mathematical approach capable for analyzing functionals with relatively small parameters. By using VAM, no prior assumption is required for modelling plate structures. For structure modelling, VAM directly works on energy functional

instead of differential equations, allowing the derivation in a more systematic way. By taking the advantage of small parameter of h/l in plate structures, where h is the thickness and l indicates the characteristic in-plane dimension, a model with desired accuracy can be acquired.

Early application of VAM on composite plate modelling includes the work by Atilgan and Hodges [35]. Their work is extended by Sutyrin and Hodges in [36] and [37] to make the model practical for multi-layered composite plates by transforming the formula to a Reissner-Mindlin-like model by minimizing an interaction term. Yu et al. [38, 39] developed a general composite laminated plate model based on the geometrically nonlinear theory in [40]. The model is expressed in Reissner-like form by an optimization and recovery relations allow it to accurately predict the stress field including transverse normal stress. Later, Yu et al. [41] derived the same asymptotic model in a finite element based approach, making the theory available in finite element analyses. Using the same finite element approach, Yu and Hodges extended their previous work for applying on a thermopiezoelastic composite plate [42]. But electric field and temperature field are only one way coupled with mechanical field. Liao and Yu developed the model to accommodate a fully coupled piezoelectric composite plate. The zeroth-order approximation is completed analytically and the first-order approximation is in finite element approach. Both the case of surface and interface coated electrodes [43] and lateral boundary coated electrodes [44] are derived. Recently, Chen and Yu [45] further induced magnetic field in the composite laminate model. Piezoelectric effect, piezomagnetic effect and magnetoelectric effect are fully coupled. The derivation is completed in an analytical approach.

1.3 Present Work and Outline

The purpose of this thesis is to derive a model for multi-layered surfaces and interfaces electroded piezoelectric plates under thermal loads, which can help to analyze the deformation of flexible space reflector as well as other composite laminated plates.

As described in the above section, most existing thermopiezoelastic plate models are based on ad hoc assumptions that can create loss of accuracy while VAM can effectively avoid this problem. Consequently a precise thermopiezoelastic laminated plate model that can provide constitutive relations for efficient plate solving is required for future applications.

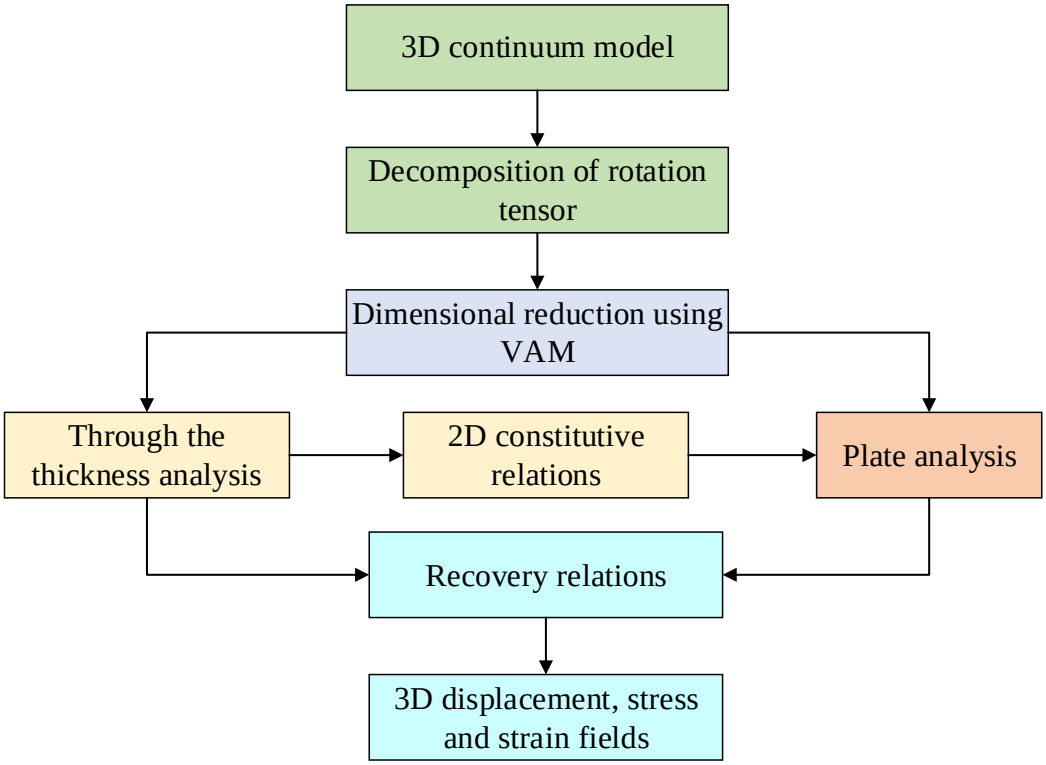

Figure 1.2. Procedure of plate analysis using VAM.

The methodology of this thesis is illustrated in figure 1.2. Firstly 3D continuum formulation of the plate is presented. With the help of the concept of decomposition of the rotation tensor [46] and 3D warping functions, 3D strains can be expressed in terms of 2D generalized strains. Then energy expression of the plate is given out in terms of potential energy, which contains elasticity, piezoelectricity, dielectricity,

pyroelectricity and thermal expansion, kinetic energy and virtual work from external loads. Since the main purpose is to study the deformation of plates, converse effect of pyroelectricity is not included to avoid heat conduction problem. 3D model is then reduced to a 2D formulation by applying the VAM. The reduced 2D plate model can be solved in the same way as classical or first-order shear deformation theory. 3D displacement, stress and strain fields can be recovered using warping functions derived from energy expression. Outline of the present work is followed.

- Chapter 2 provides the theoretical prerequisites of variatioanl-asymptotic plate analysis, including the 3D formulae, energy expressions and a brief demonstration of the VAM.
- Chapter 3 is the derivation from 3D plate model to a 2D model, also called dimensional reduction. The process is in two parts: zeroth-order reduction, which coincide the classical plate model, and first-order reduction, which can be transformed into a Reissner-Mindlin model.
- Chapter 4 presents several numerical examples validating both the zeroth-order model and the first-order model.
- Chapter 5 concludes the work done for this thesis.
- Chapter 6 suggests possible future developments of the present work.

2. Fundamental Theories

In this chapter, several fundamental theories required to complete later work, including 3D modelling of the undeformed and deformed plate, formulation of the 3D strain field and generalized 2D strains, energy expressions and the VAM, are introduced. Note that these may not be original work of the thesis author while it would be necessary to show the author's understanding of these indispensable foundations.

Notation conventions that are used in this and following chapters are explained here. In subscripts, a comma implies partial derivative, and Greek letters refer to 1 and 2 while Latin letters refers to 1, 2 and 3. Summation convention is applied unless specified. The operator $(\,)'$ implies partial derivative with respect to x_3 coordinate. The operator $\dot{(\,)}$ implies partial derivative with respect to time. The subscript $(\,)_{\|}$ indicates a column matrix with two in-plane components, so that $(\,)_{\|} = [(\,)_1 \quad (\,)_2]^{\mathrm{T}}$. The notation $\tilde{(\,)}$ refers to a antisymmetric matrix with its entries satisfying the equation $\tilde{(\,)} = -e_{ijk}(\,)_k$, where e_{ijk} is the permutation symbol. Angle brackets indicate definite integral on x_3 direction from the bottom to the top of the plate.

2.1 Plate Kinematics

2.1.1 Deformation Configurations

Position of a point in a plate can be determined by its Cartesian coordinates x_i, as shown in Figure 2.1, where x_α are two orthogonal coordinates in the reference surface and x_3 is the normal coordinate with the origin locating at the middle of the thickness. Orthogonal triad $\mathbf{b}_i$ denote the unit vectors in x_i directions of the

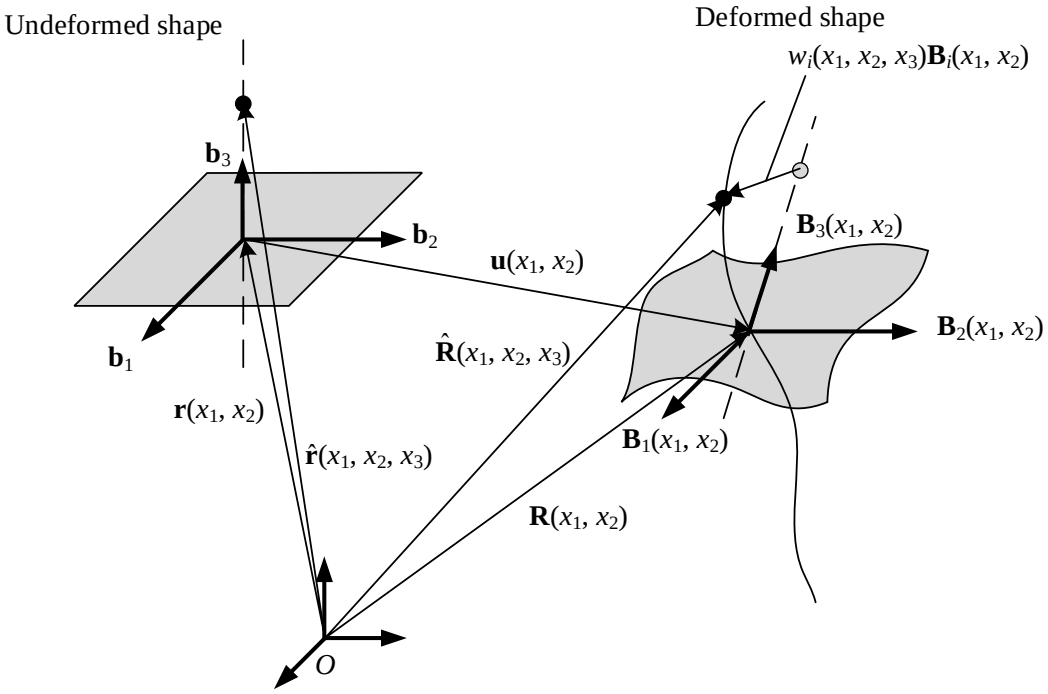

Figure 2.1. Schematic of plate deformation.

undeformed plate, so any material point in the undeformed plate can have a position vector $\hat{\mathbf{r}}$ from a fixed point O so that

$$\hat{\mathbf{r}}\left(x_1, x_2, x_3\right) = \mathbf{r}\left(x_1, x_2\right) + x_3\mathbf{b}_3 \tag{2.1}$$

where $\mathbf{r}$ denotes the position vector, from point O, of intersection point between the reference surface and the normal line on which the described point is located. Integrating both sides of equation (2.1), we have

$$\langle\hat{\mathbf{r}}\left(x_1, x_2, x_3\right)\rangle = h\mathbf{r}\left(x_1, x_2\right) \tag{2.2}$$

where h is the thickness of the plate.

When deformation happens, the material point described by vector $\hat{\mathbf{r}}$ in the undeformed state will have the position vector $\hat{\mathbf{R}}$ in the deformed state. Every material

point in the undeformed state will uniquely have a deformation determined position vector in the deformed shape. For expression, orthogonal unit vector triad for the deformed plate $\mathbf{B}_i$ is introduced. Relation between $\mathbf{b}_i$ and $\mathbf{B}_i$ is indicated in a similar way as coordinate transformation using direction cosine matrix $\mathcal{C}(x_1, x_2)$

$$\begin{aligned} \mathbf{B}_i &= \mathcal{C}_{ij}\mathbf{b}_j \\ \mathcal{C}_{ij} &= \mathbf{B}_i \cdot \mathbf{b}_j \end{aligned} \tag{2.3}$$

so that $\mathbf{B}_i$ and $\mathbf{b}_i$ are identical when the plate is undeformed. Then a rotation tensor can be defined as

$$\mathbf{C}^{Bb} = \mathcal{C}_{ij}\mathbf{b}_j\mathbf{b}_i = \mathbf{B}_i\mathbf{b}_i \tag{2.4}$$

Now $\hat{\mathbf{R}}$ can be expanded to the following form for any definition of $\mathbf{B}_i$

$$\hat{\mathbf{R}}(x_1, x_2, x_3) = \mathbf{R}(x_1, x_2) + x_3\mathbf{B}_3(x_1, x_2) + w_i(x_1, x_2, x_3)\,\mathbf{B}_i(x_1, x_2) \tag{2.5}$$

where w_i are warping functions to ensure equation (2.5) to be able to describe all possible deformation. No assumption is made on the shape of warping functions and their exact expression will be solved in the next chapter. Unlike $\mathbf{b}_i$, which is clearly defined, $\mathbf{B}_i$ is not necessarily tangent to the coordinates in the deformed plate, so equation (2.5) is not unique for every point unless six more constraints are introduced to fix $\mathbf{B}_i$. For the first three constraints, it would be convenient to set $\mathbf{R}$ to be the average through the thickness, while an optimization problem to be occurred in the next chapter makes it more reasonable to set the constraint in the way of

$$\begin{aligned} \langle w_{\|}(x_1, x_2, x_3)\rangle &= c_{\|} \\ \langle w_3(x_1, x_2, x_3)\rangle &= 0 \end{aligned} \tag{2.6}$$

where $c_{\|}$ is a free variable independent of x_3, so that

$$\left\langle \hat{\mathbf{R}} \right\rangle = h\mathbf{R} + \begin{Bmatrix} c_{\|} \\ 0 \end{Bmatrix} \tag{2.7}$$

Two more constraints can be specified by setting $\mathbf{B}_3$ normal to the reference surface of the deformed plate. Although the unit vector is fixed to be normal, transverse

shear and thickness change are still allowed because of the warping functions, which dissociate the present work from any hypotheses. It is still possible for $\mathbf{B}_\alpha$ to rotate around $\mathbf{B}_3$, so introducing

$$\mathbf{B}_1 \cdot \mathbf{R}_{,2} = \mathbf{B}_2 \cdot \mathbf{R}_{,1} \tag{2.8}$$

to be the last constraint. Note that all variables in the deformed state can be function of time t, but it is not explicitly shown for simplifying notation.

2.1.2 3D Strain Field

In a Cartesian coordinate, the covariant base vectors in the undeformed state $\mathbf{g}_i$ are defined as

$$\mathbf{g}_i\left(x_1, x_2, x_3\right) = \frac{\partial \hat{\mathbf{r}}}{\partial x_i} \tag{2.9}$$

then the contravariant base vectors $\mathbf{g}^i$ of the undeformed plate can be express in the definition

$$\mathbf{g}^i\left(x_1, x_2, x_3\right) = \frac{1}{2\sqrt{\mathrm{g}}} e_{ijk} \mathbf{g}_j \times \mathbf{g}_k \tag{2.10}$$

where

$$\mathrm{g} = \det\left(\mathbf{g}_i \cdot \mathbf{g}_j\right) \tag{2.11}$$

For plate structures, it is apparent that $\mathbf{g}_i = \mathbf{b}_i$, so

$$\sqrt{\mathrm{g}} = \mathbf{g}_1 \cdot \left(\mathbf{g}_2 \times \mathbf{g}_3\right) = 1 \tag{2.12}$$

$$\mathbf{g}^i = \mathbf{g}_i = \mathbf{b}_i \tag{2.13}$$

Similarly, when the plate is deformed, the covariant base vectors in the deformed state $\mathbf{G}_i$ are

$$\mathbf{G}_i\left(x_1, x_2, x_3\right) = \frac{\partial \hat{\mathbf{R}}}{\partial x_i} \tag{2.14}$$

Based on the base vectors of $\mathbf{g}_i$, $\mathbf{g}^i$ and $\mathbf{G}_i$, the nabla operator can be defined as

$$\nabla = \frac{\partial}{\partial x_i} \mathbf{g}^i \tag{2.15}$$

So the deformation gradient tensor $\mathbf{F}$ is defined as

$$\mathbf{F} = \hat{\mathbf{R}}\nabla = \frac{\partial \hat{\mathbf{R}}}{\partial x_i}\mathbf{g}^i = \mathbf{G}_i\mathbf{g}^i \tag{2.16}$$

Since the deformation gradient tensor is resolved along the mixed bases [47], that is

$$\mathbf{F} = F_{ij}\mathbf{B}_i\mathbf{b}_j \tag{2.17}$$

then

$$F_{ij} = \mathbf{B}_i \cdot \mathbf{G}_k\mathbf{g}^k \cdot \mathbf{b}_j \tag{2.18}$$

To obtain the 3D strain field, Jauman-Biot-Cauchy strain can be adopted in the form derived from decomposition of the rotation tensor [47]

$$\Gamma_{ij} = \frac{1}{2}(F_{ij} + F_{ji}) - \delta_{ij} \tag{2.19}$$

where δ_{ij} is the Kronecker symbol.

For expressing 3D strain field in terms of 2D strains, one can define 2D generalized strains in the same way as [40]

$$\mathbf{R}_{,\alpha} = \mathbf{B}_\alpha + \varepsilon_{\alpha\beta}\mathbf{B}_\beta \tag{2.20}$$

$$\mathbf{B}_{i,\alpha} = (-K_{\alpha\beta}\mathbf{B}_\beta \times \mathbf{B}_3 + K_{\alpha 3}\mathbf{B}_3) \times \mathbf{B}_i \tag{2.21}$$

where $\varepsilon_{\alpha\beta}$ and $K_{\alpha\beta}$ are 2D generalized membrane strains and curvatures. Recall equation (2.5) and (2.13), equation (2.18) can be written in the form of

$$F_{ij} = \mathbf{B}_i \cdot \frac{\partial \hat{\mathbf{R}}}{\partial x_j} = \mathbf{B}_i \cdot \mathbf{R}_{,j} + \mathbf{B}_i \cdot (x_3\mathbf{B}_3)_{,j} + \mathbf{B}_i \cdot w_{k,j}\mathbf{B}_k + \mathbf{B}_i \cdot w_k\mathbf{B}_{k,j} \tag{2.22}$$

Strains are assumed to be small compared to unity and warping functions are of the similar magnitude of strain when only geometric nonlinearity can be considered. So the last term of equation (2.22) can be neglect since it is of high order. Now one can derive the 3D strain field expression to be

$$\begin{aligned} \Gamma_e &= \epsilon + x_3\kappa + I_\alpha w_{\|,\alpha} \\ 2\Gamma_s &= w_\|{}' + e_\alpha w_{3,\alpha} \\ \Gamma_t &= w_3{}' \end{aligned} \tag{2.23}$$

where

$$\begin{gathered}\Gamma_e = [\ \Gamma_{11} \quad 2\Gamma_{12} \quad \Gamma_{22}\ ]^{\mathrm{T}} \\ 2\Gamma_s = [\ 2\Gamma_{13} \quad 2\Gamma_{23}\ ]^{\mathrm{T}} \\ \Gamma_t = \Gamma_{33}\end{gathered} \tag{2.24}$$

and

$$\begin{gathered}\epsilon = [\ \varepsilon_{11} \quad 2\varepsilon_{12} \quad \varepsilon_{22}\ ]^{\mathrm{T}} \\ \kappa = [\ K_{11} \quad K_{12} + K_{21} \quad K_{22}\ ]^{\mathrm{T}}\end{gathered} \tag{2.25}$$

and

$$\begin{gathered}I_1 = \begin{bmatrix} 1 & 0 \\ 0 & 1 \\ 0 & 0 \end{bmatrix} \qquad I_2 = \begin{bmatrix} 0 & 0 \\ 1 & 0 \\ 0 & 1 \end{bmatrix} \\ e_1 = \begin{Bmatrix} 1 \\ 0 \end{Bmatrix} \qquad e_2 = \begin{Bmatrix} 0 \\ 1 \end{Bmatrix}\end{gathered} \tag{2.26}$$

So far kinematics of a plate is formulated. However, for a coupled piezoelectric laminated plates, electric field should also be in concern along with the mechanical field. Electric field can be defined using electric potential $\phi(x_1, x_2, x_3)$

$$\begin{gathered}E_s = [\ E_1 \quad E_2\ ]^{\mathrm{T}} = -[\ \phi_{,1} \quad \phi_{,2}\ ]^{\mathrm{T}} \\ E_t = E_3 = -\phi'\end{gathered} \tag{2.27}$$

In this study electrodes of the piezoelectric plate are coated on the top and bottom surfaces or interfaces between layers. Electrodes are assumed to be of negligible thickness and have no influence on mechanical properties of the plate. Then electric potential can be specified at $x_3 = h_i$, where h_i refers to the position of surface or interface and here i indicates the numbering of layers varying from 1 to $k+1$ and k is the total number of layers, in which sense h_1 refers to the bottom surface and h_{k+1} to the top surface. Although temperature load is considered in the work, it is only one-way coupling so temperature change $T(x_1, x_2, x_3)$ is treated as a known function.

2.2 Energy Formulation

The elastodynamic behavior of a piezoelectric laminated plate is governed by the extended Hamiltion's principle [48]

$$\int_{t_1}^{t_2} \left[\delta(\mathcal{K}-\mathcal{U}) + \overline{\delta\mathcal{W}}\right] \mathrm{d}t = 0 \tag{2.28}$$

where t_1 and t_2 are arbitrary fixed time; $\mathcal{K}$ is the kinetic energy; $\mathcal{U}$ is the internal potential energy related to strain, electric field and temperature; $\overline{\delta\mathcal{W}}$ is the virtual work of external loads. The overline indicates that the virtual work is not necessarily the variation of a functional. For dimensional reduction purpose, three energy quantities, $\mathcal{K}$, $\mathcal{U}$ and $\overline{\delta\mathcal{W}}$, need to be expressed in terms of 2D plate variables.

2.2.1 Internal Potential Energy

For piezoelectric structures with thermal loads, the internal potential energy $\mathcal{U}$ turns out to be the electric enthalpy containing mechanical, electric and thermal fields

$$\begin{aligned}\mathcal{U} = \frac{1}{2}\int_{\mathcal{V}} (&\boldsymbol{\Gamma} : \boldsymbol{C}^{\boldsymbol{E}} : \boldsymbol{\Gamma} - 2\boldsymbol{E}\cdot\boldsymbol{e} : \boldsymbol{\Gamma} \\ &- 2\boldsymbol{\Gamma} : \boldsymbol{C}^{\boldsymbol{E}} : \boldsymbol{\alpha}T - \boldsymbol{E}\cdot\boldsymbol{\varepsilon}^{\boldsymbol{\Gamma}}\cdot\boldsymbol{E} - 2\boldsymbol{E}\cdot\boldsymbol{p}T)\mathrm{d}\mathcal{V}\end{aligned} \tag{2.29}$$

where $\boldsymbol{\Gamma}$ is the strain field tensor; $\boldsymbol{E}$ is the electric field vector; T is the temperature change; $\boldsymbol{C}^{\boldsymbol{E}}$ is the material's elastic constant tensor at a constant electric field; $\boldsymbol{e}$ is the piezoelectric stress coefficient tensor; $\boldsymbol{\alpha}$ is thermal expansion coefficient tensor; $\boldsymbol{\varepsilon}^{\boldsymbol{\Gamma}}$ is the dielectric constant tensor at a constant strain field; $\boldsymbol{p}$ is pyroelectric coefficient vector; $\mathcal{V}$ is the space domain of the 3D structure. For piezoelectric laminated plates, equation (2.29) can be expressed as the integral of area potential energy density

$$\mathcal{U} = \int_{\Omega} \mathcal{H}\mathrm{d}\Omega \tag{2.30}$$

where Ω is the area domain of the reference surface and

$$\begin{aligned}\mathcal{H} = \frac{1}{2}\Bigg\langle \begin{Bmatrix} \Gamma_e \\ 2\Gamma_s \\ \Gamma_t \end{Bmatrix}^{\mathrm{T}} \begin{bmatrix} C_e & C_{es} & C_{et} \\ C_{es}^{\mathrm{T}} & C_s & C_{st} \\ C_{et}^{\mathrm{T}} & C_{st}^{\mathrm{T}} & C_t \end{bmatrix} \begin{Bmatrix} \Gamma_e \\ 2\Gamma_s \\ \Gamma_t \end{Bmatrix} \Bigg\rangle \\ - \Bigg\langle \begin{Bmatrix} \Gamma_e \\ 2\Gamma_s \\ \Gamma_t \end{Bmatrix}^{\mathrm{T}} \begin{bmatrix} e_b & e_{et} \\ e_s & e_a \\ e_c & e_t \end{bmatrix} \begin{Bmatrix} E_s \\ E_t \end{Bmatrix} \Bigg\rangle \\ - \Bigg\langle \begin{Bmatrix} \Gamma_e \\ 2\Gamma_s \\ \Gamma_t \end{Bmatrix}^{\mathrm{T}} \begin{bmatrix} C_e & C_{es} & C_{et} \\ C_{es}^{\mathrm{T}} & C_s & C_{st} \\ C_{et}^{\mathrm{T}} & C_{st}^{\mathrm{T}} & C_t \end{bmatrix} \begin{Bmatrix} \alpha_e \\ \alpha_s \\ a_t \end{Bmatrix} T \Bigg\rangle \\ - \frac{1}{2}\Bigg\langle \begin{Bmatrix} E_s \\ E_t \end{Bmatrix}^{\mathrm{T}} \begin{bmatrix} d_s & d_{et} \\ d_{et}^{\mathrm{T}} & d_t \end{bmatrix} \begin{Bmatrix} E_s \\ E_t \end{Bmatrix} \Bigg\rangle \\ - \Bigg\langle \begin{Bmatrix} E_s \\ E_t \end{Bmatrix}^{\mathrm{T}} \begin{Bmatrix} p_s \\ p_t \end{Bmatrix} T \Bigg\rangle \end{aligned} \tag{2.31}$$

where C_e, C_{es}, C_{et}, C_s, C_{st} and C_t are the submatrices of the partitioned 6×6 material's elastic constant matrix at a constant electric field; e_b, e_{et}, e_s, e_a, e_c and e_t are the submatrices of the partitioned transpose of the 3×6 piezoelectric stress coefficient matrix; α_e, α_s and α_t are the submatrices of the partitioned 6×1 thermal expansion coefficient matrix; d_s, d_{et} and d_t are the submatrices of the partitioned 3×3 dielectric constant matrix at a constant strain field; p_s and p_t are the submatrices of the partitioned 3×1 pyroelectric coefficient matrix.

2.2.2 Kinetic Energy

For dynamic analysis, it is necessary to compute the kinetic energy. By taking the time derivative of equation (2.5), velocity of a material point in the 3D body can be expressed as

$$v = V + x_3\dot{\mathbf{B}}_3 + \dot{w}_i\mathbf{B}_i + w_i\dot{\mathbf{B}}_i \tag{2.32}$$

where v is the absolute velocity of the point in the 3D structure and V is the absolute velocity of the corresponding point in the reference surface. Angular velocity ω can be defined to express the time derivative of the $\mathbf{B}_i$ bases, so that

$$\begin{aligned}\dot{\mathbf{B}}_1 &= [\ 0 \quad \omega_3 \quad -\omega_2\ ]^{\mathrm{T}} \\ \dot{\mathbf{B}}_2 &= [\ -\omega_3 \quad 0 \quad \omega_1\ ]^{\mathrm{T}} \\ \dot{\mathbf{B}}_3 &= [\ \omega_2 \quad -\omega_1 \quad 0\ ]^{\mathrm{T}}\end{aligned} \tag{2.33}$$

then equation (2.32) can be rewritten as

$$v = V + \tilde{\omega}(\xi + w) + \dot{w} \tag{2.34}$$

where $\xi = [\ 0 \quad 0 \quad x_3\ ]^{\mathrm{T}}$ and v, V, ω, ξ and w are column matrices whose components are in $\mathbf{B}_i$ bases. Then total kinetic energy of the plate can be expressed as

$$\mathcal{K} = \frac{1}{2}\int_{\mathcal{V}} \rho v^{\mathrm{T}} v \mathrm{d}\mathcal{V} = \mathcal{K}_{2\mathrm{D}} + \mathcal{K}^* \tag{2.35}$$

where ρ is the volumetric mass density; $\mathcal{K}_{2\mathrm{D}}$ denotes the kinetic energy from reference surface and motion along the normal and $\mathcal{K}^*$ denotes the kinetic energy from warping and

$$\mathcal{K}_{2\mathrm{D}} = \frac{1}{2}\int_{\Omega} (\bar{\mu} V^{\mathrm{T}} V + 2\omega^{\mathrm{T}}\widetilde{\overline{\mu\xi}} V + \omega^{\mathrm{T}} \mathrm{j}\omega)\mathrm{d}\Omega \tag{2.36}$$

$$\mathcal{K}^* = \frac{1}{2}\int_{\mathcal{V}} \rho \left[(\tilde{\omega} w + \dot{w})^{\mathrm{T}}(\tilde{\omega} w + \dot{w}) + 2(V + \tilde{\omega}\xi)^{\mathrm{T}}(\tilde{\omega} w + \dot{w})\right] \mathrm{d}\mathcal{V} \tag{2.37}$$

where $\bar{\mu}$, $\overline{\mu\xi}$ and j are inertial constants which can be obtained by doing integrals through the thickness as

$$\begin{aligned}\bar{\mu} &= \langle \rho \rangle \\ \overline{\mu\xi} &= [\ 0 \quad 0 \quad \langle x_3 \rho \rangle\ ]^{\mathrm{T}} \\ \mathrm{j} &= \begin{bmatrix} \langle {x_3}^2 \rho \rangle & 0 & 0 \\ 0 & \langle {x_3}^2 \rho \rangle & 0 \\ 0 & 0 & 0 \end{bmatrix}\end{aligned} \tag{2.38}$$

2.2.3 Virtual Work

The virtual work in the plate due to the applied loads can be calculated as

$$\overline{\delta\mathcal{W}} = \int_\Omega \left(\left\langle \mathbf{P} \cdot \delta\hat{\mathbf{R}} \right\rangle + \boldsymbol{\tau} \cdot \delta\hat{\mathbf{R}}^+ + \boldsymbol{\beta} \cdot \delta\hat{\mathbf{R}}^- \right) \mathrm{d}\Omega + \int_s \left\langle \mathbf{Q} \cdot \delta\hat{\mathbf{R}} \right\rangle \mathrm{d}s \tag{2.39}$$

where s is the boundary of the reference surface; $\mathbf{P} = P_i\mathbf{B}_i$ is the applied body force; $\boldsymbol{\tau} = \tau_i\mathbf{B}_i$ is the applied traction on the top surface and $\boldsymbol{\beta} = \beta_i\mathbf{B}_i$ is the applied traction on the bottom surface; $\mathbf{Q} = Q_i\mathbf{B}_i$ is the applied tractions on the lateral boundary surfaces where s is located. The $+$ and $-$ signs in superscript denote the value at the top and bottom surface respectively. $\delta\hat{\mathbf{R}}$ can be derived by taking the variation of equation (2.5), such that

$$\delta\hat{\mathbf{R}} = \delta\mathbf{R} + x_3\delta\mathbf{B}_3 + \delta w_i\mathbf{B}_i + w_i\delta\mathbf{B}_i \tag{2.40}$$

The virtual displacement and rotation can be defined in a similar way as the definition of 2D general strains, so that

$$\delta\mathbf{R} = \overline{\delta q}_i\mathbf{B}_i \tag{2.41}$$

$$\delta\mathbf{B}_i = (-\overline{\delta\psi}_2\mathbf{B}_1 + \overline{\delta\psi}_1\mathbf{B}_2 + \overline{\delta\psi}_3\mathbf{B}_3) \times \mathbf{B}_i \tag{2.42}$$

where $\overline{\delta q}_i$ and $\overline{\delta\psi}_i$ are the virtual displacement and rotation components in the $\mathbf{B}$ bases respectively. Again, as in the definition of 3D strains, the last term of equation (2.40) can be dropped because the warping functions are small. Then, the virtual work done by applied loads can be obtained in two terms as

$$\overline{\delta\mathcal{W}} = \overline{\delta\mathcal{W}}_{\mathrm{2D}} + \overline{\delta\mathcal{W}}^* \tag{2.43}$$

where

$$\overline{\delta\mathcal{W}}_{\mathrm{2D}} = \int_\Omega \left(f_i\overline{\delta q}_i + m_\alpha\overline{\delta\psi}_\alpha \right) \mathrm{d}\Omega + \int_s \left(\langle Q_i \rangle\, \overline{\delta q}_i + \langle x_3 Q_\alpha \rangle\, \overline{\delta\psi}_\alpha \right) \mathrm{d}s \tag{2.44}$$

$$\overline{\delta\mathcal{W}}^* = \int_\Omega \left(\langle P_i\delta w_i \rangle + \tau_i\delta {w_i}^+ + \beta_i\delta {w_i}^- \right) \mathrm{d}\Omega + \int_s \langle Q_i\delta w_i \rangle \mathrm{d}s \tag{2.45}$$

in which f_i and m_α are generalized forces and moments defined as

$$\begin{aligned} f_i &= \langle P_i \rangle + \tau_i + \beta_i \\ m_\alpha &= \langle x_3 P_\alpha \rangle + \frac{h}{2}(\tau_\alpha - \beta_\alpha) \end{aligned} \tag{2.46}$$

In this study, the goal is to obtain a constitutive relation of the interior part of the plate, so for the Saint-Venant's Principle, edge effect can be safely neglected. Consequently, the second term in equation (2.45) is trivial and would not be considered in further derivation.

2.3 Variational-Asymptotic Method

The variational-asymptotic method (VAM) is a method that can deal with energy stationary value problems depending on small parameters such as the thickness of plates and shells. Its fundamental idea is solving the problem by neglecting terms asymptotically smaller than the designated order. Compared to formal asymptotic analyses which work on differential equations, the VAM directly works on functionals so it can be simpler as dropping one term in the variational statement is equivalent to dropping related terms in several differential equations simultaneously.

In order to proceed the VAM, it is important to know the way of recognizing the order of a function. Let there be continuous functions $f(x)$ and $g(x)$ defined on some domain and take the limits $x \to x_0$. Generally it will have three cases: $f(x) = O(g(x))$, $f(x) = o(g(x))$ and $f(x) \sim g(x)$, which means $f(x)$ is asymptotically bounded by or of the order of $g(x)$, $f(x)$ is asymptotically smaller than $g(x)$ and $f(x)$ is asymptotically equal to $g(x)$, respectively. Whether $f(x)$ is asymptotically smaller than $g(x)$ can be determined by calculating the expression

$$\lim_{x \to x_o} \frac{|f(x)|}{|g(x)|} \tag{2.47}$$

If this limit goes to zero, $f(x)$ can be determined to be asymptotically smaller and can be dropped in a functional if the order considered is up to the order of $g(x)$.

For example, when calculating the stationary point of a function using the VAM

$$f(u, \varepsilon) = u + u^2 + \varepsilon \sin u \tag{2.48}$$

where ε is a small parameter, ε can be set to zero to acquire the zeroth-order solution. By taking the derivative of $f(u, 0) = u + u^2$ and make it to be zero, it can be solved

easily that $u = -\frac{1}{2}$. Set $u = -\frac{1}{2} + u_1$ and substitute back into the original $f(u, \varepsilon)$. In order to compare the order with the sine function, a series expansion is required. Then,

$$\begin{aligned} f(-\frac{1}{2} + u_1, \varepsilon) = & \left(-\frac{1}{4} - \varepsilon \sin\frac{1}{2}\right) + u_1 \varepsilon \cos\frac{1}{2} \\ & + {u_1}^2 \left(1 + \frac{1}{2}\varepsilon \sin\frac{1}{2}\right) + O\big({u_1}^3\big) \end{aligned} \tag{2.49}$$

As u_1 is a perturbed term that is also small, it can be confirmed that ${u_1}^3 = o({u_1}^2)$ and ${u_1}^2\varepsilon = o({u_1}^2)$, so these asymptotically smaller terms can be dropped. Taking the derivative and setting to zero, it can be calculated that $u_1 = -\frac{1}{2}\varepsilon \cos\frac{1}{2}$ so the first-order approximate solution is $u = -\frac{1}{2} - \frac{1}{2}\varepsilon \cos\frac{1}{2}$. When $\varepsilon = 0.1$, the exact solution is -0.542813 and the approximate solution is -0.543879, with an error of 0.2 percent. This verifies that the VAM can provide an accurate approximation solution to the original problem. The same process can be repeated to get second or higher order solutions with further improved accuracy.

It is suitable to apply the VAM in analyzing structures with small parameters such as beams, plates and shells, the original statements of which may be too complicated to be solved directly. More detailed and systematic description of the VAM can be found in [49].

3. Dimensional Reduction

From the energy expression derived in last chapter, one can rewrite the Hamilton's Principle, equation (2.28), as

$$\int_{t_1}^{t_2} [\delta(\mathcal{K}_{2\mathrm{D}} + \mathcal{K}^* - \mathcal{U}) + \overline{\delta\mathcal{W}}_{2\mathrm{D}} + \overline{\delta\mathcal{W}}^*]\mathrm{d}t = 0 \tag{3.1}$$

It is expensive to solve this equation directly as this is a 3D problem. Implementation is required to simplify it to a 2D formula in terms of generalized strains and electric potential. Taking the feature of small h/l of plate structures, where h is the thickness and l indicates the characteristic in-plane dimension, this chapter reduced the 3D continuum model of the thermopiezoelastic plate to a 2D plate model by a through-the-thickness analysis using the VAM. Distinguished from formal methods that adopt unjustifiable hypotheses before analysis, process in the study involves no ad hoc assumption.

3.1 Order Assessment

Before implementing the VAM, it is necessary to recognize the order of terms in the expression and decide which terms can be considered to be small and dropped. Based on the definition of a plate structure, the ratio of thickness over the characteristic in-plane dimension of the reference surface is much smaller than one, that is, $h/l \ll 1$. As only geometric nonlinearity is considered and physical nonlinearity is beyond the topic of this thesis, both 3D and 2D strains are assumed to be small, that is, $\Gamma_{ij} \sim \varepsilon_{\alpha\beta} \sim \epsilon \ll 1$, so ϵ can represent the order of all strains. From the definition of 3D strain, equation (2.23), it can be found that the 2D curvature, κ, must satisfy the relation of $h\kappa \sim hK_{\alpha\beta} \sim \epsilon$.

As it is stated during the derivation of 3D strain, the order of warping functions are the same as the strains. However, from equation (2.5) and (2.23), the dimension

of warping function should be displacement, whose unit is meter in SI system, and the derivative of the warping function should have the same dimension as strain, so for a more precise declaration, the partial derivative of warping functions with respect to x_3 are in the same order as strains, that is, $w_i \sim h\epsilon$. Note that although partial derivative with respect to x_1 or x_2 will have the same dimension as strain, the warping functions cannot be in this order as it will lead $w_i{}'$ to be greater than ϵ and this conclusion can be proved when the expression of the warping functions are solved.

Assume the material constants have the order of μ. Then because of the equilibrium condition for plate structures, orders of external loads can be determined to be

$$\begin{aligned} hP_\alpha \sim \tau_\alpha \sim \beta_\alpha &\sim \mu\frac{h}{l}\epsilon \\ hP_3 \sim \tau_3 \sim \beta_3 &\sim \mu(\frac{h}{l})^2\epsilon \\ Q_\alpha &\sim \mu\epsilon \\ Q_3 &\sim \mu\frac{h}{l}\epsilon \end{aligned} \tag{3.2}$$

For piezoelectricity and temperature related quantities, it is straight forward to set the order of electric potential as $\phi \sim w_i \sim h\epsilon$, and piezoelectric coefficient and dielectric constants are in the order of μ. So from equation (2.31), one can conclude that $\alpha T \sim \epsilon$ and $pT \sim \mu\epsilon$. In the following sections energy expressions that are asymptotically correct in the corresponding order will be derived. Since warping functions are small, it is reasonable to have the characteristic scale of change of the displacement and warping functions with respect to time making $\mathcal{K}^*$ much smaller than other terms in equation (3.1), which can satisfy the case of low frequency dynamic problems. If the purpose is to seek static solutions, all kinetic energy terms can be disregarded in the process of dimensional reduction hereafter.

3.2 Zeroth-Order Reduction

In the zeroth-order reduction, the energy is expanded into the order of $(hl^2)\mu\epsilon^2$. It can be seen from expression (3.2) that all terms in the virtual work are smaller than the desired magnitude. As a result, equation (3.1) can be simplified to be

$$\int_{t_1}^{t_2} \left[\delta(\mathcal{K}_{2\mathrm{D}} - \int_\Omega \mathcal{H}_0 \mathrm{d}\Omega) + \overline{\delta\mathcal{W}}_{2\mathrm{D}}\right] \mathrm{d}t = 0 \tag{3.3}$$

where $\mathcal{H}_0$ is the area potential energy density that reduced to the zeroth-order.

3.2.1 Reduction Formulation

In zeroth-order approximation, it is obvious that warping functions w_i and electric potential ϕ only appears in the area potential energy density, so it is more convenient to directly work on $\mathcal{H}_0$ to obtain its asymptotically correct expression in the order of $\mu\epsilon^2$. By dropping higher order terms in equation (2.31), which are derivatives with respect to x_α, $\mathcal{H}_0$ can be obtained as

$$\begin{aligned}
2\mathcal{H}_0 = & \left\langle (\epsilon + x_3\kappa)^{\mathrm{T}} C_e (\epsilon + x_3\kappa) + {w_\parallel}'^{\mathrm{T}} C_s {w_\parallel}' + {w_3}'^{\mathrm{T}} C_t {w_3}' \right\rangle \\
& + 2\left\langle (\epsilon + x_3\kappa)^{\mathrm{T}} C_{es} {w_\parallel}' + (\epsilon + x_3\kappa)^{\mathrm{T}} C_{et} {w_3}' + {w_\parallel}'^{\mathrm{T}} C_{st} {w_3}' \right\rangle \\
& + 2\left\langle (\epsilon + x_3\kappa)^{\mathrm{T}} e_{et}\phi' + {w_\parallel}'^{\mathrm{T}} e_a \phi' + {w_3}'^{\mathrm{T}} e_t \phi' \right\rangle - \left\langle \phi'^{\mathrm{T}} d_t \phi' \right\rangle \\
& - 2\left\langle T\left[(\epsilon + x_3\kappa)^{\mathrm{T}} C_e \alpha_e + {w_\parallel}'^{\mathrm{T}} C_{es}^{\mathrm{T}} \alpha_e + {w_3}'^{\mathrm{T}} C_{et}^{\mathrm{T}} \alpha_e \right] \right\rangle \\
& - 2\left\langle T\left[(\epsilon + x_3\kappa)^{\mathrm{T}} C_{es} \alpha_s + {w_\parallel}'^{\mathrm{T}} C_s \alpha_s + {w_3}'^{\mathrm{T}} C_{st}^{\mathrm{T}} \alpha_s \right] \right\rangle \\
& - 2\left\langle T\left[(\epsilon + x_3\kappa)^{\mathrm{T}} C_{et} \alpha_t + {w_\parallel}'^{\mathrm{T}} C_{st} \alpha_t + {w_3}'^{\mathrm{T}} C_t \alpha_t \right] \right\rangle \\
& + 2\left\langle T\phi'^{\mathrm{T}} p_t \right\rangle + \lambda_\parallel \left\langle w_\parallel - \frac{c_\parallel}{h} \right\rangle + \lambda_3 \left\langle w_3 \right\rangle
\end{aligned} \tag{3.4}$$

where $\lambda_\parallel$ and λ_3 are Lagrange multipliers for introducing the constraints in equation (2.6). Then a simplified version of equation (3.3) can be expressed as

$$\delta\mathcal{H}_0 = 0 \tag{3.5}$$

The variation can be calculated to be

$$\begin{aligned}\delta\mathcal{H}_0 = \Big\langle &\big[(\varepsilon + x_3\kappa)^{\mathrm{T}} C_{es} + {w_\parallel}'^{\mathrm{T}} C_s + {w_3}' C_{st}^{\mathrm{T}} + \phi' e_a^{\mathrm{T}} \\ &- (\alpha_e^{\mathrm{T}} C_{es} + \alpha_s^{\mathrm{T}} C_s + \alpha_t C_{st}^{\mathrm{T}}) T\big] \delta {w_\parallel}' \\ &+ \big[(\varepsilon + x_3\kappa)^{\mathrm{T}} C_{et} + {w_\parallel}'^{\mathrm{T}} C_{st} + {w_3}' C_t + \phi' e_t \\ &- (\alpha_e^{\mathrm{T}} C_{et} + \alpha_s^{\mathrm{T}} C_{st} + \alpha_t C_t) T\big] \delta {w_3}' \\ &+ \big[(\varepsilon + x_3\kappa)^{\mathrm{T}} e_{et} + {w_\parallel}'^{\mathrm{T}} e_a + {w_3}' e_t - \phi' d_t + p_t T\big] \delta\phi' \Big\rangle \\ &+ \lambda_\parallel \langle \delta w_\parallel \rangle + \lambda_3 \langle \delta w_3 \rangle\end{aligned} \tag{3.6}$$

Using integration by parts, this variation statement has the following Euler-Lagrange equations corresponding to $w_\parallel$, w_3 and ϕ

$$\begin{aligned}\big[(\epsilon + x_3\kappa)^{\mathrm{T}} C_{es} + {w_\parallel}'^{\mathrm{T}} C_s + {w_3}' C_{st}^{\mathrm{T}} + \phi' e_a^{\mathrm{T}} \\ -(\alpha_e^{\mathrm{T}} C_{es} + \alpha_s^{\mathrm{T}} C_s + \alpha_t C_{st}^{\mathrm{T}}) T\big]' = \lambda_\parallel\end{aligned} \tag{3.7}$$

$$\begin{aligned}\big[(\epsilon + x_3\kappa)^{\mathrm{T}} C_{et} + {w_\parallel}'^{\mathrm{T}} C_{st} + {w_3}' C_t + \phi' e_t \\ -(\alpha_e^{\mathrm{T}} C_{et} + \alpha_s^{\mathrm{T}} C_{st} + \alpha_t C_t) T\big]' = \lambda_3\end{aligned} \tag{3.8}$$

$$\big[(\epsilon + x_3\kappa)^{\mathrm{T}} e_{et} + {w_\parallel}'^{\mathrm{T}} e_a + {w_3}' e_t - \phi' d_t + p_t T\big]' = 0 \tag{3.9}$$

with the boundary conditions

$$\begin{aligned}\big[(\epsilon + x_3\kappa)^{\mathrm{T}} C_{es} + {w_\parallel}'^{\mathrm{T}} C_s + {w_3}' C_{st}^{\mathrm{T}} + \phi' e_a^{\mathrm{T}} \\ -(\alpha_e^{\mathrm{T}} C_{es} + \alpha_s^{\mathrm{T}} C_s + \alpha_t C_{st}^{\mathrm{T}}) T\big]^+ = 0 \\ \big[(\epsilon + x_3\kappa)^{\mathrm{T}} C_{es} + {w_\parallel}'^{\mathrm{T}} C_s + {w_3}' C_{st}^{\mathrm{T}} + \phi' e_a^{\mathrm{T}} \\ -(\alpha_e^{\mathrm{T}} C_{es} + \alpha_s^{\mathrm{T}} C_s + \alpha_t C_{st}^{\mathrm{T}}) T\big]^- = 0\end{aligned} \tag{3.10}$$

$$\begin{aligned}\big[(\epsilon + x_3\kappa)^{\mathrm{T}} C_{et} + {w_\parallel}'^{\mathrm{T}} C_{st} + {w_3}' C_t + \phi' e_t \\ -(\alpha_e^{\mathrm{T}} C_{et} + \alpha_s^{\mathrm{T}} C_{st} + \alpha_t C_t) T\big]^+ = 0 \\ \big[(\epsilon + x_3\kappa)^{\mathrm{T}} C_{et} + {w_\parallel}'^{\mathrm{T}} C_{st} + {w_3}' C_t + \phi' e_t \\ -(\alpha_e^{\mathrm{T}} C_{et} + \alpha_s^{\mathrm{T}} C_{st} + \alpha_t C_t) T\big]^- = 0\end{aligned} \tag{3.11}$$

$$\begin{aligned}\big[(\epsilon + x_3\kappa)^{\mathrm{T}} e_{et} + {w_\parallel}'^{\mathrm{T}} e_a + {w_3}' e_t - \phi' d_t + p_t T\big]^+ = 0, \quad \text{if } \delta\phi^+ \neq 0 \\ \big[(\epsilon + x_3\kappa)^{\mathrm{T}} e_{et} + {w_\parallel}'^{\mathrm{T}} e_a + {w_3}' e_t - \phi' d_t + p_t T\big]^- = 0, \quad \text{if } \delta\phi^- \neq 0\end{aligned} \tag{3.12}$$

Warping functions w_i are free to vary at the top and bottom surfaces so $\delta {w_i}^+$ and $\delta {w_i}^-$ should not be zero at those locations and boundary conditions (3.10) and (3.11) must be satisfied. However, electric potential is free to vary at the top and bottom surfaces only when it is not prescribed at those locations. If it is prescribed, electric potential is no longer a variable at the location so $\delta\phi^+$ or $\delta\phi^-$ will always be zero and the expressions in equation (3.12) are not necessarily zero.

Integrating equations (3.7), (3.8) and (3.9), and substitute the boundary conditions, it can be easily solved that Lagrange multipliers $\lambda_\parallel = \lambda_3 = 0$. Then, Euler-Lagrange equations can be rewritten as

$$\begin{aligned}(\epsilon + x_3\kappa)^{\mathrm{T}} C_{es} + {w_\parallel}'^{\mathrm{T}} C_s + {w_3}' C_{st}^{\mathrm{T}} + \phi' e_a^{\mathrm{T}} \\ -(\alpha_e^{\mathrm{T}} C_{es} + \alpha_s^{\mathrm{T}} C_s + \alpha_t C_{st}^{\mathrm{T}}) T = 0\end{aligned} \tag{3.13}$$

$$\begin{aligned}(\epsilon + x_3\kappa)^{\mathrm{T}} C_{et} + {w_\parallel}'^{\mathrm{T}} C_{st} + {w_3}' C_t + \phi' e_t \\ -(\alpha_e^{\mathrm{T}} C_{et} + \alpha_s^{\mathrm{T}} C_{st} + \alpha_t C_t) T = 0\end{aligned} \tag{3.14}$$

$$(\epsilon + x_3\kappa)^{\mathrm{T}} e_{et} + {w_\parallel}'^{\mathrm{T}} e_a + {w_3}' e_t - \phi' d_t + p_t T = \mathcal{P} \tag{3.15}$$

where $\mathcal{P}$ is an arbitrary function independent about x_3 generated by indefinite integration. When the plate has multiple layers, the material constants in the Euler-Lagrange equations may be different from layer to layer while the material constants in the boundary conditions are always corresponding to the top and bottom layer. Besides, left hand side of equations (3.13), (3.14) and (3.15) must be continuous at the interfaces between layers to ensure the terms at interfaces generated by integration by parts to vanish. Since the material constants vary layerwise, the warping functions w_i, electric potential ϕ as well as the integration constant $\mathcal{P}$ can be different in different layers. However, because of the physical meaning of warping functions and electric potential, they must be continuous at the interfaces between layers. Expressions of the warping function and electric potential can be solved from equations (3.13), (3.14) and (3.15), giving

$${w_\parallel}'^{\mathrm{T}} = -(\epsilon + x_3\kappa - \alpha_e T)^{\mathrm{T}} C_{es}^{**} C_s^{-1} + \mathcal{P}\frac{e_a^{*\mathrm{T}} C_s^{-1}}{d_t^*} - p_t^* T \frac{e_a^{*\mathrm{T}} C_s^{-1}}{d_t^*} + \alpha_s^{\mathrm{T}} T \tag{3.16}$$

$$w_3{}' = -(\epsilon + x_3\kappa - \alpha_e T)^{\mathrm{T}} C_{et}^{**} C_t^{*-1} + \mathcal{P}\frac{e_t^* C_t^{*-1}}{d_t^*} - p_t^* T \frac{e_t^* C_t^{*-1}}{d_t^*} + \alpha_t T \tag{3.17}$$

$$\phi' = (\epsilon + x_3\kappa - \alpha_e T)^{\mathrm{T}} \frac{e_{et}^*}{d_t^*} - \mathcal{P}\frac{1}{d_t^*} + p_t^* T \frac{1}{d_t^*} \tag{3.18}$$

where the starred quantities are introduced for simplifying the expression. They can be expressed in terms of material constants including elastic constants, piezoelectric coefficient, dielectric constants, thermal expansion coefficient and pyroelectric coefficient, that is

$$\begin{aligned}
C_{et}^* &= C_{et} - C_{es} C_s^{-1} C_{st} \\
C_t^* &= C_t - C_{st}^{\mathrm{T}} C_s^{-1} C_{st} \\
C_{es}^* &= C_{es} - \frac{C_{et}^* C_{st}^{\mathrm{T}}}{C_t^*} \\
C_{et}^{**} &= C_{et}^* + \frac{e_{et}^* e_t^*}{d_t^*} \\
C_{es}^{**} &= C_{es}^* + \frac{e_{et}^* e_a^{*\mathrm{T}}}{d_t^*} \\
e_t^* &= e_t - e_a^{\mathrm{T}} C_s^{-1} C_{st} \\
e_a^* &= e_a - \frac{C_{st} e_t^*}{C_t^*} \\
e_{et}^* &= e_{et} - C_{es}^* C_s^{-1} e_a - \frac{C_{et}^* e_t}{C_t^*} \\
d_t^* &= d_t + e_a^{*\mathrm{T}} C_s^{-1} e_a + \frac{e_t^* e_t}{C_t^*} \\
p_t^* &= p_t + \alpha_e^{\mathrm{T}} e_{et} + \alpha_s^{\mathrm{T}} e_a + \alpha_t e_t
\end{aligned} \tag{3.19}$$

Note that the expressions in equations (3.16), (3.17), (3.18) and (3.19) are not unique even though the solution for $w_\parallel$, w_3 and ϕ is unique for every layer. The expressions depend on the procedure of solving equation (3.13), (3.14) and (3.15) but they must be the same when all starred quantities are completely expanded. Although solutions for warping functions and electric potential are expressed in the form of derivatives with respect to x_3 here, their explicit expression can be easily obtained by doing the integral and utilizing continuous condition at the interfaces along with the constraints in equation (2.6) or prescribed electric potential at certain surfaces or interfaces. Here

it can be observed that warping functions $w_i \sim h\epsilon$, justifying the setting in last the section.

It is impossible to determine a most general expression of function $\mathcal{P}$, but a most general form of function $\mathcal{P}$ can be given out to be

$$\mathcal{P} = \epsilon^{\mathrm{T}}\mathcal{P}_{\epsilon} + \kappa^{\mathrm{T}}\mathcal{P}_{\kappa} + \mathcal{P}_{\phi} \tag{3.20}$$

Specially, if electric potential is specified at top and bottom interfaces of a certain layer, integrate equation (3.18), giving

$$\phi = (x_3\epsilon + \frac{1}{2}{x_3}^2\kappa - \alpha_e \int T\mathrm{d}x_3)^{\mathrm{T}} \frac{e_{et}^*}{d_t^*} - \mathcal{P}\frac{x_3}{d_t^*} + p_t^* \frac{1}{d_t^*} \int T\mathrm{d}x_3 + \mathcal{P}_1 \tag{3.21}$$

where $\mathcal{P}_1$ is another arbitrary function independent from x_3 and

$$\begin{aligned} &\text{at } x_3 = h_a,\ \phi = V_a \\ &\text{at } x_3 = h_b,\ \phi = V_b \end{aligned} \tag{3.22}$$

where V_a and V_b are specified electric potential. Let

$$\bar{T}\left(x_1, x_2, x_3\right) = \int T\mathrm{d}x_3 \tag{3.23}$$

and

$$\begin{aligned} \bar{T}\left(x_1, x_2, h_a\right) &= \bar{T}_a \\ \bar{T}\left(x_1, x_2, h_b\right) &= \bar{T}_b \end{aligned} \tag{3.24}$$

function $\mathcal{P}$ can be solved to be

$$\mathcal{P} = \epsilon^{\mathrm{T}} e_{et}^* + \frac{h_a + h_b}{2}\kappa^{\mathrm{T}} e_{et}^* - \frac{\bar{T}_b - \bar{T}_a}{h_b - h_a}\alpha_e^{\mathrm{T}} e_{et}^* + \frac{\bar{T}_b - \bar{T}_a}{h_b - h_a} p_t^* - \frac{V_b - V_a}{h_b - h_a} d_t^* \tag{3.25}$$

then

$$\begin{aligned} \mathcal{P}_{\epsilon} &= e_{et}^* \\ \mathcal{P}_{\kappa} &= \frac{h_a + h_b}{2} e_{et}^* \\ \mathcal{P}_{\phi} &= \frac{\bar{T}_b - \bar{T}_a}{h_b - h_a}\left(p_t^* - \alpha_e^{\mathrm{T}} e_{et}^*\right) - \frac{V_b - V_a}{h_b - h_a} d_t^* \end{aligned} \tag{3.26}$$

Though this solution is derived based on specific conditions, it is general enough in practical use as electrodes are usually coated on the top and bottom interfaces of the piezoelectric layers and electric potentials are specified when the piezoelectric layers are designed as actuators.

Before substituting the solution of warping functions and electric potential back into the area potential energy density, it is helpful to simplify $\mathcal{H}_0$ using the Euler-Lagrange equations, which gives

$$\begin{aligned} 2\mathcal{H}_0 = & \left\langle (\epsilon + x_3\kappa - \alpha_e T)^{\mathrm{T}} C_e (\epsilon + x_3\kappa) + (w_\parallel{}' - \alpha_s T)^{\mathrm{T}} C_{es}^{\mathrm{T}} (\epsilon + x_3\kappa) \right\rangle \\ & + \left\langle (w_3{}' - \alpha_t T) C_{et}^{\mathrm{T}} (\epsilon + x_3\kappa) + \phi' e_{et}^{\mathrm{T}} (\epsilon + x_3\kappa) \right\rangle \\ & - \left\langle T \left[(\epsilon + x_3\kappa)^{\mathrm{T}} C_e \alpha_e + w_\parallel{}'^{\mathrm{T}} C_{es}^{\mathrm{T}} \alpha_e + w_3{}' C_{et}^{\mathrm{T}} \alpha_e \right] \right\rangle \\ & - \left\langle T \left[(\epsilon + x_3\kappa)^{\mathrm{T}} C_{es} \alpha_s + w_\parallel{}'^{\mathrm{T}} C_s \alpha_s + w_3{}' C_{st}^{\mathrm{T}} \alpha_s \right] \right\rangle \\ & - \left\langle T \left[(\epsilon + x_3\kappa)^{\mathrm{T}} C_{et} \alpha_t + w_\parallel{}'^{\mathrm{T}} C_{st} \alpha_t + w_3{}' C_t \alpha_t \right] \right\rangle \\ & + \langle T\phi' p_t \rangle + \left\langle (\epsilon^{\mathrm{T}} P_\epsilon + \kappa^{\mathrm{T}} P_\kappa + P_\phi)\phi' \right\rangle \end{aligned} \tag{3.27}$$

Substituting equations (3.16), (3.17)and (3.18) into equation (3.27), the zeroth-order asymptotically correct expression of the potential energy density can be obtained as

$$2\mathcal{H}_0 = \begin{Bmatrix} \epsilon \\ \kappa \end{Bmatrix}^{\mathrm{T}} \begin{bmatrix} A^* & B^* \\ B^{*\mathrm{T}} & D^* \end{bmatrix} \begin{Bmatrix} \epsilon \\ \kappa \end{Bmatrix} - 2 \begin{Bmatrix} S_\epsilon \\ S_\kappa \end{Bmatrix}^{\mathrm{T}} \begin{Bmatrix} \epsilon \\ \kappa \end{Bmatrix} \tag{3.28}$$

with

$$\begin{aligned} A^* &= \left\langle C_e^* - \frac{\mathcal{P}_\epsilon \mathcal{P}_\epsilon^{\mathrm{T}}}{d_t^*} \right\rangle \\ B^* &= \left\langle x_3 C_e^* - \frac{\mathcal{P}_\epsilon \mathcal{P}_\kappa^{\mathrm{T}}}{d_t^*} \right\rangle \\ D^* &= \left\langle {x_3}^2 C_e^* - \frac{\mathcal{P}_\kappa \mathcal{P}_\kappa^{\mathrm{T}}}{d_t^*} \right\rangle \end{aligned} \tag{3.29}$$

and

$$\begin{aligned} S_\epsilon &= \left\langle \frac{\mathcal{P}_\epsilon \mathcal{P}_\phi^{\mathrm{T}}}{d_t^*} + T \left[C_e^* \alpha_e - \frac{e_{et}^*}{d_t^*} p_t^* \right] \right\rangle \\ S_\kappa &= \left\langle \frac{\mathcal{P}_\kappa \mathcal{P}_\phi^{\mathrm{T}}}{d_t^*} + T \left[x_3 C_e^* \alpha_e - x_3 \frac{e_{et}^*}{d_t^*} p_t^* \right] \right\rangle \end{aligned} \tag{3.30}$$

where

$$C_e^* = C_e - C_{es}^* C_s^{-1} C_{es}^{\mathrm{T}} - \frac{C_{et}^* C_{et}^{\mathrm{T}}}{C_t^*} + \frac{e_{et}^* e_{et}^{*\mathrm{T}}}{d_t^*} \tag{3.31}$$

Terms relating only to material constants, temperature change or prescribed electric potential are all dropped during the derivation because they will not affect the total energy when the plate is deformed. It can be found apparently from equation (3.29) that the stiffness matrices A^*, B^* and D^* not only depend on material elastic constants, but also piezoelectric coefficients and dielectric constants. Temperature change and applied electric field can affect the values of S_ϵ and S_κ, which provide additional contributions to the total potential energy.

Up to this point, the original 3D problem has been reduced to a 2D plate problem with the constitutive relation in equation (3.28). By defining the force resultants $\mathcal{N}$ and moment resultants $\mathcal{M}$ due to in-plane membrane strains and bending strains, that is

$$\begin{aligned} \mathcal{N} &= \frac{\partial \mathcal{H}_0}{\partial \epsilon} \\ \mathcal{M} &= \frac{\partial \mathcal{H}_0}{\partial \kappa} \end{aligned} \tag{3.32}$$

an equivalent plate energetics can be obtain as

$$\left\{ \begin{array}{c} \mathcal{N} \\ \mathcal{M} \end{array} \right\} = \left[\begin{array}{cc} A^* & B^* \\ B^{*\mathrm{T}} & D^* \end{array} \right] \left\{ \begin{array}{c} \epsilon \\ \kappa \end{array} \right\} - \left\{ \begin{array}{c} S_\epsilon \\ S_\kappa \end{array} \right\} \tag{3.33}$$

It is obvious that even though the plate is a piezoelectric smart plate, the 2D energetics has the same form as the classical laminated plate theory (CLPT) with thermal load except the temperature related term is extended to contain piezoelectric effect. Equation (3.33) can be directly applied in plate analyses based on the CLPT.

3.2.2 Recovery Relations

Using equation (3.33) along with boundary conditions, an accurate 2D plate solution can be obtain analytically or with the help of finite element analyses. While in many cases it is also valuable to acquire the 3D quantities of the plate structure.

In such situations, 3D fields are required to be recovered via the 2D results. For the zeroth-order approximation, the 3D strain field and electric field can be recovered by neglecting terms with derivatives with respect to x_α in equation (2.23) and (2.27), obtaining

$$\begin{aligned} \Gamma_e^0 &= \epsilon + x_3\kappa \\ 2\Gamma_s^0 &= {w_\parallel}' \\ \Gamma_t^0 &= {w_3}' \end{aligned} \tag{3.34}$$

and

$$\begin{aligned} E_s^0 &= 0 \\ E_t^0 &= -\phi' \end{aligned} \tag{3.35}$$

The 3D stress field and electric displacement field can be obtained by taking the derivatives of equation (2.31) with respect to 3D strain field and 3D electric field respectively, which gives

$$\begin{aligned} \begin{Bmatrix} \sigma_e \\ \sigma_s \\ \sigma_t \end{Bmatrix} = & \begin{bmatrix} C_e & C_{es} & C_{et} \\ C_{es}^{\mathrm{T}} & C_s & C_{st} \\ C_{et}^{\mathrm{T}} & C_{st}^{\mathrm{T}} & C_t \end{bmatrix} \begin{Bmatrix} \Gamma_e^0 \\ 2\Gamma_s^0 \\ \Gamma_t^0 \end{Bmatrix} - \begin{bmatrix} e_b & e_{et} \\ e_s & e_a \\ e_c & e_t \end{bmatrix} \begin{Bmatrix} E_s^0 \\ E_t^0 \end{Bmatrix} \\ & - \begin{bmatrix} C_e & C_{es} & C_{et} \\ C_{es}^{\mathrm{T}} & C_s & C_{st} \\ C_{et}^{\mathrm{T}} & C_{st}^{\mathrm{T}} & C_t \end{bmatrix} \begin{Bmatrix} \alpha_e \\ \alpha_s \\ a_t \end{Bmatrix} T \end{aligned} \tag{3.36}$$

$$\begin{Bmatrix} D_s \\ D_t \end{Bmatrix} = \begin{bmatrix} e_b & e_{et} \\ e_s & e_a \\ e_c & e_t \end{bmatrix}^{\mathrm{T}} \begin{Bmatrix} \Gamma_e^0 \\ 2\Gamma_s^0 \\ \Gamma_t^0 \end{Bmatrix} + \begin{bmatrix} d_s & d_{et} \\ d_{et}^{\mathrm{T}} & d_t \end{bmatrix} \begin{Bmatrix} E_s^0 \\ E_t^0 \end{Bmatrix} + \begin{Bmatrix} p_s \\ p_t \end{Bmatrix} T \tag{3.37}$$

with

$$\begin{aligned} \sigma_e &= \begin{bmatrix} \sigma_{11} & \sigma_{12} & \sigma_{22} \end{bmatrix}^{\mathrm{T}} \\ \sigma_s &= \begin{bmatrix} \sigma_{13} & \sigma_{23} \end{bmatrix}^{\mathrm{T}} \\ \sigma_t &= \sigma_{33} \end{aligned} \tag{3.38}$$

and

$$D_s = \begin{bmatrix} D_1 & D_2 \end{bmatrix}^{\mathrm{T}}$$
$$D_t = D_3 \tag{3.39}$$

where σ_{ij} are 3D stresses and D_i are 3D electric displacements.

From the second equation in (3.34) it can be found that the transverse shear strains are not zero, which means lines normal to the reference surface in the undeformed plate are no long normal in the deformed plate and since $w_\parallel{}'$ is a linear function through the thickness, the straightness of the normal lines disappears either. Besides, the third equation in (3.34) shows that the transverse normal strain is not zero, allowing thickness change when deformed. These two features differ the current model from the CLPT. Analyzing equation (3.36), it can be conclude that in-plane stresses can be easily calculated while transverse shear and normal stresses are identically zero because the expressions of σ_s and σ_t coincide the Euler-Lagrange equations in (3.13) and (3.14). This result is a direct deduction from the variational statement instead of a ad hoc assumption. Similarly, D_3 always equals to $\mathcal{P}$ because of Euler-Lagrange equation (3.15). Though at this stage transverse shear and normal stresses cannot be predicted, they can be estimated in a higher-order approximation.

3.3 First-Order Reduction

In previous section, the strains are in the order of $(\frac{h}{l})^0\epsilon$ and the energy expression is up to the order of $(hl^2)\mu\epsilon^2$. To improve the accuracy as well as predict transverse stresses, dimension reduction of the first-order is required. In this reduction, strains are expanded into the order of $\frac{h}{l}\epsilon$ and the resultant energy is in the order of $(hl^2)\mu(\frac{h}{l})^2\epsilon^2$. Then warping functions and electric potential are perturbed to be

$$\begin{aligned} w_\parallel &= w_\parallel^0 + v_\parallel + o\left(\frac{h^2}{l}\epsilon\right) \\ w_3 &= w_3^0 + v_3 + o\left(\frac{h^2}{l}\epsilon\right) \\ \phi &= \phi^0 + \varphi + o\left(\frac{h^2}{l}\epsilon\right) \end{aligned} \tag{3.40}$$

Note that up to this order virtual work of applied loads are not negligible, so total potential density can be defined as

$$\Pi = \mathcal{H} - W \tag{3.41}$$

with

$$W = \left\langle P_{\|}^{\mathrm{T}} w_{\|} \right\rangle + \tau_{\|}^{\mathrm{T}} w_{\|}^{+} + \beta_{\|}^{\mathrm{T}} w_{\|}^{-} + \langle P_3 w_3 \rangle + \tau_3 w_3^{+} + \beta_3 w_3^{-} \tag{3.42}$$

$$\delta \int_{\Omega} W \mathrm{d}\Omega = \overline{\delta \mathcal{W}}^{*} \tag{3.43}$$

then equation (3.1) can be simplified to be

$$\int_{t_1}^{t_2} \left[\delta(\mathcal{K}_{2\mathrm{D}} - \int_{\Omega} \Pi_1 \mathrm{d}\Omega) + \overline{\delta \mathcal{W}}_{2\mathrm{D}} \right] \mathrm{d}t = 0 \tag{3.44}$$

where Π_1 is reduced to the second order.

3.3.1 Reduction Formulation

In the zeroth-order approximation, the formulation is for complete anisotropic materials, which means all the terms in material constant matrices can be non-zero. This provides the best generality while making the formulation tedious in higher order derivation. Since most piezoelectric and composite materials present at least monoclinic symmetry about the mid-plane, it would be enough for practical use when applying this material symmetry. Consequently, C_{es} and C_{st} in the material elastic constant matrix, e_b, e_a and e_c in the piezoelectric coefficient matrix, d_{et} in the dielectric constant matrix and α_s in the thermal expansion coefficient matrix will always vanish. Then warping functions and electric potential in each layer solved during the zeroth-order reduction can be rewritten as

$$w_{\|}^{0} = 0 \tag{3.45}$$

$$w_3^{0} = C_{\perp} \mathcal{E} + w_{3e}^{0} \tag{3.46}$$

$$\phi^{0} = C_{\phi} \mathcal{E} + \phi_e^{0} \tag{3.47}$$

with

$$\mathcal{E} = \begin{bmatrix} \epsilon & \kappa \end{bmatrix}^{\mathrm{T}} \tag{3.48}$$

and

$$\begin{aligned} C_{\perp}{}' &= \left[-\frac{C_{et}^{**\mathrm{T}}}{C_t^*} + \frac{e_t^*}{d_t^* C_t^*}\mathcal{P}_{\epsilon}^{\mathrm{T}} \quad - x_3 \frac{C_{et}^{**\mathrm{T}}}{C_t^*} + \frac{e_t^*}{d_t^* C_t^*}\mathcal{P}_{\kappa}^{\mathrm{T}} \right] \\ w_{3e}^{0}{}' &= T\left(\frac{C_{et}^{**\mathrm{T}}\alpha_e}{C_t^*} - \frac{e_t^* p_t^*}{d_t^* C_t^*} + \alpha_t \right) + \frac{e_t^*}{d_t^* C_t^*}\mathcal{P}_{\phi} \end{aligned} \tag{3.49}$$

$$\begin{aligned} C_{\phi}{}' &= \left[\frac{e_{et}^{*\mathrm{T}}}{d_t^*} - \frac{1}{d_t^*}\mathcal{P}_{\epsilon}^{\mathrm{T}} \quad x_3 \frac{e_{et}^{*\mathrm{T}}}{d_t^*} - \frac{1}{d_t^*}\mathcal{P}_{\kappa}^{\mathrm{T}} \right] \\ \phi_e^{0\prime} &= T\left(-\frac{e_{et}^{*\mathrm{T}}\alpha_e}{d_t^*} + \frac{p_t^*}{d_t^*} \right) - \frac{1}{d_t^*}\mathcal{P}_{\phi} \end{aligned} \tag{3.50}$$

where the "0" in superscript denotes that the quantity is from the zeroth-order approximation.

Substituting equations (3.45), (3.46) and (3.47) back into equation (3.40), then equation (2.23), expression for Π to the second-order can be obtained using equations (3.41), (2.31) and (3.42), that is

$$\begin{aligned} 2\Pi_1 = & \left\langle (\epsilon + x_3\kappa)^{\mathrm{T}} C_e (\epsilon + x_3\kappa) + 2(\epsilon + x_3\kappa)^{\mathrm{T}} C_e I_\alpha v_{\parallel,\alpha} \right\rangle \\ & + \left\langle 2(\epsilon + x_3\kappa)^{\mathrm{T}} C_{et}(w_3^{0\prime} + v_3{}') + 2(I_\alpha v_{\parallel,\alpha})^{\mathrm{T}} C_{et} w_3^{0\prime} \right\rangle \\ & + \left\langle (v_\parallel{}' + e_\alpha w_{3,\alpha}^0)^{\mathrm{T}} C_s (v_\parallel{}' + e_\alpha w_{3,\alpha}^0) + (w_3^{0\prime} + v_3{}')^{\mathrm{T}} C_t (w_3^{0\prime} + v_3{}') \right\rangle \\ & + \left\langle 2(\epsilon + x_3\kappa)^{\mathrm{T}} e_{et}(\phi^{0\prime} + \varphi') + 2(I_\alpha v_{\parallel,\alpha})^{\mathrm{T}} e_{et}\phi^{0\prime} \right\rangle \\ & + \left\langle 2(v_\parallel{}' + e_\alpha w_{3,\alpha}^0)^{\mathrm{T}} e_s \phi_{,\parallel}^0 + 2(w_3^{0\prime} + v_3{}')^{\mathrm{T}} e_t (\phi^{0\prime} + \varphi') \right\rangle \\ & - \left\langle \phi_{,\parallel}^{0\mathrm{T}} d_s \phi_{,\parallel}^0 + (\phi^{0\prime} + \varphi')^{\mathrm{T}} d_t (\phi^{0\prime} + \varphi') \right\rangle \\ & - 2\left\langle T\left[(\epsilon + x_3\kappa + I_\alpha v_{\parallel,\alpha})^{\mathrm{T}} C_e \alpha_e + (w_3^{0\prime} + v_3{}')^{\mathrm{T}} C_{et}^{\mathrm{T}} \alpha_e \right] \right\rangle \\ & - 2\left\langle T\left[(\epsilon + x_3\kappa + I_\alpha v_{\parallel,\alpha})^{\mathrm{T}} C_{et} \alpha_t + (w_3^{0\prime} + v_3{}')^{\mathrm{T}} C_t \alpha_t \right] \right\rangle \\ & + 2\left\langle T\left[(\phi_{,\parallel}^0 + \varphi_{,\parallel})^{\mathrm{T}} p_s + (\phi^{0\prime} + \varphi')^{\mathrm{T}} p_t \right] \right\rangle \\ & - 2\left[\left\langle P_\parallel^{\mathrm{T}} v_\parallel \right\rangle + \tau_\parallel^{\mathrm{T}} v_\parallel^+ + \beta_\parallel^{\mathrm{T}} v_\parallel^- + \left\langle P_3 w_3^0 \right\rangle + \tau_3 w_3^{0+} + \beta_3 w_3^{0-} \right] \\ & + \bar{\lambda}_\parallel \left\langle v_\parallel - \frac{c_\parallel}{h} \right\rangle + \bar{\lambda}_3 \left\langle w_3^0 + v_3 \right\rangle \end{aligned} \tag{3.51}$$

where $\bar{\lambda}_\parallel$ and $\bar{\lambda}_3$ are Lagrange multiplier for introducing the constraints in equation (2.6) in the first-order approximation. Differing from the zeroth-order approximation, it is incorrect to drop off all strains of the second or higher order even though the warping functions and electric potential are perturbed only to the first-order, as the goal is to obtain the energy to the second order so a term combining second-order and zeroth-order strains should still be kept. Taking the variation of the total potential density and simplifying using the Euler-Lagrange equations in the zeroth-order reduction, gives

$$\begin{aligned}\delta\Pi_1 = \Big\langle & \big[(\epsilon + x_3\kappa - \alpha_e T)^{\mathrm{T}} C_e^* + (p_t^* T - \mathcal{P})\frac{e_{et}^{*\mathrm{T}}}{d_t^*}\big] I_\alpha \delta v_{\parallel,\alpha} \\ & + \big[(v_\parallel{}' + e_\alpha w_{3,\alpha}^0)^{\mathrm{T}} C_s + \phi_{,\parallel}^{0\mathrm{T}} e_s{}^{\mathrm{T}}\big]\delta v_\parallel{}' + \big[v_3{}' C_t + \varphi' e_t\big]\delta v_3{}' \\ & + \big[p_s^{\mathrm{T}} T\big]\delta\varphi_{,\parallel} + \big[P + v_3{}' e_t - \varphi' d_t\big]\delta\varphi' \Big\rangle \\ & - \big\langle P_\parallel^{\mathrm{T}}\delta v_\parallel\big\rangle - \tau_\parallel^{\mathrm{T}}\delta v_\parallel^+ - \beta_\parallel^{\mathrm{T}}\delta v_\parallel^- + \big\langle\bar{\lambda}_\parallel\delta v_\parallel\big\rangle + \big\langle\bar{\lambda}_3\delta v_3\big\rangle\end{aligned} \tag{3.52}$$

Note that in the first-order approximation, warping functions w_i^0 and ϕ^0 are already solved in the zero-order approximation and should not be considered as varying functions, so they are not taken the variation. Using integration by parts for both the thickness coordinate and in-plane coordinates, the Euler-Lagrange equations can be derived to be

$$\big[C_s(v_\parallel{}' + e_\alpha w_{3,\alpha}^0) + e_s\phi_{,\parallel}^0\big]' = D_\alpha{}'\mathcal{E}_{,\alpha} + g' + \bar{\lambda}_\parallel \tag{3.53}$$

$$\big[v_3{}' C_t + \varphi' e_t\big]' = \bar{\lambda}_3 \tag{3.54}$$

$$\big[v_3{}' e_t - \varphi' d_t\big]' = -T_{,\parallel}{}^{\mathrm{T}} p_s \tag{3.55}$$

with boundary conditions

$$\begin{aligned}\big[C_s(v_\parallel{}' + e_\alpha w_{3,\alpha}^0) + e_s\phi_{,\parallel}^0\big]^+ &= \tau_\parallel \\ \big[C_s(v_\parallel{}' + e_\alpha w_{3,\alpha}^0) + e_s\phi_{,\parallel}^0\big]^- &= \beta_\parallel\end{aligned} \tag{3.56}$$

$$\begin{aligned}\big[v_3{}' C_t + \varphi' e_t\big]^+ &= 0 \\ \big[v_3{}' C_t + \varphi' e_t\big]^- &= 0\end{aligned} \tag{3.57}$$

$$\begin{aligned}\left[{v_3}'e_t - \varphi' d_t\right]^+ &= 0, \quad \text{if } \delta\varphi^+ \neq 0 \\ \left[{v_3}'e_t - \varphi' d_t\right]^- &= 0, \quad \text{if } \delta\varphi^- \neq 0\end{aligned} \tag{3.58}$$

where

$${D_\alpha}' = -I_\alpha^{\mathrm{T}} \begin{bmatrix} C_e^* - \dfrac{e_{et}^*}{d_t^*}\mathcal{P}_\epsilon^{\mathrm{T}} & x_3 C_e^* - \dfrac{e_{et}^*}{d_t^*}\mathcal{P}_\kappa^{\mathrm{T}} \end{bmatrix} \tag{3.59}$$

$$g' = I_\alpha^{\mathrm{T}} \left(T_{,\alpha} C_e^* \alpha_e - \frac{e_{et}^*}{d_t^*}\mathcal{P}_{\phi,\alpha} + T_{,\alpha} p_t^* \frac{e_{et}^*}{d_t^*} \right) - P_\parallel \tag{3.60}$$

The boundary conditions in equations (3.56), (3.57) and (3.58) come from integration by parts about x_3 coordinate. Boundary terms generated by integration by parts about the x_α coordinates can be transformed to integrals on the lateral boundaries, which is not considered as the study aims at seeking an internal solution, using divergence theorem. As a result, integration by parts with respect to the in-plane coordinates can be arbitrarily adopted when convenient in the following derivation.

From equations (3.53), (3.54) and (3.55), it can be found that $v_\parallel$ is decoupled from v_3 and φ, so they can be solved separately. Integrating equation (3.54) with respect to x_3 and using boundary condition in equation (3.57), it can be solved that $\bar{\lambda}_3 = 0$. Then equation (3.54) and (3.55) can be rewritten as

$${v_3}' C_t + \varphi' e_t = 0 \tag{3.61}$$

$${v_3}' e_t - \varphi' d_t = -\theta_\parallel^{\mathrm{T}} p_s + \hat{\mathcal{P}} \tag{3.62}$$

where $\hat{\mathcal{P}}$ is a function independent from x_3 generated by the integral, and $\theta_\parallel$ is introduced for simplifying the notation, which is defined as

$$\theta_\parallel = \int T_{,\parallel} \mathrm{d}x_3 \tag{3.63}$$

Solving equation (3.61) and (3.62) gives

$${v_3}' = -(\theta_\parallel^{\mathrm{T}} p_s - \hat{\mathcal{P}}) \frac{e_t}{d_t^* C_t} \tag{3.64}$$

$$\varphi' = (\theta_\parallel^{\mathrm{T}} p_s - \hat{\mathcal{P}}) \frac{1}{d_t^*} \tag{3.65}$$

whose order satisfy the perturbation of $v_i \sim h(h/l)\epsilon$.

The expression of $\hat{\mathcal{P}}$ can be derived when electric potential is prescribed on the top and bottom interfaces of a layer. Since the prescribed electric potential is completely included in ϕ^0 at the location, φ is always zero at the prescribed position, so

$$(p_s^{\mathrm{T}}\bar{\theta}_{\|} - x_3\hat{\mathcal{P}})\frac{1}{d_t^*} + \hat{\mathcal{P}}_1 = 0 \quad \text{at } x_3 = h_a \text{ and } x_3 = h_b \tag{3.66}$$

then

$$\hat{\mathcal{P}} = p_s^{\mathrm{T}}\frac{\bar{\theta}_{\|}(x_1, x_2, h_a) - \bar{\theta}_{\|}(x_1, x_2, h_b)}{h_a - h_b} \tag{3.67}$$

where

$$\bar{\theta}_{\|}(x_1, x_2, x_3) = \int \theta_{\|}\mathrm{d}x_3 \tag{3.68}$$

If the temperature change is a constant along the in-plane direction, $\hat{\mathcal{P}}$ will vanish and v_3 and φ will become zero, which means the results of warping function w_3 and electric potential ϕ will be the same as the zeroth-order reduction.

Warping functions $v_{\|}$ can be solved using equation (3.53). Integrating with respect to x_3, gives

$$C_s({v_{\|}}' + e_\alpha w_{3,\alpha}^0) + e_s\phi_{,\|}^0 = D_\alpha\mathcal{E}_{,\alpha} + g + \bar{\lambda}_{\|}x_3 + \bar{\Lambda}_{\|} \tag{3.69}$$

Substituting the boundary condition in equation (3.56), Lagrange multipliers can be solved to be

$$\bar{\lambda}_{\|} = \frac{1}{h}\left(\tau_{\|} + \beta_{\|} - D_\alpha^+\mathcal{E}_{,\alpha} + D_\alpha^-\mathcal{E}_{,\alpha} - g^+ + g^-\right) \tag{3.70}$$

$$\bar{\Lambda}_{\|} = \frac{1}{2}\left(\tau_{\|} - \beta_{\|} - D_\alpha^+\mathcal{E}_{,\alpha} - D_\alpha^-\mathcal{E}_{,\alpha} - g^+ - g^-\right) \tag{3.71}$$

Substituting equation (3.70) and (3.71) back into equation (3.69), it can be derived that

$${v_{\|}}' = C_s^{-1}D_\alpha^*\mathcal{E}_{,\alpha} + C_s^{-1}g^* \tag{3.72}$$

where

$$D_\alpha^* = D_\alpha - C_s e_\alpha C_\perp - e_s e_\alpha C_\phi - \left(\frac{x_3}{h} + \frac{1}{2}\right)D_\alpha^+ + \left(\frac{x_3}{h} - \frac{1}{2}\right)D_\alpha^- \tag{3.73}$$

$$\begin{aligned} g^* = g - C_s e_\alpha w_{3e,\alpha}^0 - e_s e_\alpha \phi_{e,\alpha}^0 + \left(\frac{x_3}{h} + \frac{1}{2}\right)\tau_{\|} + \left(\frac{x_3}{h} - \frac{1}{2}\right)\beta_{\|} \\ - \left(\frac{x_3}{h} + \frac{1}{2}\right)g^+ + \left(\frac{x_3}{h} - \frac{1}{2}\right)g^- \end{aligned} \tag{3.74}$$

Left hand side of equation (3.69) must be continuous through the thickness to eliminate terms about the interfaces generated by integration by parts and consequently D_α and g are also continuous through the thickness. Integrate equation (3.72), $v_\parallel$ can be expressed as

$$v_\parallel = (\bar{D}_\alpha + L_\alpha)\mathcal{E}_{,\alpha} + \bar{g} \tag{3.75}$$

with

$$\bar{D}'_\alpha = C_s^{-1} D^*_\alpha \tag{3.76}$$

$$\bar{g}' = C_s^{-1} g^* \tag{3.77}$$

where L_α are constants generated by integral and will be used as optimization parameters during transforming the model to a Reissner-Mindlin like form. In order to satisfy the constraints in equation (2.6), coefficients in equation (3.75) should have

$$\begin{aligned} \left\langle \bar{D}_\alpha \right\rangle &= 0 \\ \langle \bar{g} \rangle &= 0 \\ L_\alpha \mathcal{E}_{,\alpha} &= \frac{c_\parallel}{h} \end{aligned} \tag{3.78}$$

Expression of $\bar{D}_\alpha$ and $\bar{g}$ can be solved using equations (3.76), (3.77), (3.78) and continuity condition.

Simplifying equation (3.51) using the Euler-Lagrange equations and plugging the solution of warping functions and electric potential in, the asymptotically correct expression of the total potential density Π_1 to the second-order is

$$2\Pi_1 = \mathcal{E}^{\mathrm{T}} A \mathcal{E} + \mathcal{E}_{,1}^{\mathrm{T}} B \mathcal{E}_{,1} + 2\mathcal{E}_{,1}^{\mathrm{T}} C \mathcal{E}_{,2} + \mathcal{E}_{,2}^{\mathrm{T}} D \mathcal{E}_{,2} - 2\mathcal{E}^{\mathrm{T}} F \tag{3.79}$$

where

$$A = \begin{bmatrix} A^* & B^* \\ B^{*\mathrm{T}} & D^* \end{bmatrix} \tag{3.80}$$

$$\begin{aligned} B = \big\langle & - D_1^{*\mathrm{T}} C_s^{-1} D_1^* + C_{s(11)} C_\perp^{\mathrm{T}} C_\perp + e_{s(11)} C_\perp^{\mathrm{T}} C_\phi \\ & + e_{s(11)} C_\phi^{\mathrm{T}} C_\perp - d_{s(11)} C_\phi^{\mathrm{T}} C_\phi \big\rangle + \big\langle {D_1'}^{\mathrm{T}} \big\rangle L_1 + L_1^{\mathrm{T}} \big\langle D_1' \big\rangle \end{aligned} \tag{3.81}$$

$$C = \Big\langle -D_1^{*\mathrm{T}} C_s^{-1} D_2^* + C_{s(12)} C_\perp^{\mathrm{T}} C_\perp + e_{s(12)} C_\perp^{\mathrm{T}} C_\phi + e_{s(12)} C_\phi^{\mathrm{T}} C_\perp - d_{s(12)} C_\phi^{\mathrm{T}} C_\phi \Big\rangle + \big\langle {D_1'}^{\mathrm{T}} \big\rangle L_2 + L_1^{\mathrm{T}} \big\langle D_2' \big\rangle \tag{3.82}$$

$$D = \Big\langle -D_2^{*\mathrm{T}} C_s^{-1} D_2^* + C_{s(22)} C_\perp^{\mathrm{T}} C_\perp + e_{s(22)} C_\perp^{\mathrm{T}} C_\phi + e_{s(22)} C_\phi^{\mathrm{T}} C_\perp - d_{s(22)} C_\phi^{\mathrm{T}} C_\phi \Big\rangle + \big\langle {D_2'}^{\mathrm{T}} \big\rangle L_2 + L_2^{\mathrm{T}} \big\langle D_2' \big\rangle \tag{3.83}$$

$$\begin{aligned} F = S_{\epsilon\kappa} + \Big\langle & - R_{\epsilon\kappa} - D_\alpha^{*\mathrm{T}} C_s^{-1} g_{,\alpha}^* + \big[p_{s(\alpha)} C_\phi^{\mathrm{T}} T \big]_{,\alpha} \\ & + \big[C_{s(\alpha\beta)} C_\perp^{\mathrm{T}} w_{3e}^0 + e_{s(\alpha\beta)} C_\perp^{\mathrm{T}} \phi_e^0 + e_{s(\alpha\beta)} C_\phi^{\mathrm{T}} w_{3e}^0 - d_{s(\alpha\beta)} C_\phi^{\mathrm{T}} \phi_e^0 \big]_{,\alpha\beta} \Big\rangle \\ & + \big\langle C_\perp^{\mathrm{T}} P_3 \big\rangle + C_\perp^{+\mathrm{T}} \tau_3 + C_\perp^{-\mathrm{T}} \beta_3 - L_\alpha^{\mathrm{T}} \Big(\tau_\parallel + \beta_\parallel - \big\langle g' \big\rangle \Big)_{,\alpha} \end{aligned} \tag{3.84}$$

with

$$S_{\epsilon\kappa} = \left\{ \begin{array}{c} S_\epsilon \\ S_\kappa \end{array} \right\} \tag{3.85}$$

$$R_{\epsilon\kappa} = \left\{ \begin{array}{c} \mathcal{P}_\epsilon \big(\theta_\parallel^{\mathrm{T}} p_s - \hat{\mathcal{P}} \big) / d_t^* \\ \mathcal{P}_\kappa \big(\theta_\parallel^{\mathrm{T}} p_s - \hat{\mathcal{P}} \big) / d_t^* \end{array} \right\} \tag{3.86}$$

and $(\alpha\beta)$ in the subscript indicates the α, βth element in the corresponding matrix. Similarly to the zeroth-order reduction, terms that are not functions of 2D generalized strain $\mathcal{E}$ are dropped as they do not affect the energy when deformed. From equation (3.79) it can be found that the form of the asymptotically correct 2D energy expression does not resemble any existing plate model.

3.3.2 Transformation to Reissner-Mindlin Model

Though equation (3.79) is asymptotically correct to the second order, it is inconvenient to put into practical use because it contains derivatives of the 2D generalized strain, making the boundary conditions hard to define. For the convenience in practical use, it would be reasonable to transform it into a model having the same form as the first-order shear deformation theory (FSDT), or Reissner-Mindlin plate theory, since the energy expression is acquired from the first-order approximation.

In order to transform into the Reissner-Mindlin model, two transverse shear strains generated by the rotation of transverse normal need to be introduced along with

another orthogonal triad $\mathbf{B}_i^*$ in the deformed plate to redefine the 2D generalized strains, so that

$$\mathbf{R}_{,\alpha} = \mathbf{B}_\alpha^* + \varepsilon_{\alpha\beta}^* \mathbf{B}_\beta^* + 2\gamma_{\alpha 3}\mathbf{B}_3^* \tag{3.87}$$

$$\mathbf{B}_{i,\alpha}^* = (-K_{\alpha\beta}^* \mathbf{B}_\beta^* \times \mathbf{B}_3^* + K_{\alpha 3}^* \mathbf{B}_3^*) \times \mathbf{B}_i^* \tag{3.88}$$

with the transverse shear strains as

$$\gamma = [\ 2\gamma_{13} \quad 2\gamma_{23}\ ]^{\mathrm{T}} \tag{3.89}$$

Kinematic identity can be found between the former 2D generalized strain $\mathcal{E}$ and Reissner-Mindlin 2D generalized strain $\mathcal{R}$ as triad $\mathbf{B}_i$ and $\mathbf{B}_i^*$ can be related with a direction cosine matrix containing γ ([50] and [38]). The relationship can be derived to be

$$\mathcal{E} = \mathcal{R} - \mathcal{D}_\alpha \gamma_{,\alpha} \tag{3.90}$$

where

$$\begin{aligned} \mathcal{D}_1 &= \begin{bmatrix} 0 & 0 & 0 & 1 & 0 & 0 \\ 0 & 0 & 0 & 0 & 1 & 0 \end{bmatrix}^{\mathrm{T}} \\ \mathcal{D}_2 &= \begin{bmatrix} 0 & 0 & 0 & 0 & 1 & 0 \\ 0 & 0 & 0 & 0 & 0 & 1 \end{bmatrix}^{\mathrm{T}} \end{aligned} \tag{3.91}$$

$$\mathcal{R} = [\ \varepsilon_{11}^* \quad 2\varepsilon_{12}^* \quad \varepsilon_{22}^* \quad K_{11}^* \quad K_{12}^* + K_{21}^* \quad K_{22}^*\ ]^{\mathrm{T}} \tag{3.92}$$

Since the transverse shear strains are introduced in the first-order approximation, they should be considered to be an order higher than the in-plane 2D strains, that is $\gamma \sim (h/l)\epsilon$, otherwise they should be taken into consideration during the zeroth-order approximation. Substituting equation (3.90) back into equation (3.79) and neglecting higher-order terms, the second-order asymptotically correct total potential density in terms of Reissner-Mindlin strains can be expressed as

$$\begin{aligned} 2\Pi_1 = {} & \mathcal{R}^{\mathrm{T}} A \mathcal{R} - 2\mathcal{R}^{\mathrm{T}} A \mathcal{D}_1 \gamma_{,1} - 2\mathcal{R}^{\mathrm{T}} A \mathcal{D}_2 \gamma_{,2} \\ & + \mathcal{R}_{,1}^{\mathrm{T}} B \mathcal{R}_{,1} + 2\mathcal{R}_{,1}^{\mathrm{T}} C \mathcal{R}_{,2} + \mathcal{R}_{,2}^{\mathrm{T}} D \mathcal{R}_{,2} - 2\mathcal{R}^{\mathrm{T}} F \end{aligned} \tag{3.93}$$

Compared to the potential energy of the Reissner-Mindlin plate model, which has the form of

$$2\Pi_{\mathcal{R}} = \mathcal{R}^{\mathrm{T}} A \mathcal{R} + \gamma^{\mathrm{T}} G \gamma - 2\mathcal{R}^{\mathrm{T}} F_{\mathcal{R}} - 2\gamma^{\mathrm{T}} F_{\gamma} \tag{3.94}$$

further derivation is still required to completely eliminate terms with partial derivatives of the 2D generalized strains in equation (3.93). This can be achieved by utilizing the equilibrium equations of

$$\begin{aligned} \mathcal{M}_{11,1} + \mathcal{M}_{12,2} - \mathcal{Q}_1 + m_1 = 0 \\ \mathcal{M}_{22,2} + \mathcal{M}_{12,1} - \mathcal{Q}_2 + m_2 = 0 \end{aligned} \tag{3.95}$$

since in the Reissner-Mindlin model, it has

$$\left\{ \begin{array}{c} \mathcal{N} \\ \mathcal{M} \end{array} \right\} = A\mathcal{R} - F_{\mathcal{R}} \tag{3.96}$$

$$\mathcal{Q} = G\gamma - F_{\gamma} \tag{3.97}$$

Then the following equation can be obtain

$$G\gamma - F_{\gamma} = \mathcal{D}_{\alpha}^{\mathrm{T}} A \mathcal{R}_{,\alpha} - \mathcal{D}_{\alpha}^{\mathrm{T}} F_{\mathcal{R},\alpha} + \left\{ \begin{array}{c} m_1 \\ m_2 \end{array} \right\} \tag{3.98}$$

From equation (3.98), it can be derived that

$$\gamma = G^{-1} F_{\gamma} + G^{-1} \mathcal{D}_{\alpha}^{\mathrm{T}} A \mathcal{R}_{,\alpha} - G^{-1} \mathcal{D}_{\alpha}^{\mathrm{T}} F_{\mathcal{R},\alpha} + G^{-1} \left\{ \begin{array}{c} m_1 \\ m_2 \end{array} \right\} \tag{3.99}$$

Substituting equation (3.99) back into equation (3.93) and dropping higher-order terms as well as terms not related with 2D generalized strains, equation (3.93) can be rewritten as

$$2\Pi_1 = \mathcal{R}^{\mathrm{T}} A \mathcal{R} + \gamma^{\mathrm{T}} G \gamma - 2\mathcal{R}^{\mathrm{T}} F - 2\gamma^{\mathrm{T}} F_{\gamma} + U^* \tag{3.100}$$

where

$$F_{\gamma} = -\mathcal{D}_{\alpha}^{\mathrm{T}} S_{\epsilon\kappa,\alpha} \tag{3.101}$$

$$U^* = \mathcal{R}_{,1}^{\mathrm{T}} \bar{B} \mathcal{R}_{,1} + 2\mathcal{R}_{,1}^{\mathrm{T}} \bar{C} \mathcal{R}_{,2} + \mathcal{R}_{,2}^{\mathrm{T}} \bar{D} \mathcal{R}_{,2} \tag{3.102}$$

and

$$\begin{aligned}\bar{B} &= B + A\mathcal{D}_1 G^{-1} {\mathcal{D}_1}^{\mathrm{T}} A \\ \bar{C} &= C + A\mathcal{D}_1 G^{-1} {\mathcal{D}_2}^{\mathrm{T}} A \\ \bar{D} &= D + A\mathcal{D}_2 G^{-1} {\mathcal{D}_2}^{\mathrm{T}} A\end{aligned} \tag{3.103}$$

In the most ideal case, U^* can be driven to be zero for any $\mathcal{R}$ and transverse shear stiffness matrix can be solved exactly and then the asymptotically correct total potential in equation (3.100) will have the same form as the Reissner-Mindlin model in equation (3.94). However, this is impossible for most multi-layered, smart composite plate, so an optimization process is required to minimize U^* and thus minimize the error between the asymptotically correct expression and the Reissner-Mindlin form expression in practical use. The accuracy of the Reissner-Mindlin like model is influenced by the deviation of U^* from zero. Considering symmetry, there are totally 78 quantities in $\bar{B}$, $\bar{C}$ and $\bar{D}$ that are desirable to be zero, and there are 27 optimization parameters, 3 in G and 24 in L_α. To make U^* as close to zero as possible under any strain field, an overdetermined linear system with 78 equations and 27 unknowns is constructed, then the least square method is implemented to solve for the 27 unknowns with a minimized error.

By the optimization process, the best transverse shear stiffness matrix G can be obtained to complete the transformation to the Reissner-Mindlin like plate model. Similar to the zeroth-order model, the current first-order model can be directly applied in any thermopiezoelastic Reissner-Mindlin plate analyses with equivalent stiffness matrices A, G, F and F_γ calculated from plate geometry and material constants. Piezoelectricity, thermal expansion and pyroelectricity are coupled in the stiffness matrices along with elasticity.

3.3.3 Recovery Relations

Up to this stage, the first-order plate model has been acquired, with which 2D solution of a thermopiezoelastic multi-layered plate can be obtained. The 2D solution,

however, only represent the behavior of the reference surface and in many applications it would be more important to comprehend the 3D fields in the plate structure. The ability to accurately calculate the 3D displacement, stress, strain and electric fields is the essential standard to evaluate the fidelity of a dimensionally reduced model. As a result, the recovery relations are necessities in the formulation of the present work.

The goal of recovery is to express the 3D fields in terms of 2D generalized strains and thickness coordinate x_3. From equation (2.5), the 3D displacement field U_i can be easily recovered using 2D displacement field u_i and warping functions w_i, that is

$$U_i = u_i + x_3(\mathcal{C}_{3i} - \delta_{3i}) + w_j\mathcal{C}_{ji} \tag{3.104}$$

where warping functions w_i need to be expanded to the corresponding order. For the first-order approximation with energy expanded to the second-order, the 3D strain field can be recovered to be

$$\begin{aligned} \Gamma_e^1 &= \epsilon + x_3\kappa \\ 2\Gamma_s^1 &= {v_\parallel}' + e_\alpha w_{3,\alpha}^0 \\ \Gamma_t^1 &= w_3^{0\prime} + {v_3}' \end{aligned} \tag{3.105}$$

Then the 3D stresses up to the first-order can be obtained using equation (2.31). The first-order approximation allows the theory to predict the transverse shear strains and stresses, but even though the accuracy of transverse normal strain can be increased by v_3 that introducing terms related to prescribed temperature change, the Euler-Lagrange equation in (3.61) still make the transverse normal stress to be vanished regardless of deformation and temperature change. For composite laminated plates, it is necessary to acquire the transverse normal stress related to deformation, which is important for delamination prediction.

Currently the strains are in first-order and the energy is in second-order. For predicting transverse normal stress as well as more accurate values of other 3D fields, the warping functions should be perturbed once more to the order of $(h^3/l^2)\epsilon$, that is

$$\begin{aligned} w_\parallel &= w_\parallel^0 + v_\parallel^1 + y_\parallel + o\left(\frac{h^3}{l^2}\epsilon\right) \\ w_3 &= w_3^0 + v_3^1 + y_3 + o\left(\frac{h^3}{l^2}\epsilon\right) \\ \phi &= \phi^0 + \varphi^1 + \psi + o\left(\frac{h^3}{l^2}\epsilon\right) \end{aligned} \tag{3.106}$$

Using a similar procedure as the first-order reduction, the expression of the warping functions and electric potential can be obtained. Since the process is repeating and the expression of energy is lengthy, the results of warping functions and electric potential are directly presented as

$$\begin{aligned} {y_\parallel}' = & -C_s^{-1}e_s e_\alpha \varphi^1_{,\alpha} - C_s^{-1} I_\alpha^{\mathrm{T}} e^*_{et}\varphi^1_{,\alpha} \\ & + \left(\frac{x_3}{h}+\frac{1}{2}\right) I_\alpha^{\mathrm{T}} e^*_{et}\varphi^{1+}_{,\alpha} - \left(\frac{x_3}{h}-\frac{1}{2}\right) I_\alpha^{\mathrm{T}} e^*_{et}\varphi^{1-}_{,\alpha} \end{aligned} \tag{3.107}$$

$$\begin{aligned} {y_3}' = & -\frac{C_{et}^{**\mathrm{T}}}{C_t}\left[I_\beta(\bar{D}_\alpha + L_\alpha)\mathcal{E}_{,\alpha\beta} + I_\beta \bar{g}_{,\beta}\right] + \frac{e_t}{d_t^* C_t}\left(E_{\phi\alpha\beta}\mathcal{E}_{,\alpha\beta} + S_\phi + \hat{\hat{\mathcal{P}}}\right) \\ & + \frac{d_t}{d_t^* C_t}\left[E_{\perp\alpha\beta}\mathcal{E}_{,\alpha\beta} + S_\perp + \left(\frac{x_3}{h}+\frac{1}{2}\right)\tau_3 + \left(\frac{x_3}{h}-\frac{1}{2}\right)\beta_3\right. \\ & - \left(\frac{x_3}{h}+\frac{1}{2}\right) E^+_{\perp\alpha\beta}\mathcal{E}_{,\alpha\beta} + \left(\frac{x_3}{h}-\frac{1}{2}\right) E^-_{\perp\alpha\beta}\mathcal{E}_{,\alpha\beta} \\ & \left. - \left(\frac{x_3}{h}+\frac{1}{2}\right) S^+_\perp + \left(\frac{x_3}{h}-\frac{1}{2}\right) S^-_\perp\right] \end{aligned} \tag{3.108}$$

$$\begin{aligned} \psi' = & \frac{e_{et}^{*\mathrm{T}}}{d_t^*}\left[I_\beta(\bar{D}_\alpha + L_\alpha)\mathcal{E}_{,\alpha\beta} + I_\beta \bar{g}_{,\beta}\right] - \frac{1}{d_t^*}\left(E_{\phi\alpha\beta}\mathcal{E}_{,\alpha\beta} + S_\phi + \hat{\hat{\mathcal{P}}}\right) \\ & + \frac{e_t}{d_t^* C_t}\left[E_{\perp\alpha\beta}\mathcal{E}_{,\alpha\beta} + S_\perp + \left(\frac{x_3}{h}+\frac{1}{2}\right)\tau_3 + \left(\frac{x_3}{h}-\frac{1}{2}\right)\beta_3\right. \\ & - \left(\frac{x_3}{h}+\frac{1}{2}\right) E^+_{\perp\alpha\beta}\mathcal{E}_{,\alpha\beta} + \left(\frac{x_3}{h}-\frac{1}{2}\right) E^-_{\perp\alpha\beta}\mathcal{E}_{,\alpha\beta} \\ & \left. - \left(\frac{x_3}{h}+\frac{1}{2}\right) S^+_\perp + \left(\frac{x_3}{h}-\frac{1}{2}\right) S^-_\perp\right] \end{aligned} \tag{3.109}$$

with

$${E_{\perp\alpha\beta}}' = -\left(e_\beta^{\mathrm{T}} D_\alpha^* + C_{s(\alpha\beta)} C_\perp + e_{s(\alpha\beta)} C_\phi\right) \tag{3.110}$$

$$S_\perp{}' = -\left(e_\beta^{\mathrm{T}} g_{,\beta}^* + C_{s(\alpha\beta)} w_{3e,\alpha\beta}^0 + e_{s(\alpha\beta)} \phi_{e,\alpha\beta}^0 + P_3\right) \tag{3.111}$$

$$E_{\phi\alpha\beta}{}' = -\left(e_\beta^{\mathrm{T}} e_s C_s^{-1} D_\alpha^* + e_{s(\alpha\beta)} C_\perp - d_{s(\alpha\beta)} C_\phi\right) \tag{3.112}$$

$$S_\phi{}' = -\left(e_\beta^{\mathrm{T}} e_s C_s^{-1} g_{,\beta}^* + e_{s(\alpha\beta)} w_{3e,\alpha\beta}^0 - d_{s(\alpha\beta)} \phi_{e,\alpha\beta}^0\right) \tag{3.113}$$

and $\hat{\hat{\mathcal{P}}}$ is an arbitrary function of x_α.

Even though it is possible to derive the energy expression to the forth-order with warping functions and electric potential presented above, it is unnecessary to do so because the resultant expression will contain second-order derivatives of 2D generalized strain and thus too complicated for practical use. Consequently, the Reissner-Mindlin like plate model derived from first-order reduction is still adopted for 2D plate analysis, while the stress recovery considers the strains in second-order, so that the 3D strains should be expressed as

$$\begin{aligned} \Gamma_e^2 &= \varepsilon + x_3 \kappa + I_\alpha v_{\|,\alpha}^1 \\ 2\Gamma_s^2 &= v_\|^{1\prime} + y_\|{}' + e_\alpha (w_{3,\alpha}^0 + v_{3,\alpha}^1) \\ \Gamma_t^2 &= w_3^{0\prime} + v_3^{1\prime} + y_3{}' \end{aligned} \tag{3.114}$$

and the electric field to be

$$\begin{aligned} E_s^2 &= -\phi_{,\|}^0 - \varphi_{,\|}^1 \\ E_t^2 &= -\phi^{0\prime} - \varphi^{1\prime} - \psi' \end{aligned} \tag{3.115}$$

3D stress field and electric displacement can be recovered using equation (2.31). Now, the complete 3D fields can be predicted using the presented theory.

4. Numerical Examples

In this chapter, several numerical examples are provided to validate the present theory. Both the results from zeroth-order reduction and first-order reduction are analyzed. Examples include a very thin plate with different shapes used to validate the zeroth-order approximation and a thicker plate with different boundary conditions used for validating the first-order approximation. Results of the present theory are computed using symbolic manipulation software and shell finite element analyses with stiffness matrices directly specified with results from the last chapter. Recovered 3D displacement, stress, strain and electric potential are compared with 3D finite element results from commercial code ABAQUS. Results of the present work show good agreements with the 3D finite element analyses.

4.1 Validation of the Zeroth-Order Model

The zeroth-order model has the form of CLPT, in which transverse shear deformation is not considered. For an extremely thin plate such as a space reflector mentioned in chapter 1, transverse shear deformation is small enough to be completely neglected, making the zeroth-order model capable of providing high-fidelity results, so it is unnecessary to go to the first-order approximation.

In this section, two-layered plates with the aspect ratio of approximately 1000, which is close to the aspect ratio of a flexible space reflector, are considered and the layup of the plates is shown in Figure 4.1, with a layer of PVDF piezoelectric material and a layer of polyimide. The PVDF layer has a thickness of 0.05 mm and the polyimide layer is 0.1 mm. Two layers are perfectly bonded and electrodes are coated on the top and bottom interfaces of the PVDF layer.

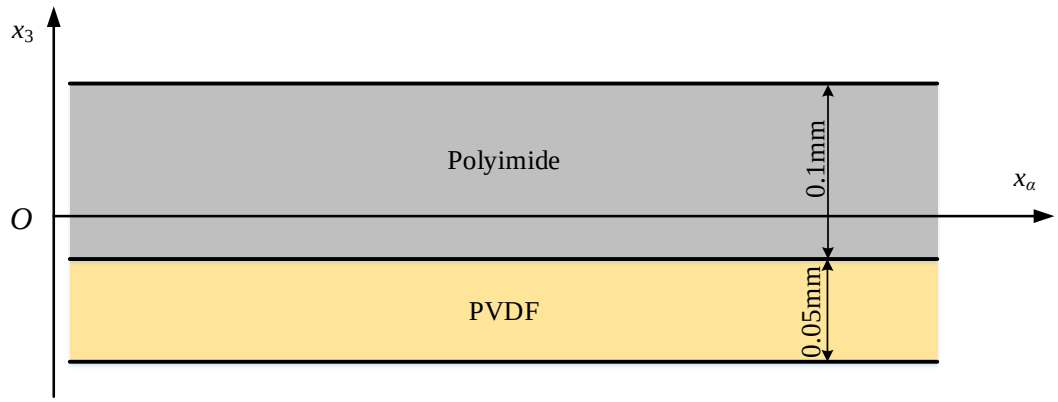

Figure 4.1. Layup of the two-layered plate.

Material properties of PVDF and polyimide are shown in Table 4.1, with the properties of PVDF coming from [51]. PVDF, as well as most piezoelectric materials, is orthotropic after polarization and polyimide is an isotropic material.

4.1.1 Example 1: Two-Layered Simply-Supported Rectangular Plate

In this example, the two-layered plate has a rectangular shape with simply-supported boundary condition as shown in Figure 4.2. Dimensions of the plate is set to be $a = b = 140$ mm. For a simply-supported rectangular plate, an analytical Navier solution can be found. 2D displacements u_1, u_2 and u_3 are expressed in double trigonometric series and 2D generalized strains can be calculated using plate kinematics, enabling the recovery of 3D displacement, stress and strain field. 3D finite element analyses use ABAQUS with 3D piezoelectric continuum quadratic element C3D20RE. All the elements have an in-plane dimension of 0.7 mm $\times$0.7 mm and thickness of the plate is divided into 6 elements, 4 in the polyimide layer and 2 in the PVDF layer. Total number of 3D elements is 240000. Firstly, the case that

Table 4.1. Material Properties of PVDF and Polyimide

Properties	PVDF	Polyimide
C_{11} (GPa)	3.61	3.85
C_{12} (GPa)	1.61	1.98
C_{13} (GPa)	1.42	1.98
C_{22} (GPa)	3.13	3.85
C_{23} (GPa)	1.31	1.98
C_{33} (GPa)	1.63	3.85
C_{44} (GPa)	0.55	0.93
C_{55} (GPa)	0.59	0.93
C_{66} (GPa)	0.69	0.93
e_{31} (C/m^2)	0.0105	0
e_{32} (C/m^2)	-0.0117	0
e_{33} (C/m^2)	-0.0284	0
e_{24} (C/m^2)	-0.0122	0
e_{15} (C/m^2)	-0.0123	0
d_{11} ($\times 10^{-9}$ C^2/(Nm^2))	0.0651	0.031
d_{22} ($\times 10^{-9}$ C^2/(Nm^2))	0.0821	0.031
d_{33} ($\times 10^{-9}$ C^2/(Nm^2))	0.0686	0.031
α_1 ($\times 10^{-6}$ K^{-1})	130	20
α_2 ($\times 10^{-6}$ K^{-1})	130	20
α_3 ($\times 10^{-6}$ K^{-1})	130	20
p_1 ($\times 10^{-6}$ C/(Km^2))	30	0
p_2 ($\times 10^{-6}$ C/(Km^2))	30	0
p_3 ($\times 10^{-6}$ C/(Km^2))	30	0

only electric potential is applied is studied. Then the case of combined load, with temperature change also applied, is analyzed.

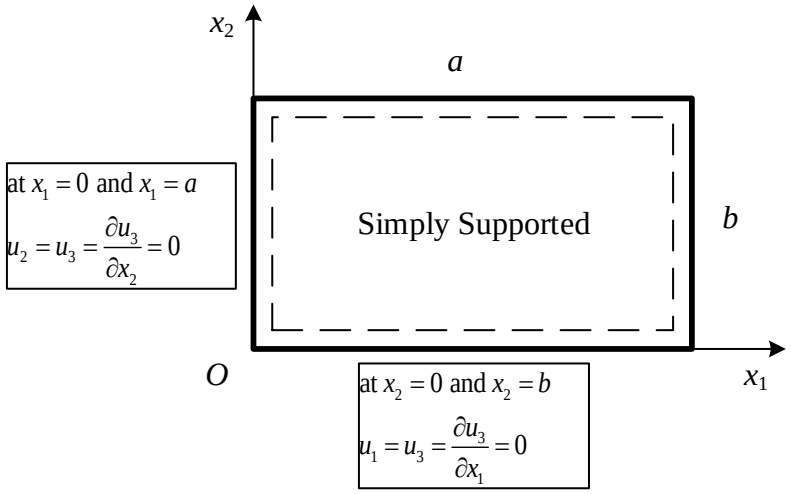

Figure 4.2. Geometry and boundary condition of a rectangular plate.

In the case when only electric potential is applied, a 300 V constant voltage charge is applied on the bottom of the plate, $x_3 = -0.075$ mm, and the interface between the PVDF and polyimide, $x_3 = -0.025$ mm, is grounded. Deflection in x_3 of the mid-surface along $x_2 = 0.07$ m is shown in Figure 4.3. After obtaining the deflection of the reference surface, 3D fields can be recovered. For result comparison, stresses, strains and electric potential distribution at the center of the plate ($x_1 = x_2 = 0.07$ m) is shown in Figures 4.4 to 4.9, with the coordinate in thickness direction normalized as $\bar{x}_3 = x_3/h$. Because of the layup and material properties, in-plane shear stress and strain are zero at the center. From Figures 4.3 to 4.9, it can be seen that the results from present work show a great accuracy. Though not shown here, the present model is capable of predicting the electric field and electric displacement using equation (3.37).

In the case of combined load, in addition to the 300 V voltage on the bottom surface, a uniform temperature change of 5 K is applied on the whole plate. From equation (3.26) and (3.30) it can be derived that when the temperature change is constant in the thickness direction, terms related to the pyroelectric coefficient are cancelled in the energy expression (3.28), resulting the pyroelectric effect to be trivial.

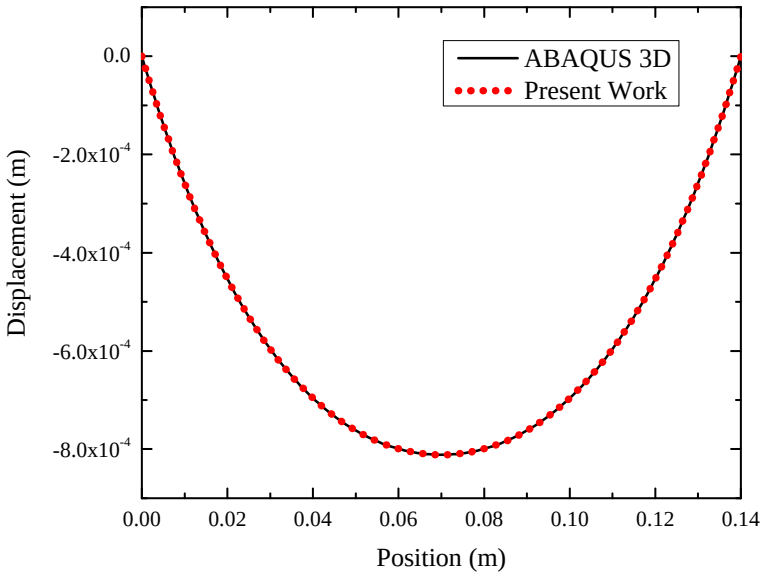

Figure 4.3. Deflection u_3 of the plate along $x_2 = 0.07$ m with electric load.

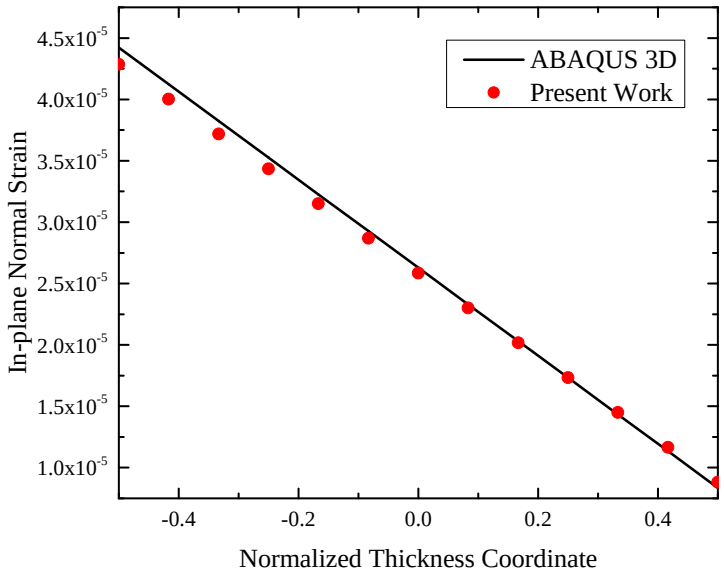

Figure 4.4. Distribution of strain Γ_{11} through thickness at the center with electric load.

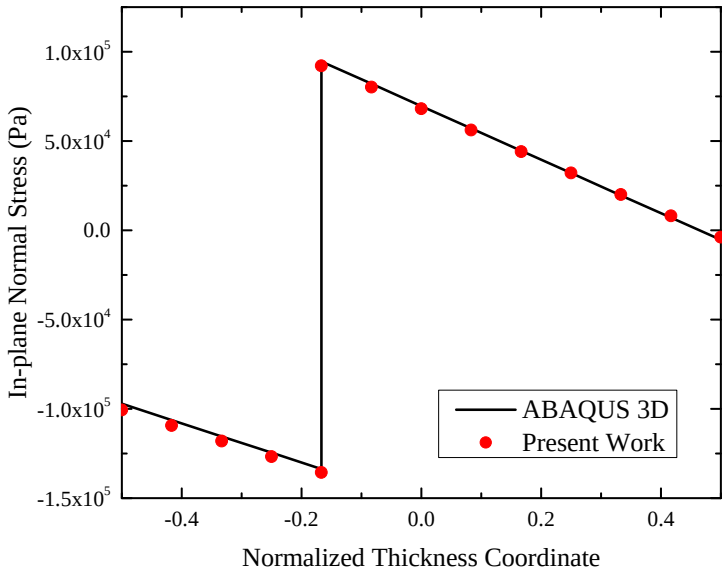

Figure 4.5. Distribution of stress σ_{11} through thickness at the center with electric load.

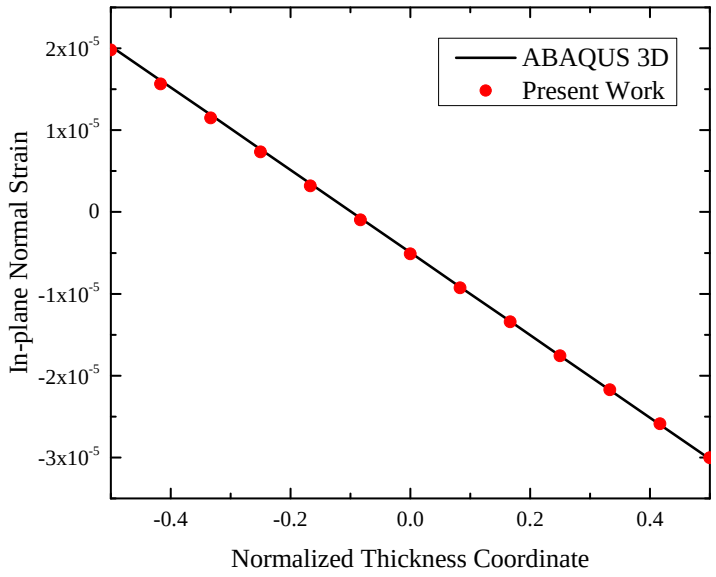

Figure 4.6. Distribution of strain Γ_{22} through thickness at the center with electric load.

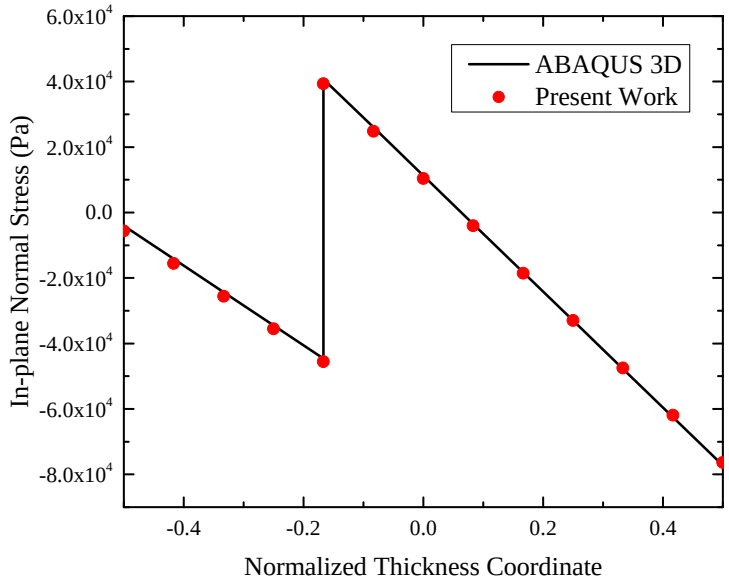

Figure 4.7. Distribution of stress σ_{22} through thickness at the center with electric load.

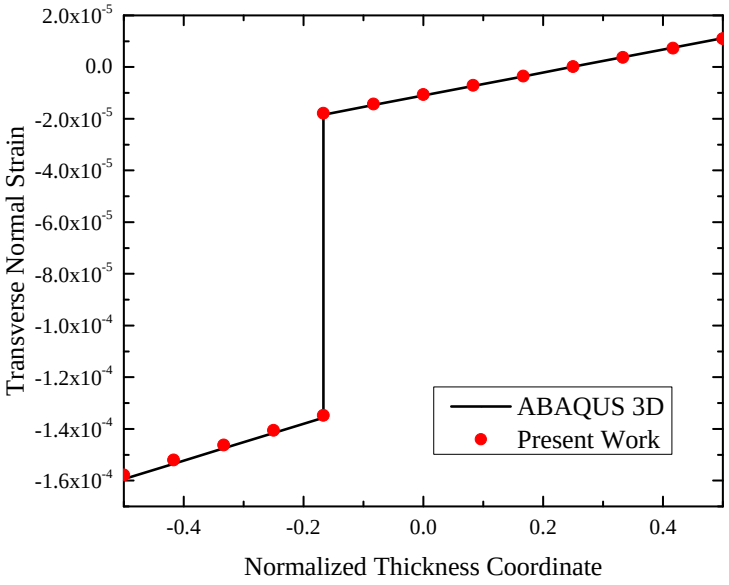

Figure 4.8. Distribution of strain Γ_{33} through thickness at the center with electric load.

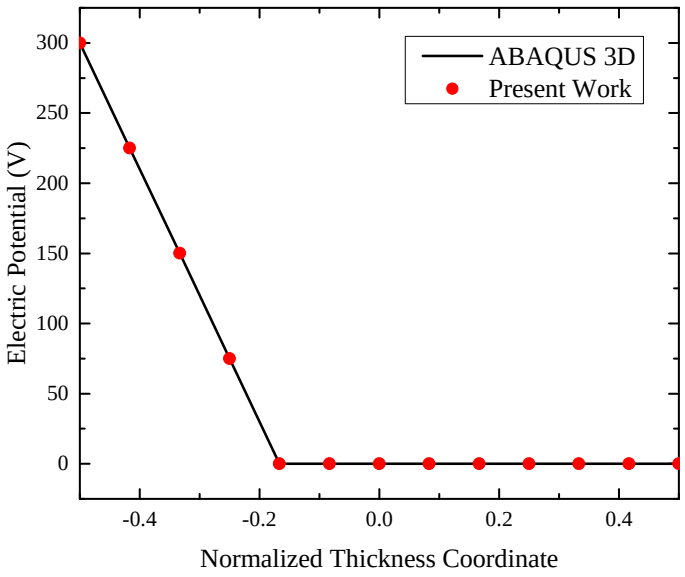

Figure 4.9. Distribution of electric potential ϕ through thickness at the center with electric load.

Results of deflection in x_3, in-plane stresses and strains and electric potential are shown in Figures 4.10 to 4.16, with data picked up from the same position as the last case. It can be observed that the present work is able to provide excellent prediction under both electric and thermal loads.

In CLPT, transverse normal strain is enforced to be zero because of the Kirchhoff hypothesis, but this can be shown to be incorrect by Figures 4.8 and 4.15. In the zeroth-order approximation, transverse normal strain is piecewise linearly distributed through the thickness. Even though in the polyimide layer, which is an isotropic material, transverse normal strain is an order smaller than in the PVDF layer, it has a similar magnitude as the in-plane strain, and because of the piezoelectric effect in the PVDF layer, the transverse normal strain is even greater. Consequently, the Kirchhoff hypothesis, which neglects transverse normal strain, will inevitably induce the loss of accuracy. Transverse normal stress and transverse shear stresses and strains are not predictable because they are small terms in the zeroth-order approximation.

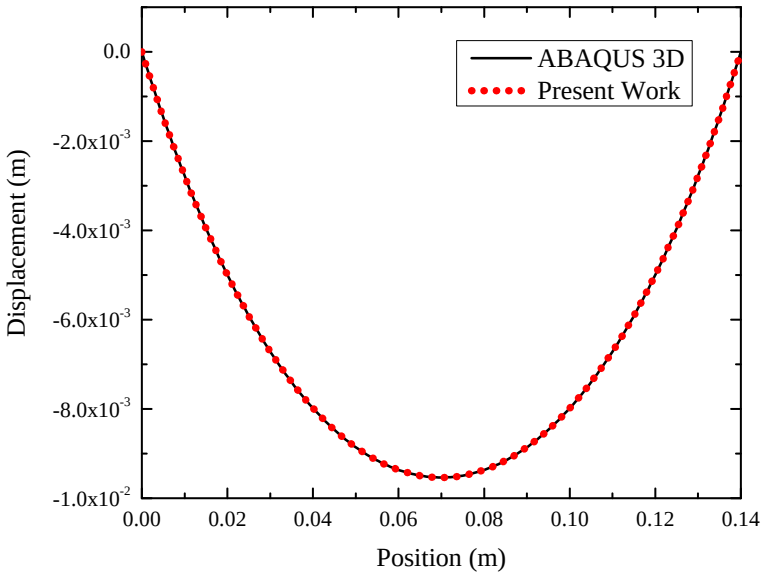

Figure 4.10. Deflection u_3 of the plate along $x_2 = 0.07$ m with combined load.

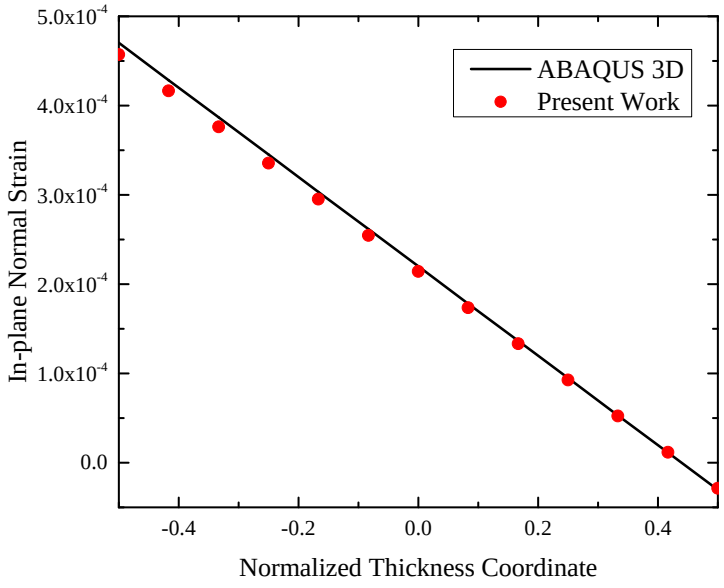

Figure 4.11. Distribution of strain Γ_{11} through thickness at the center with combined load.

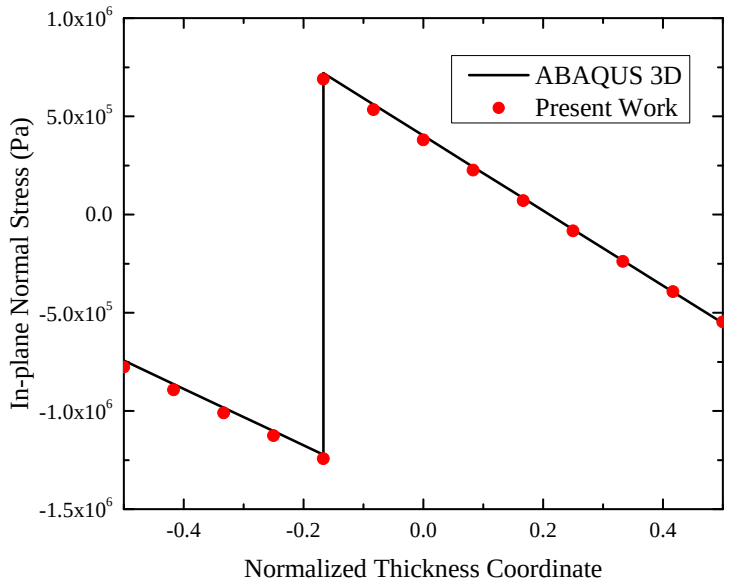

Figure 4.12. Distribution of stress σ_{11} through thickness at the center with combined load.

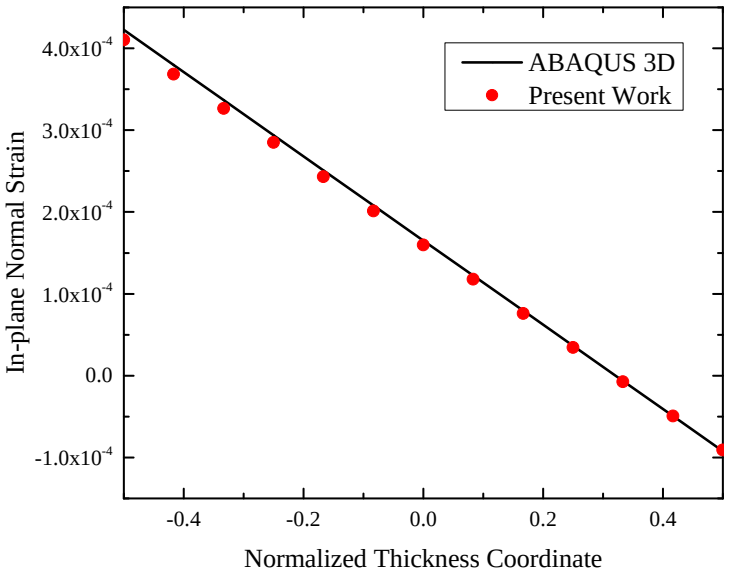

Figure 4.13. Distribution of strain Γ_{22} through thickness at the center with combined load.

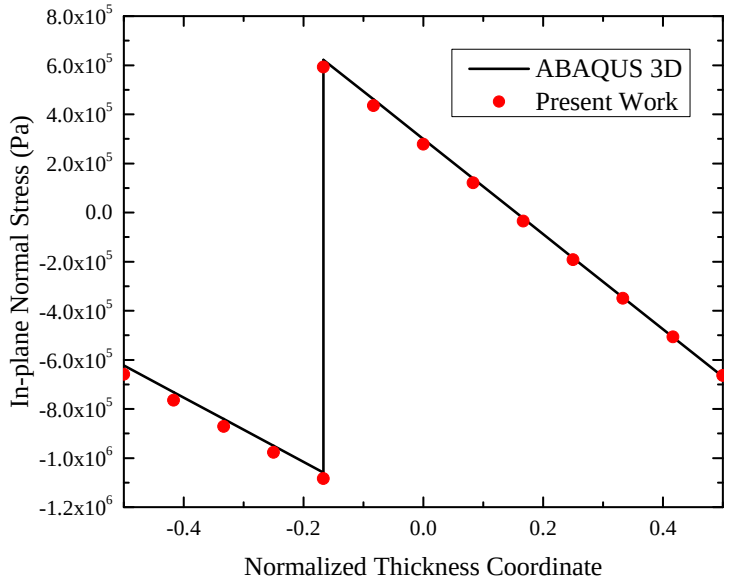

Figure 4.14. Distribution of stress σ_{22} through thickness at the center with combined load.

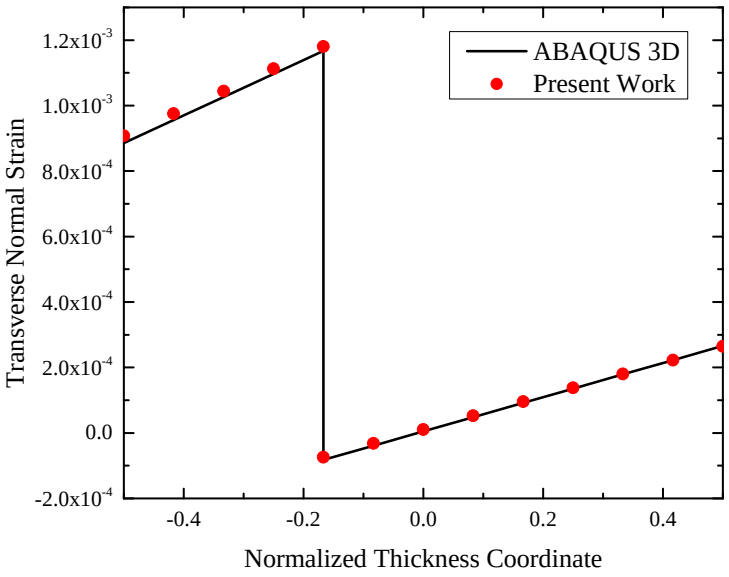

Figure 4.15. Distribution of strain Γ_{33} through thickness at the center with combined load.

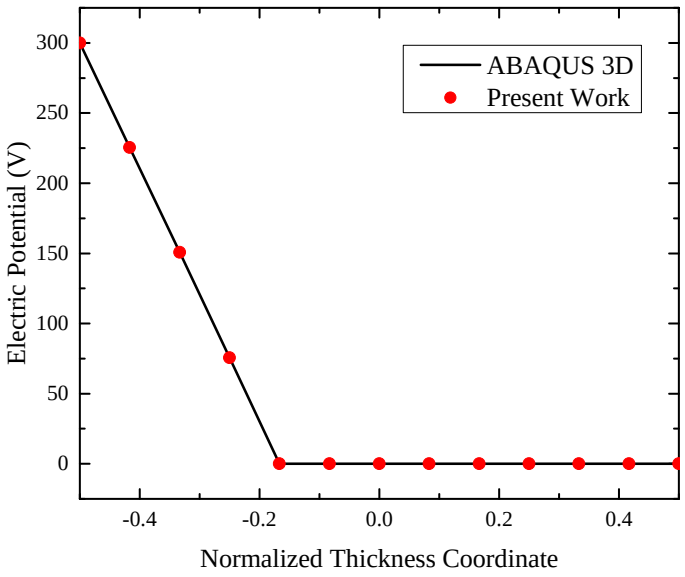

Figure 4.16. Distribution of electric potential ϕ through thickness at the center with combined load.

4.1.2 Example 2: Two-Layered Simply-Supported Circular Plate

In this example, the plate has the same layup and thickness as the one in example 1, while the shape is circular and the simply-supported boundary condition is defined in a cylindrical coordinate system, as shown in Figure 4.17. Radius of the plate is $R = 80$ mm. Analytical solution for an anisotropic circular plate is difficult to find, so shell finite element analyses using ABAQUS is applied. Though the solution is found by commercial codes, the section properties are defined using the present theory, that is, the stiffness matrices of the shell elements are directly specified by the value calculated with equation (3.29) and (3.30) instead of specifying 3D material properties given in Table 4.1. The 2D plate is meshed into 37836 S8R5 quadratic thin shell elements. The output database can provide the deflection and 3D fields can be recovered using the computed 2D generalized strains. The 3D model used for comparison has 228900 C3D20RE elements, with 6 elements through the thickness.

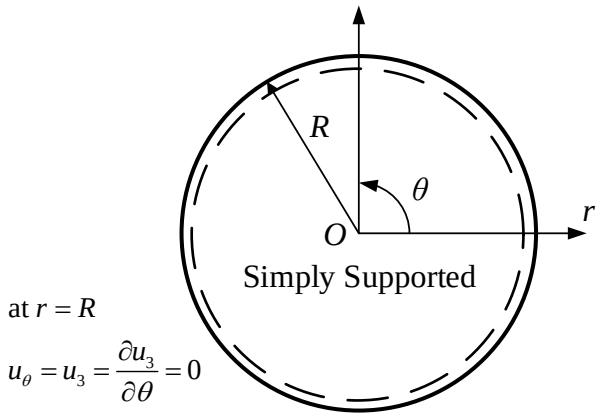

Figure 4.17. Geometry and boundary condition of a circular plate.

Similar to example 1, plate loaded with electric potential only is analyzed first then loaded with both electric potential and temperature change. Electric potential of 300V is applied on the bottom surface and the interface between the layers is grounded. Temperature change is set to be 5K in the case of combined load. Deflection u_3 of the mid-surface is plotted from $\theta = \pi$ to $\theta = 0$, and 3D stresses, strains and electric potential are picked from the center, $r = 0$, through the thickness. Deflection, 3D stresses and strains and electric potential of electrically loaded only are shown in Figures 4.18 to 4.24, and results from the combined load case are in Figures 4.25 to 4.31.

From Figures 4.18 to 4.31, an excellent agreement can be observed between the present model and 3D finite element model. Deflection of the center point of both rectangular and circular plate under two kinds of loads is shown in Table 4.2, with only the error of pure electrically loaded circular plate being larger than 0.01%.

Based on the results presented in this section, it can be proved that the plate model from the zeroth-order approximation can provide a reliable prediction of 3D variables including in-plane stresses, strains, electric field and displacement of a relatively thin thermopiezoelastic plate deformed by electric and thermal loads. Compared with

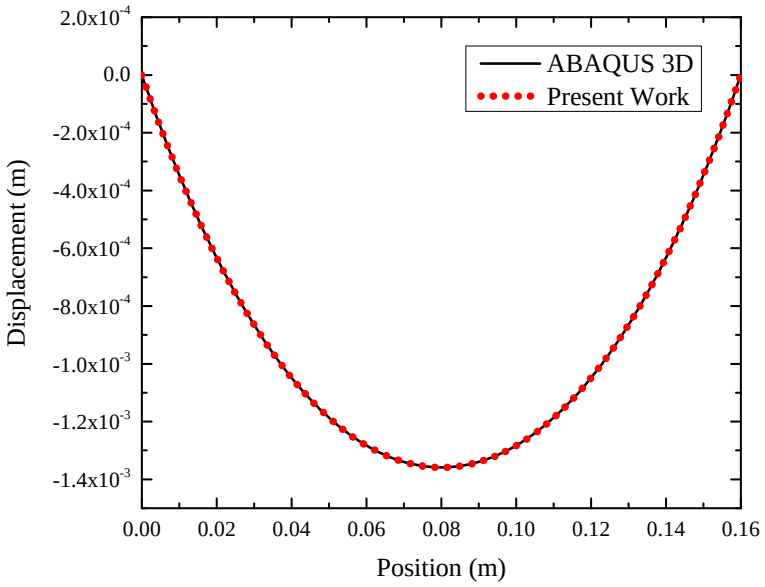

Figure 4.18. Deflection u_3 of the plate along $\theta = \pi$ to $\theta = 0$ with electric load.

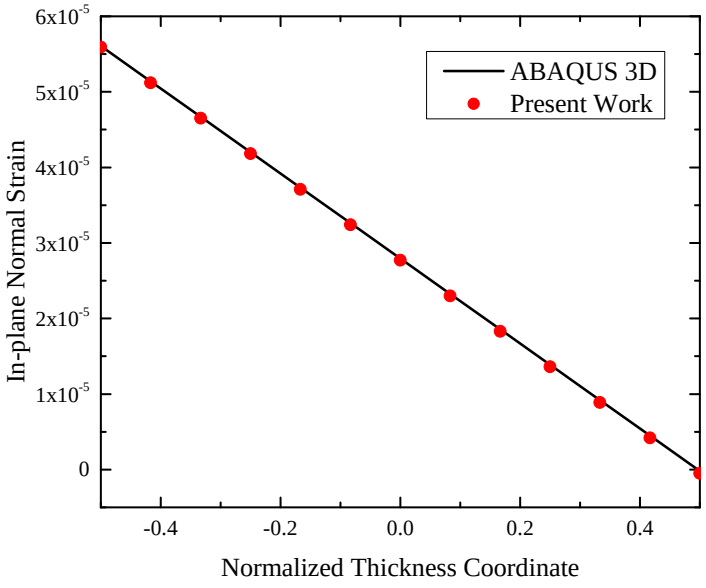

Figure 4.19. Distribution of strain Γ_{11} through thickness at the center with electric load.

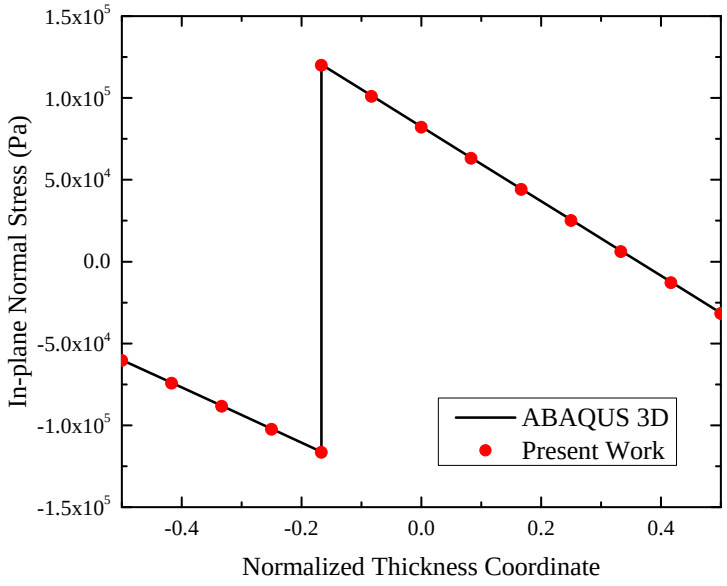

Figure 4.20. Distribution of stress σ_{11} through thickness at the center with electric load.

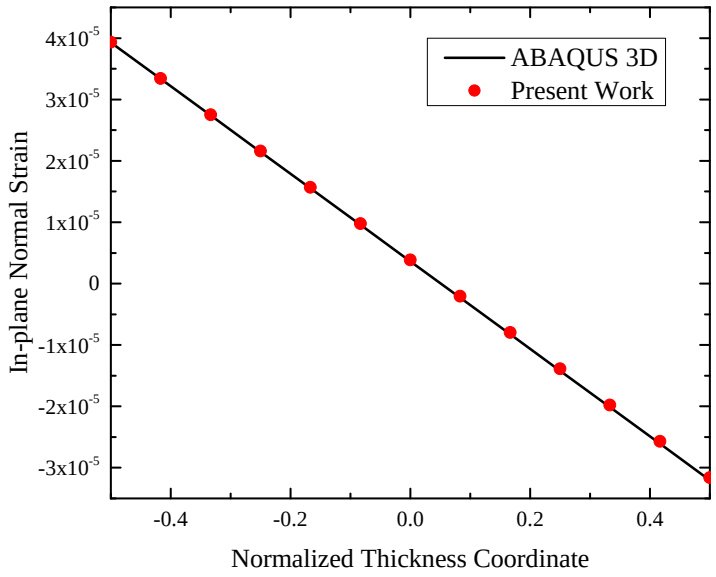

Figure 4.21. Distribution of strain Γ_{22} through thickness at the center with electric load.

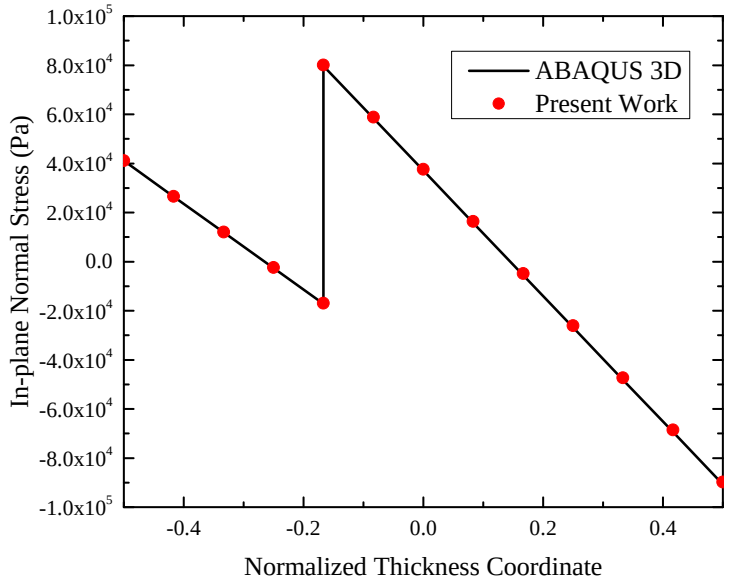

Figure 4.22. Distribution of stress σ_{22} through thickness at the center with electric load.

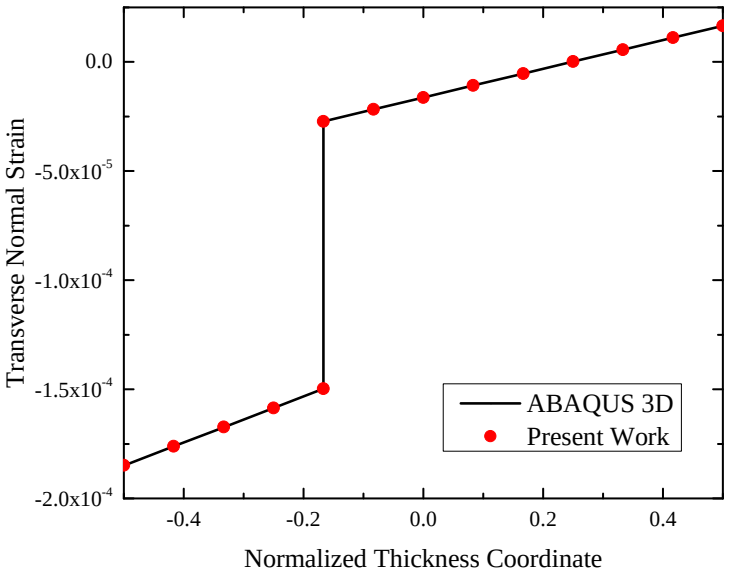

Figure 4.23. Distribution of strain Γ_{33} through thickness at the center with electric load.

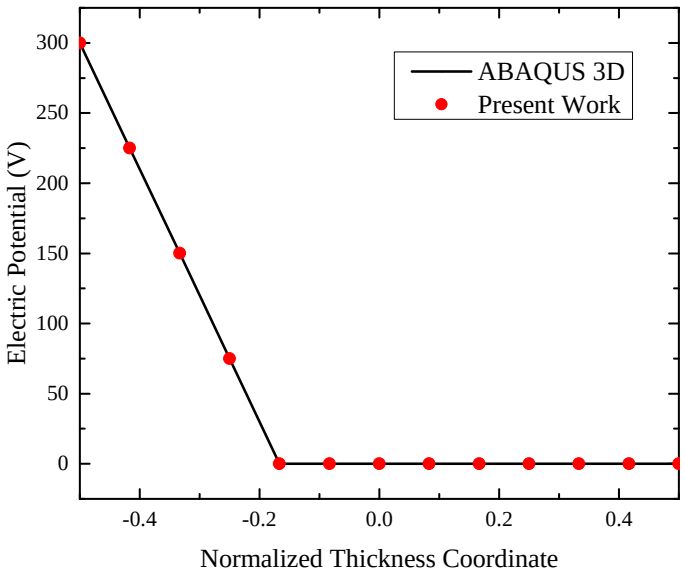

Figure 4.24. Distribution of electric potential ϕ through thickness at the center with electric load.

Table 4.2. Deflection of the center point of the plates (m)

	Rectangular		Circular	
	Electric Load	Combined Load	Electric Load	Combined Load
Present	-8.11475×10^{-4}	-9.53372×10^{-3}	-1.35883×10^{-3}	-1.58843×10^{-2}
3D FE	-8.11477×10^{-4}	-9.53373×10^{-3}	-1.3585×10^{-3}	-1.58843×10^{-2}

solving the same problem using 3D finite element, the present work can greatly improve the computational efficiency as multiple layers are modelled as a single layer. Besides, piezoelectricity and thermal effects are all included in the equivalent stiffness matrices. Again, though the zeroth-order model has the form of CLPT, it has no relation with the Kirchhoff-Love assumptions.

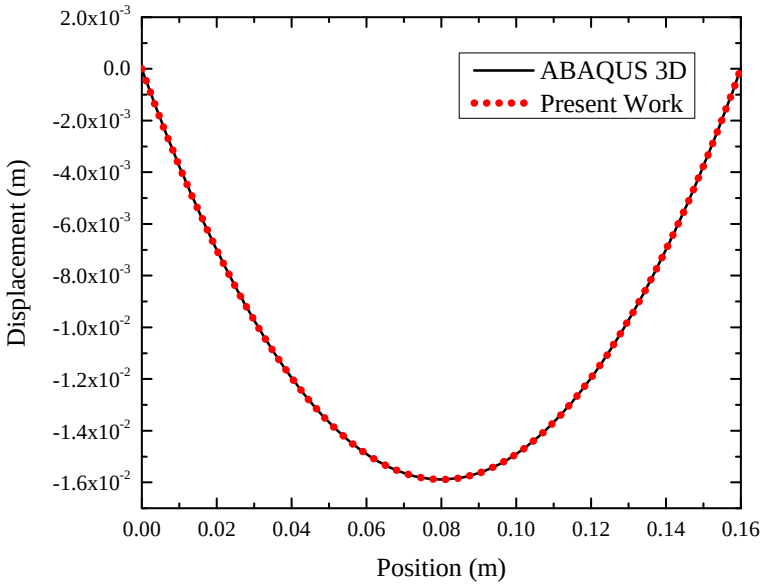

Figure 4.25. Deflection u_3 of the plate along $\theta = \pi$ to $\theta = 0$ with combined load.

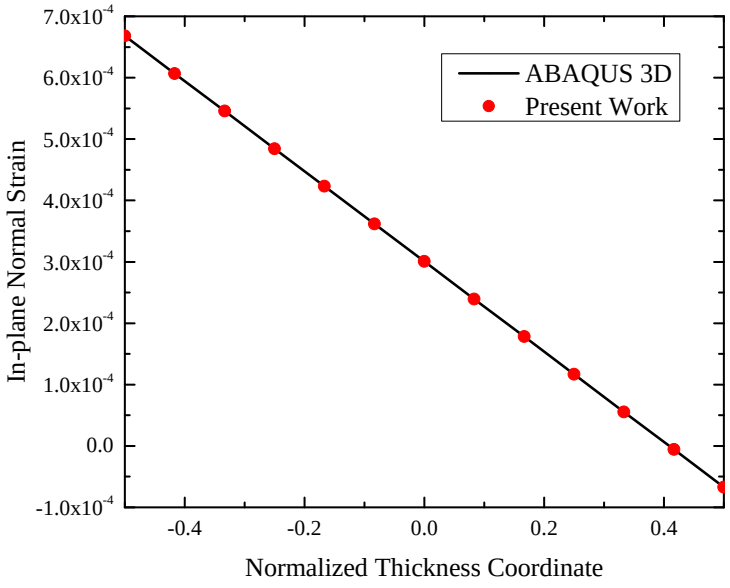

Figure 4.26. Distribution of strain Γ_{11} through thickness at the center with combined load.

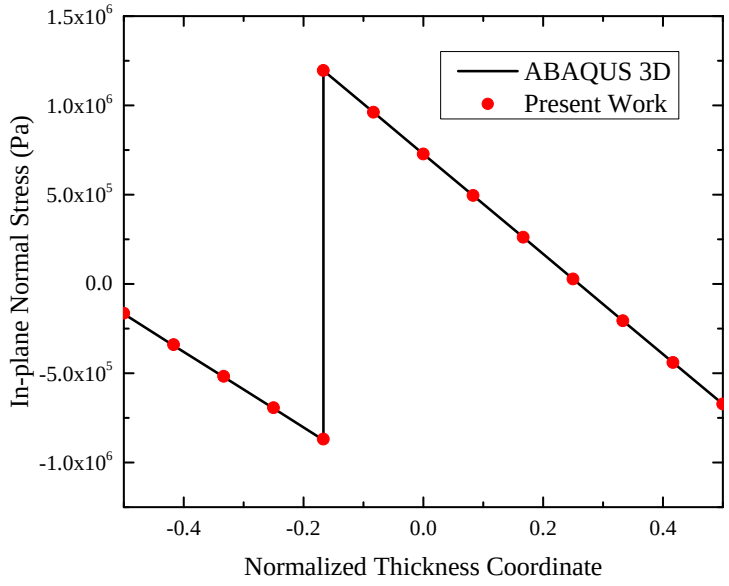

Figure 4.27. Distribution of stress σ_{11} through thickness at the center with combined load.

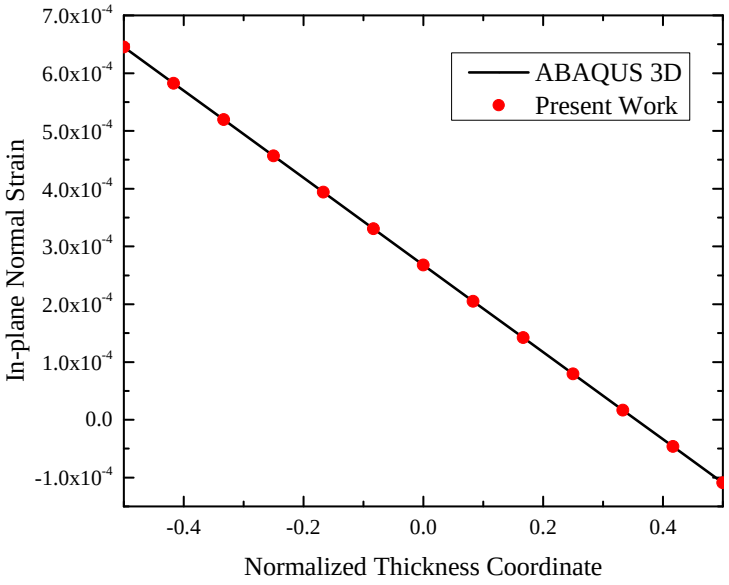

Figure 4.28. Distribution of strain Γ_{22} through thickness at the center with combined load.

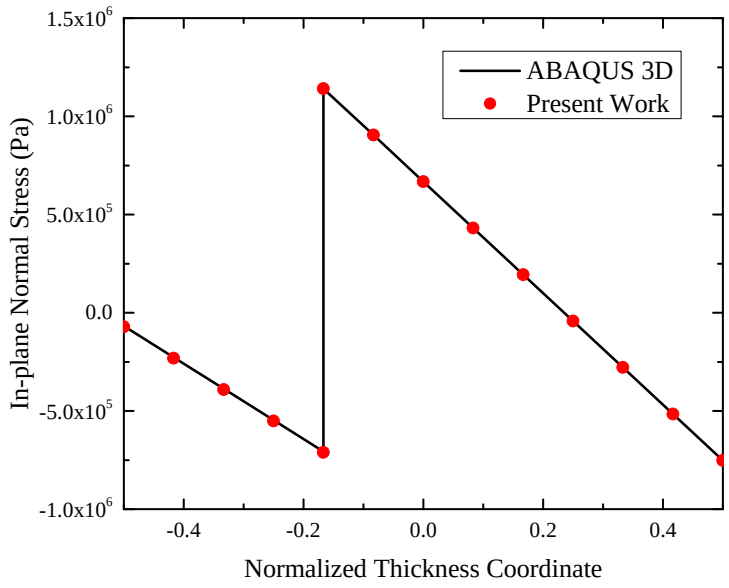

Figure 4.29. Distribution of stress σ_{22} through thickness at the center with combined load.

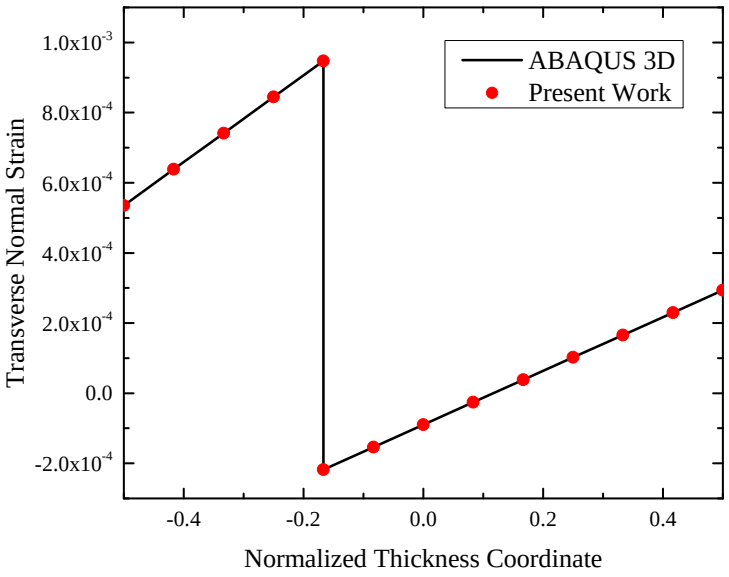

Figure 4.30. Distribution of strain Γ_{33} through thickness at the center with combined load.

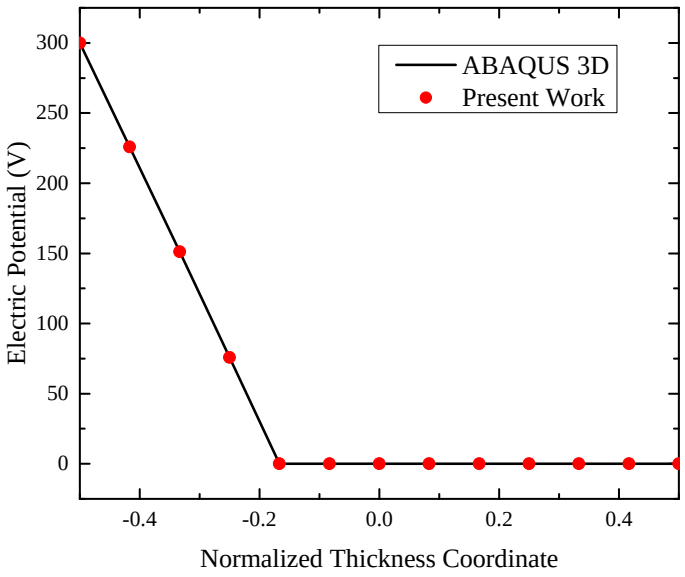

Figure 4.31. Distribution of electric potential ϕ through thickness at the center with combined load.

4.2 Validation of the First-Order Model

In the application of smart plate structures, especially smart plates based on composite laminations, the thickness is not always as thin and the layup is not always as simple as the structure similar to a flexible space reflector discussed in last section. In such cases, transverse shear deformation can be significant and should not be neglected, so the analyses should be based on the first-order model.

In this section, a three-layered rectangular plate with different boundary conditions is analyzed. The plate has a PZT-4 piezoelectric layer at the bottom and two fiber-reinforced composite layer laminated above. The fiber-reinforced material is S glass/epoxy, and the middle layer is oriented 90 degree and the top layer 0 degree with respect to x_1 axis. Thickness of each layer is 5 mm, totally 15 mm, and the in-plane dimension is 140 mm $\times$140 mm, giving an aspect ratio of 9.33. Layup of the plate is

shown in Figure 4.32. All layers are considered perfectly bonded and electrodes are on the top and bottom interfaces of the PZT-4 layer.

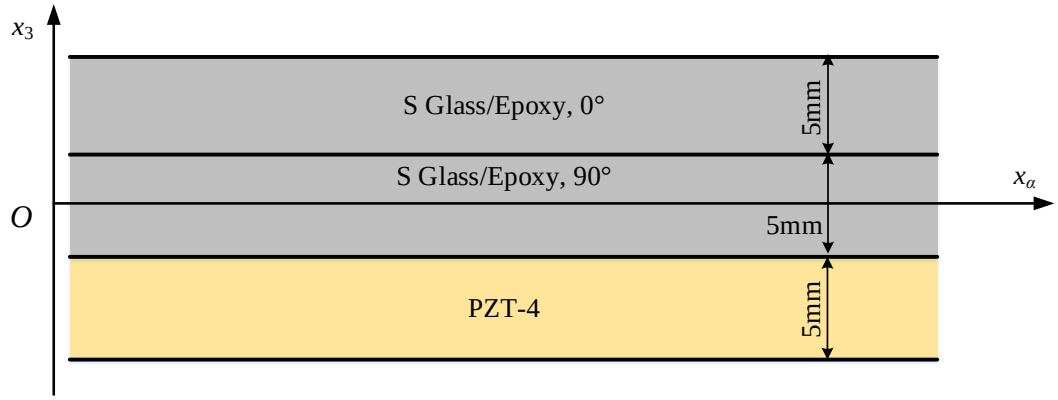

Figure 4.32. Layup of the three-layered plate.

Material properties of PZT-4 and S glass/epoxy are shown in Table 4.3. [52] is referred for the properties of PZT-4. Both PZT-4 and S glass/epoxy are transverse isotropic materials, while the axis of symmetry is in thickness direction for PZT-4 and in-plane direction for S glass/epoxy.

4.2.1 Example 1: Three-Layered Simply-Supported Rectangular Plate

In the first example, the plate is simply-supported as shown in Figure 4.2, with $a = b = 140$ mm. The 2D solution is also based on the Navier solution because of the boundary condition while this Navier solution is based on the first-order shear deformation theory as the expression of first-order approximation is transformed into a Reissner-Mindlin model. For 3D model in ABAQUS, again, element C3D20RE is adopted. The total number of elements is 120000 with 4 elements through the thickness in each layer and the element in-plane dimension of 1.4 mm $\times$1.4 mm. Similar to the zeroth-order reduction validation, two kinds of loadings are tested

Table 4.3. Material Properties of PZT-4 and S glass/epoxy

Properties	PZT-4	S glass/epoxy
C_{11} (GPa)	139.02	48.5
C_{12} (GPa)	77.85	5.82
C_{13} (GPa)	74.33	5.82
C_{22} (GPa)	139.02	12.7
C_{23} (GPa)	74.33	6.7
C_{33} (GPa)	115.45	12.7
C_{44} (GPa)	25.6	3
C_{55} (GPa)	25.6	4.5
C_{66} (GPa)	30.6	4.5
$e_{31} = e_{32}$ (C/m^2)	-5.2	0
e_{33} (C/m^2)	15.08	0
$e_{24} = e_{15}$ (C/m^2)	12.72	0
$d_{11} = d_{22}$ ($\times 10^{-9}$ C^2/(Nm^2))	13.06	0.031
d_{33} ($\times 10^{-9}$ C^2/(Nm^2))	11.51	0.031
$\alpha_1 = \alpha_2$ ($\times 10^{-6}$ K^{-1})	3.8	20
α_3 ($\times 10^{-6}$ K^{-1})	1.2	20
$p_1 = p_2$ ($\times 10^{-6}$ C/(Km^2))	0	0
p_3 ($\times 10^{-6}$ C/(Km^2))	-170	0

on the simply-supported plate: pure electric load of 600 V applied on the bottom surface and combined load with electric field and temperature change of 5 K. Results of deflection, 3D in-plane strains and stresses, transverse normal strain and electric potential are picked at the same location as example 1 in the last section; transverse shear strains and stresses are picked at $x_1 = 0.035$ m, $x_2 = 0.07$ m for "13" direction and $x_1 = 0.07$ m, $x_2 = 0.105$ m for "23" direction.

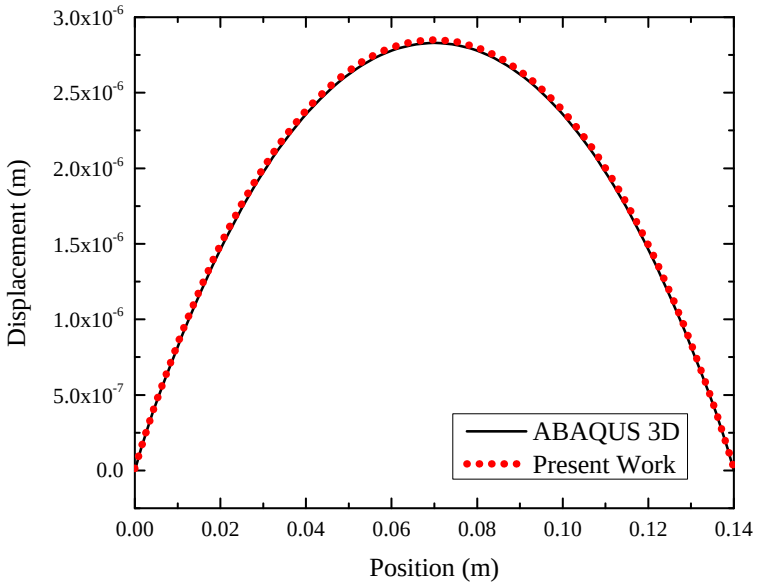

Figure 4.33. Deflection u_3 of the plate along $x_2 = 0.07$ m with electric load.

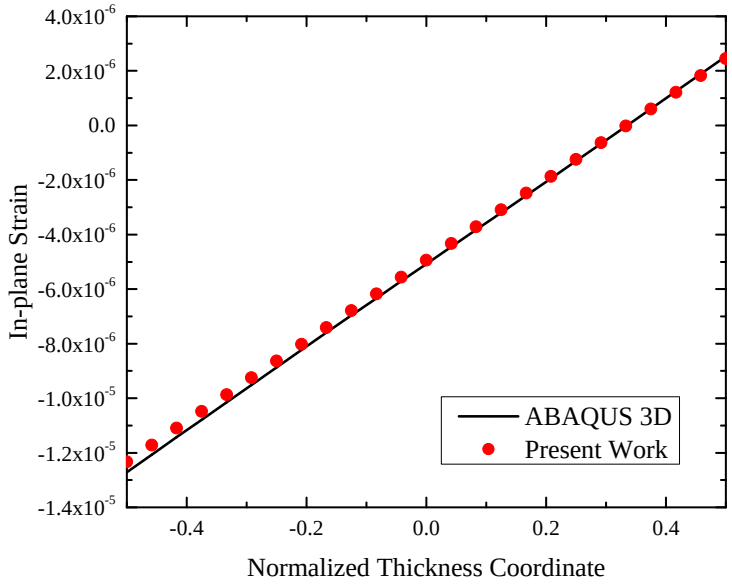

Figure 4.34. Distribution of strain Γ_{11} through thickness at the center with electric load.

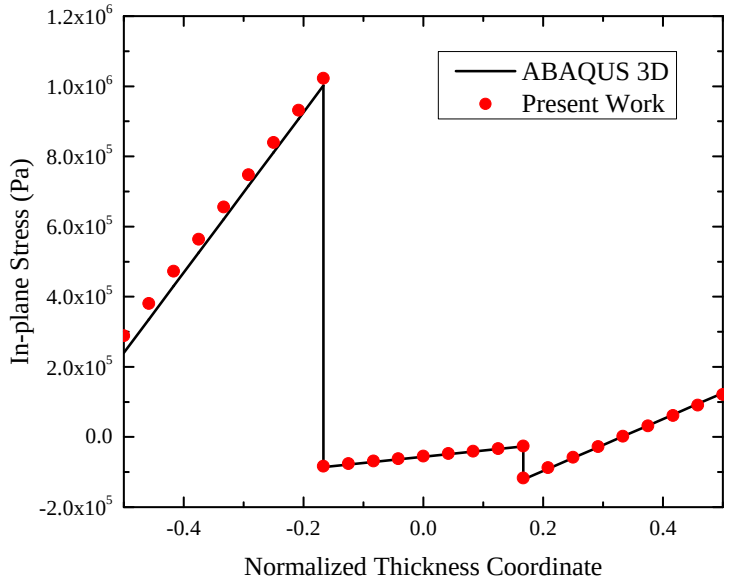

Figure 4.35. Distribution of stress σ_{11} through thickness at the center with electric load.

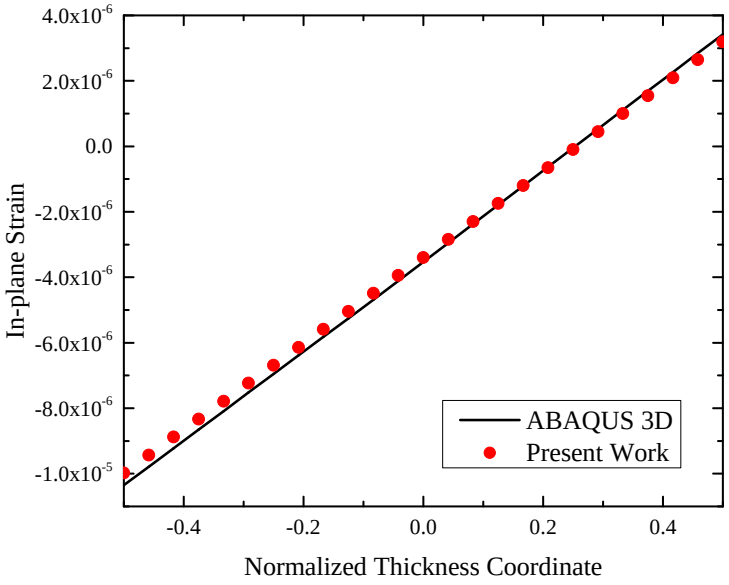

Figure 4.36. Distribution of strain Γ_{22} through thickness at the center with electric load.

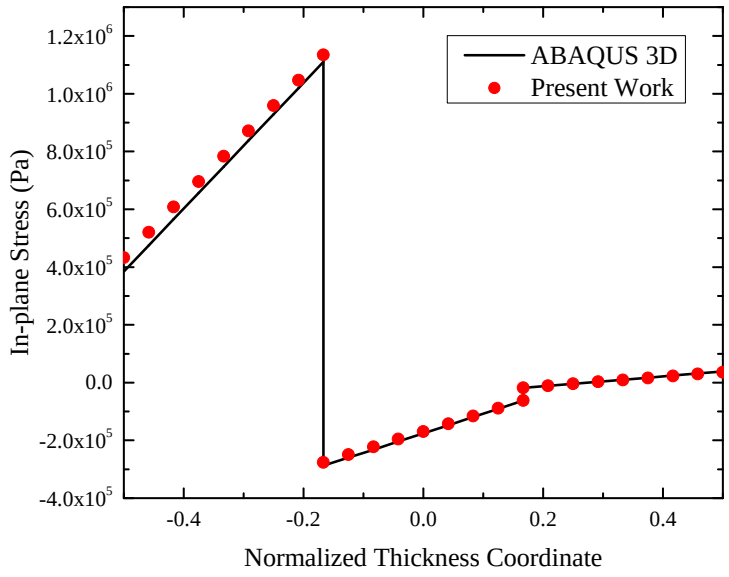

Figure 4.37. Distribution of stress σ_{22} through thickness at the center with electric load.

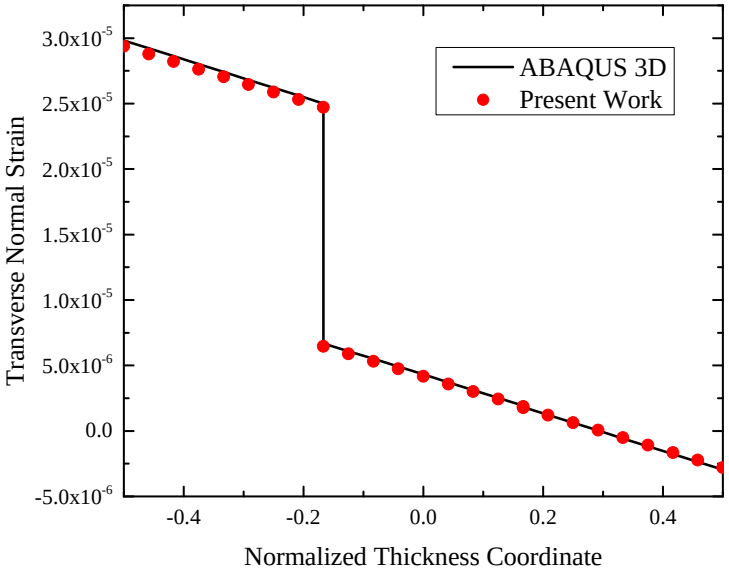

Figure 4.38. Distribution of strain Γ_{33} through thickness at the center with electric load.

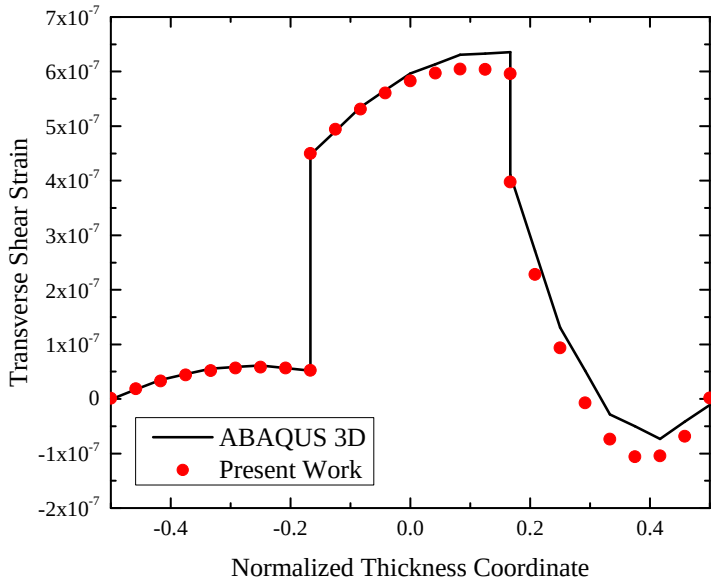

Figure 4.39. Distribution of strain Γ_{13} through thickness at $x_1 = 0.035$ m, $x_2 = 0.07$ m with electric load.

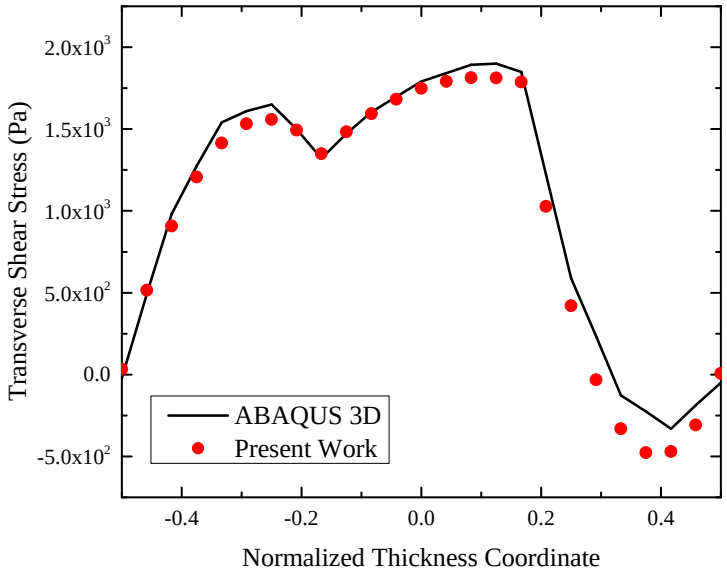

Figure 4.40. Distribution of stress σ_{13} through thickness at $x_1 = 0.035$ m, $x_2 = 0.07$ m with electric load.

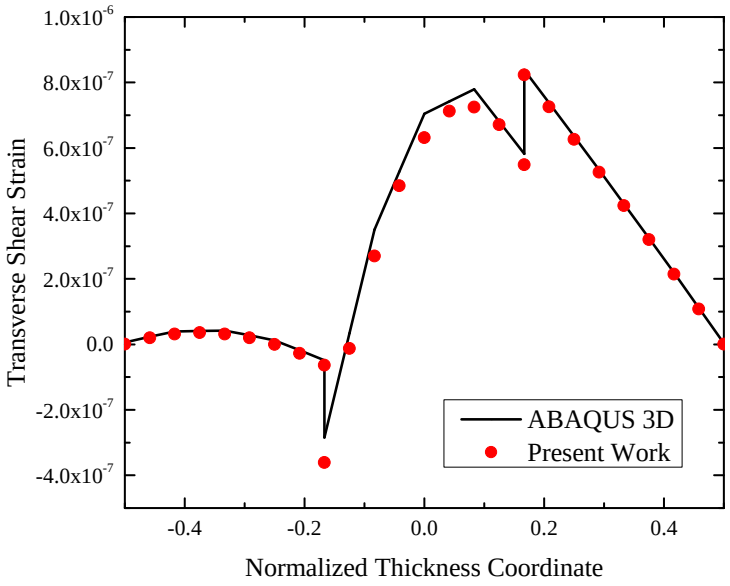

Figure 4.41. Distribution of strain Γ_{23} through thickness at $x_1 = 0.07$ m, $x_2 = 0.105$ m with electric load.

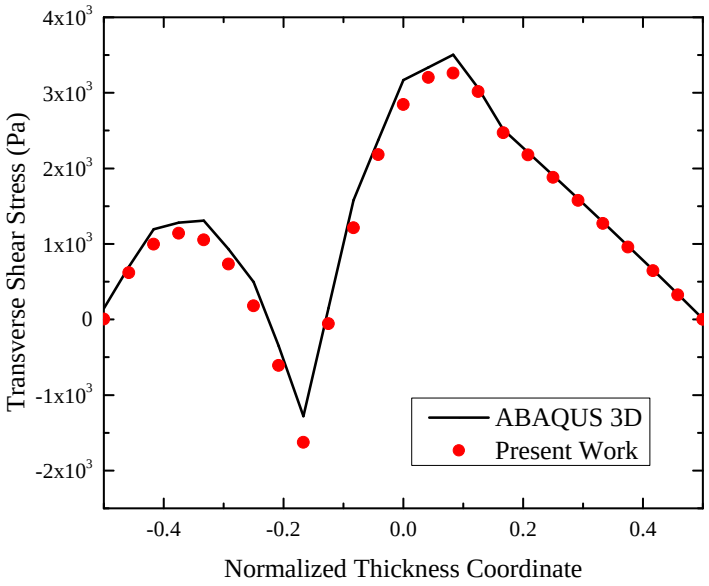

Figure 4.42. Distribution of stress σ_{23} through thickness at $x_1 = 0.07$ m, $x_2 = 0.105$ m with electric load.

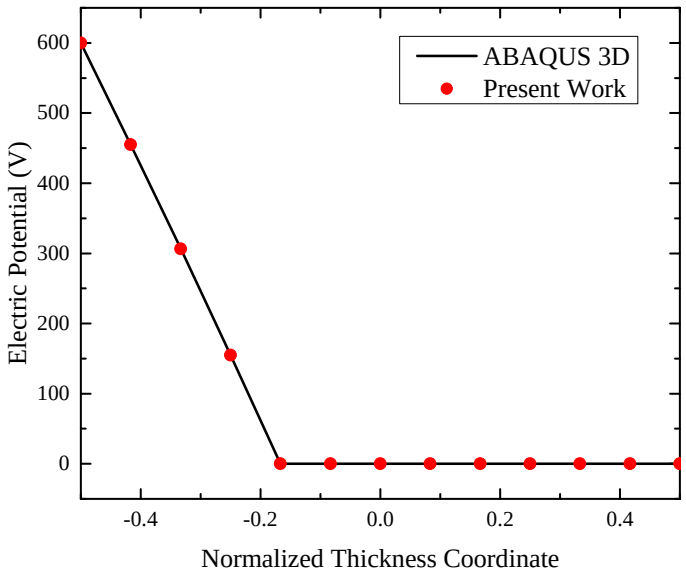

Figure 4.43. Distribution of electric potential ϕ through thickness at the center with electric load.

Results for pure electric load are shown in Figures 4.33 to 4.43, from which it can be found that the first-order approximation model can provide high-fidelity results when the smart plate is thicker and with stronger anisotropy. In addition to in-plane strains and stresses that are predictable in the zeroth-order model, the first-order model also predicts the transverse shear strains and stresses in an acceptable accuracy. Results for combined load are shown in Figures 4.44 to 4.54. Similar accuracy as those in the pure electric load can be observed. Unlike the FSDT which keeps the assumption of straight normals remain straight after deformation in Kirchhoff-Love theory, resulting in the transverse shear strains to be a constant through the thickness, the present model can recover the quadratic distribution as predicted in 3D elastic theory. From Figures 4.39 to 4.42 and 4.50 to 4.53, it is apparent that transverse shear strains and stresses vary greatly through the thickness so a constant value is far from enough for evaluation. Besides, since the present model is derived based on the energy, no correction coefficient is required for matching the energy with 3D theory.

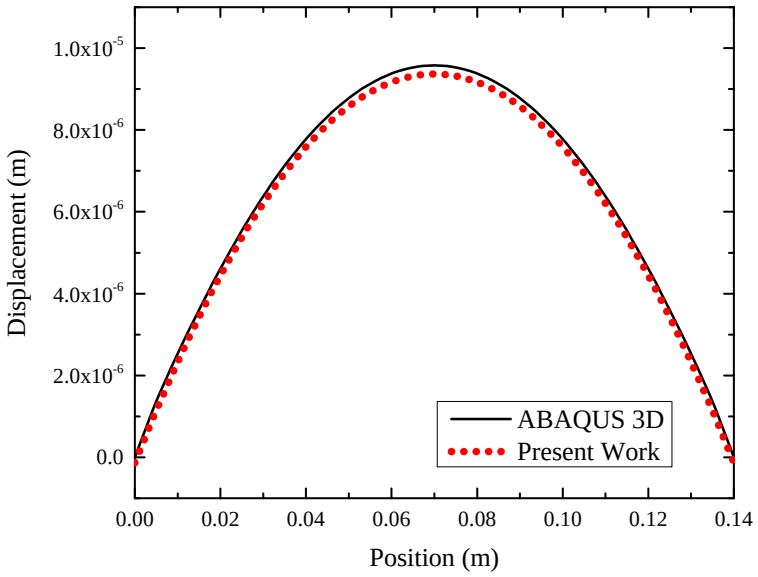

Figure 4.44. Deflection u_3 of the plate along $x_2 = 0.07$ m with combined load.

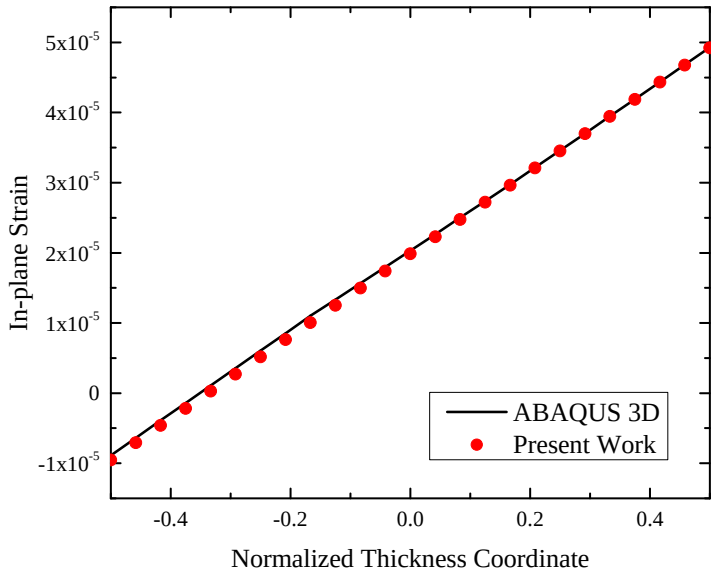

Figure 4.45. Distribution of strain Γ_{11} through thickness at the center with combined load.

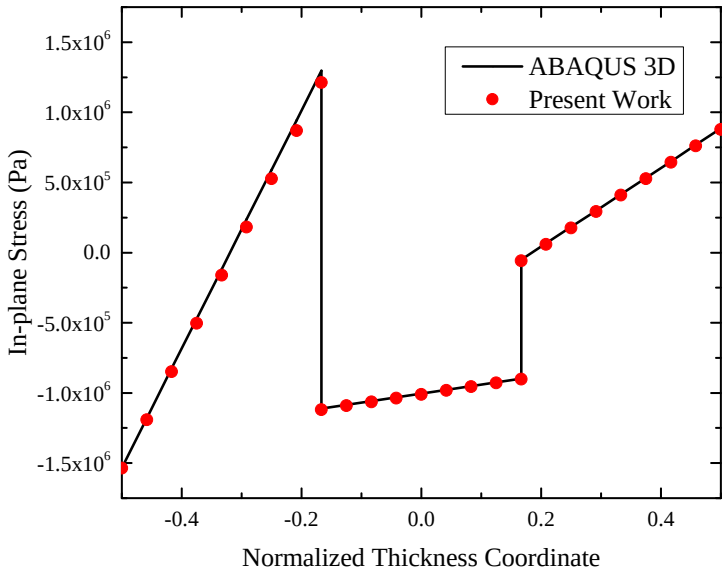

Figure 4.46. Distribution of stress σ_{11} through thickness at the center with combined load.

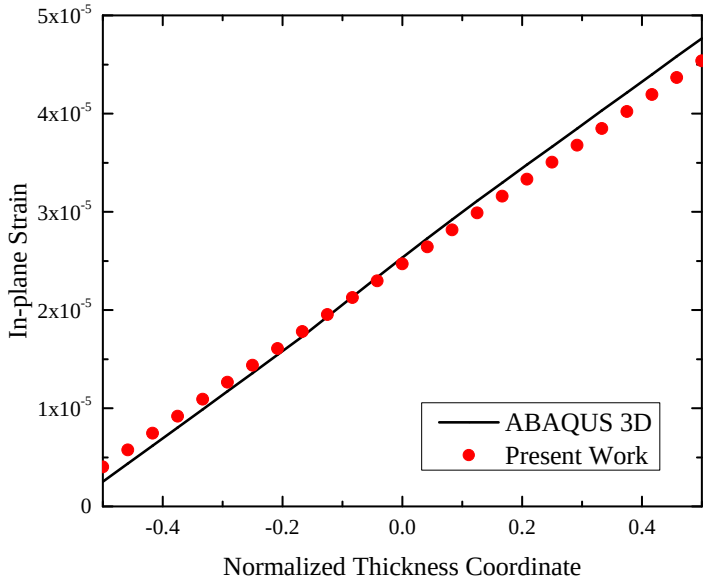

Figure 4.47. Distribution of strain Γ_{22} through thickness at the center with combined load.

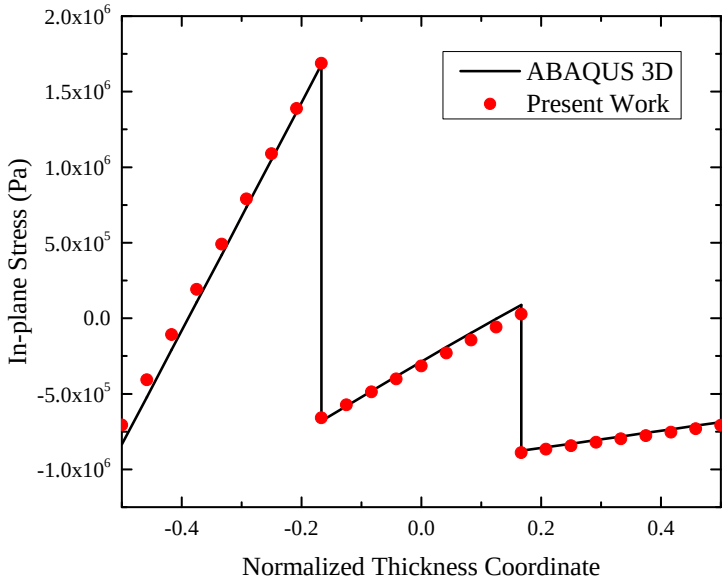

Figure 4.48. Distribution of stress σ_{22} through thickness at the center with combined load.

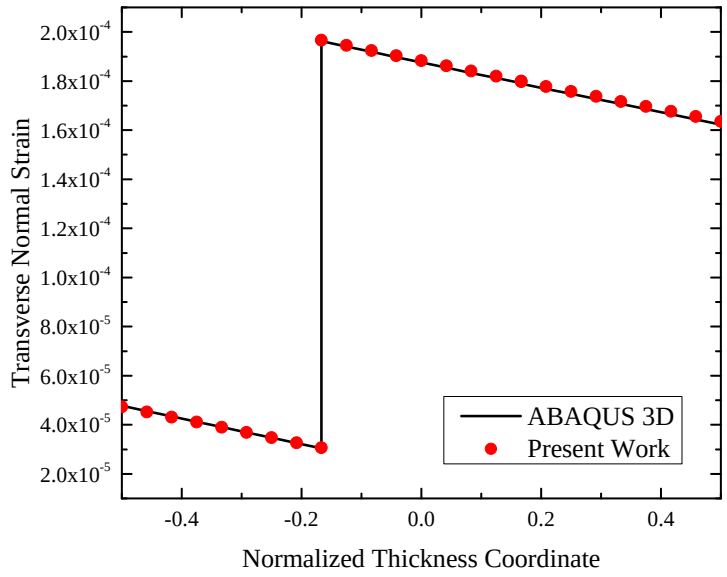

Figure 4.49. Distribution of strain Γ_{33} through thickness at the center with combined load.

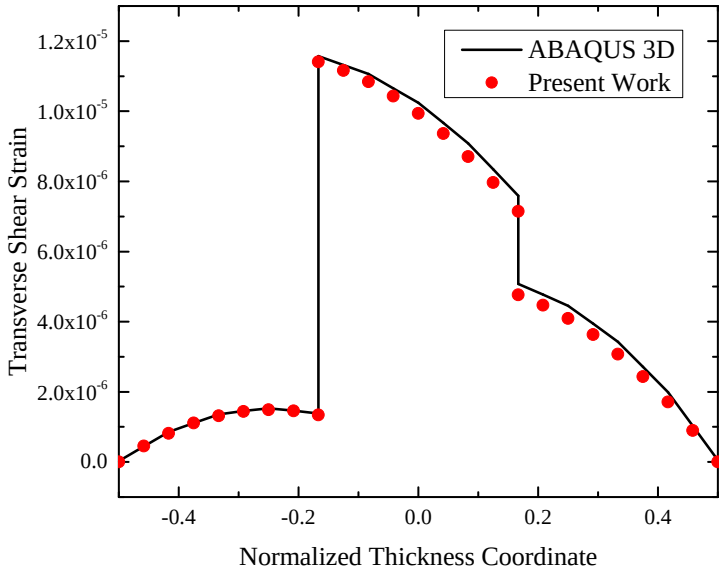

Figure 4.50. Distribution of strain Γ_{13} through thickness at $x_1 = 0.035$ m, $x_2 = 0.07$ m with combined load.

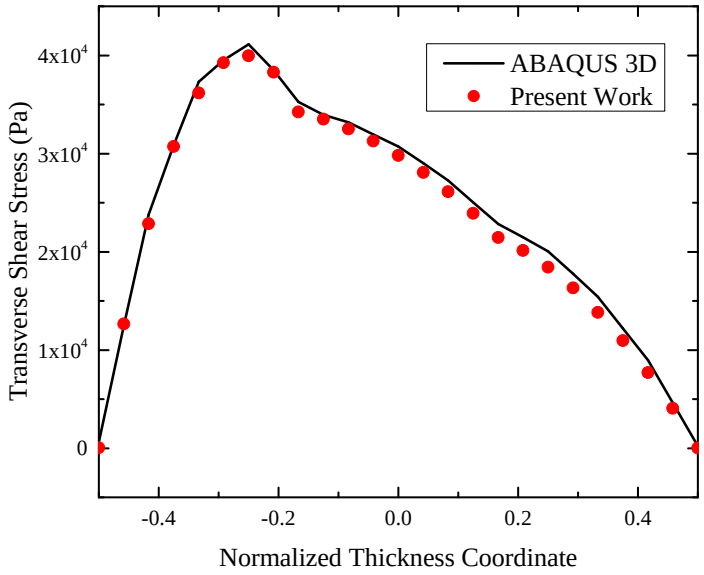

Figure 4.51. Distribution of stress σ_{13} through thickness at $x_1 = 0.035$ m, $x_2 = 0.07$ m with combined load.

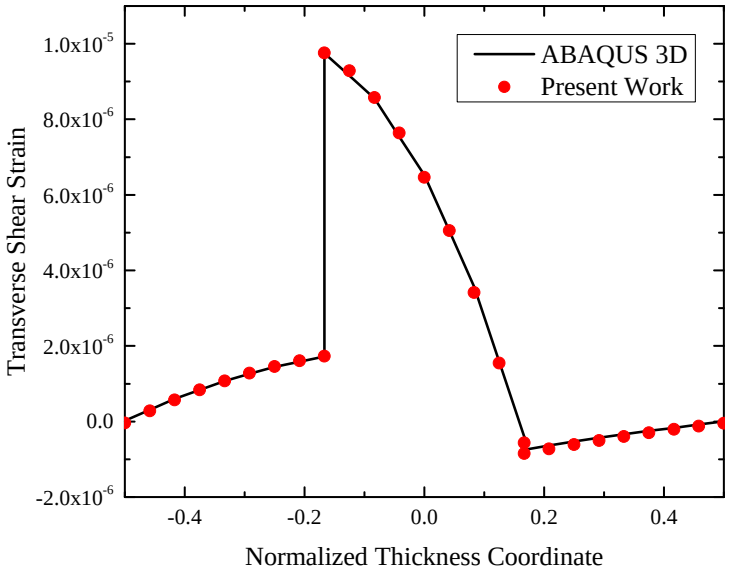

Figure 4.52. Distribution of strain Γ_{23} through thickness at $x_1 = 0.07$ m, $x_2 = 0.105$ m with combined load.

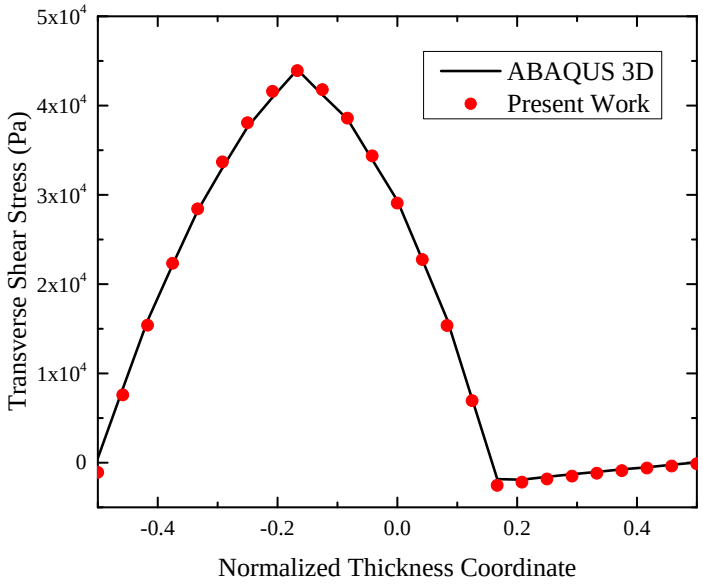

Figure 4.53. Distribution of stress σ_{23} through thickness at $x_1 = 0.07$ m, $x_2 = 0.105$ m with combined load.

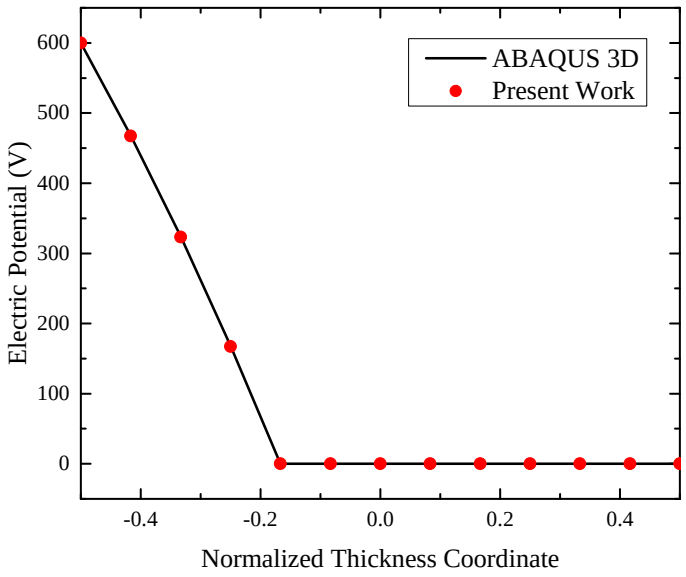

Figure 4.54. Distribution of electric potential ϕ through thickness at the center with combined load.

4.2.2 Example 2: Three-Layered Fixed Rectangular Plate

The plate analyzed in this example has the same geometry and layup as the one in the last example, while this time the plate has a fixed boundary condition. Because neither temperature change nor electric load will generate deflection on a undeformed fixed plate, a uniformly distributed mechanical load of 10kPa is applied downwards on the top surface along with the 600V electric potential on the bottom surface and 5K temperature change in the whole plate. Since it is not easy to obtain an analytical solution for a multi-layered anisotropic thick plate and the purpose of the present work is not solving 2D plate equations, finite element analysis using shell elements is applied to get the 2D solution. Since the first-order approximation model resembles the Reissner-Mindlin model, quadratic thick shell element S8R is adopted.

In finite element analysis using shell elements, fixed boundary condition is usually applied via constraining all six degrees of freedom (DOFs) to be zero at the boundary,

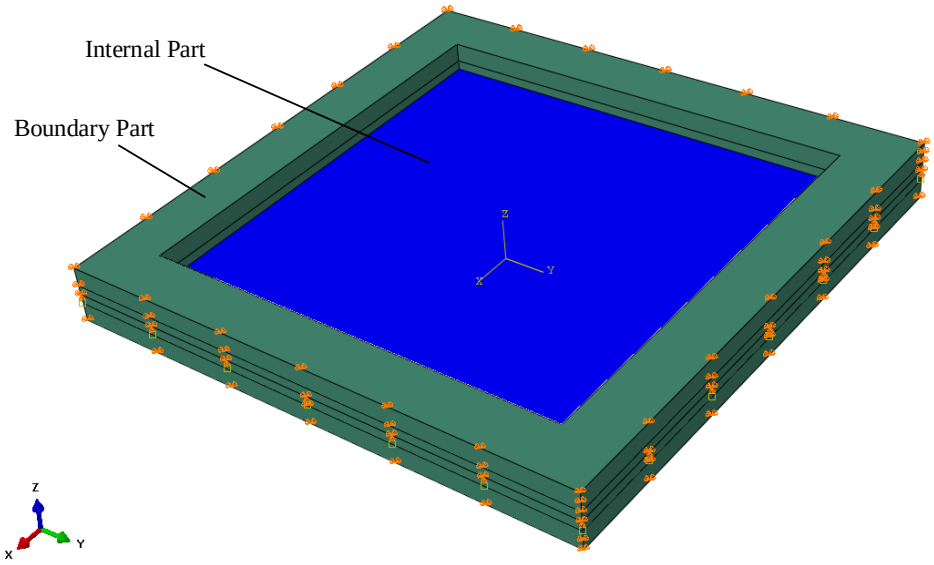

Figure 4.55. Boundary condition implementation of the fixed plate.

while in the 3D model used for comparison, as 3D continuum elements only have three DOFs, it is hard to define a completely equivalent fixed boundary conditions as the shell model. For best eliminating the effect of boundary condition, a model that divides the plate into a boundary part and an internal part is constructed, as shown in Figure 4.55. The boundary part, with the width of 14 mm, is modelled using 3D continuum elements, allowing the boundary condition of fixing three DOFs on the lateral faces to be the same as the 3D model. The internal part is modelled using shell elements, on which stiffness matrix obtained from the present theory is applied. Two parts are constrained using the solid to shell coupling. Totally there are 43200 C3D20RE elements in the boundary part and 6400 S8R elements in the internal part. Compare to 120000 elements in the 3D model with the same element size, the number is still much smaller. Results of deflection, 3D strains and stresses, and electric potential from the two part model are shown in Figures 4.56 to 4.66 with the counterparts from 3D model.

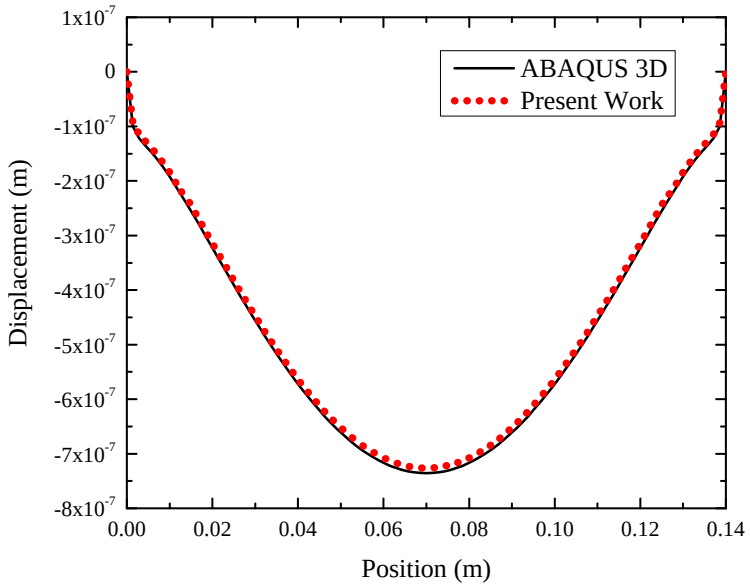

Figure 4.56. Deflection u_3 of the fixed plate along $x_2 = 0.07$ m.

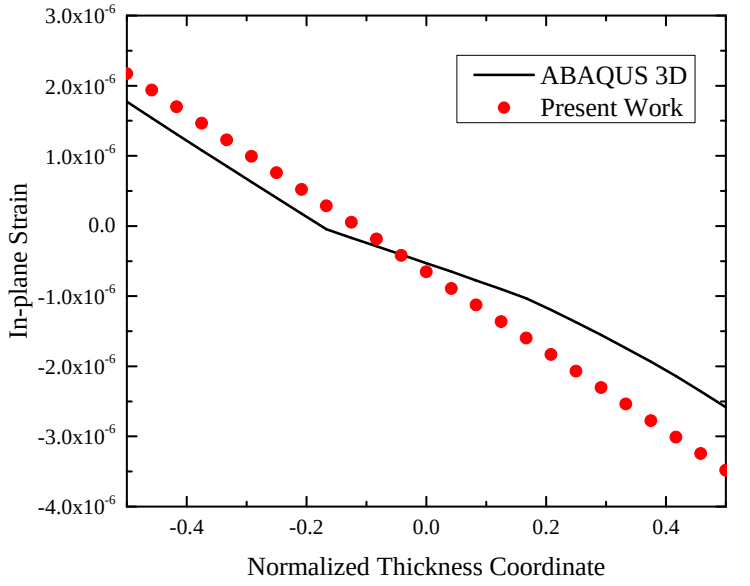

Figure 4.57. Distribution of strain Γ_{11} through thickness at the center.

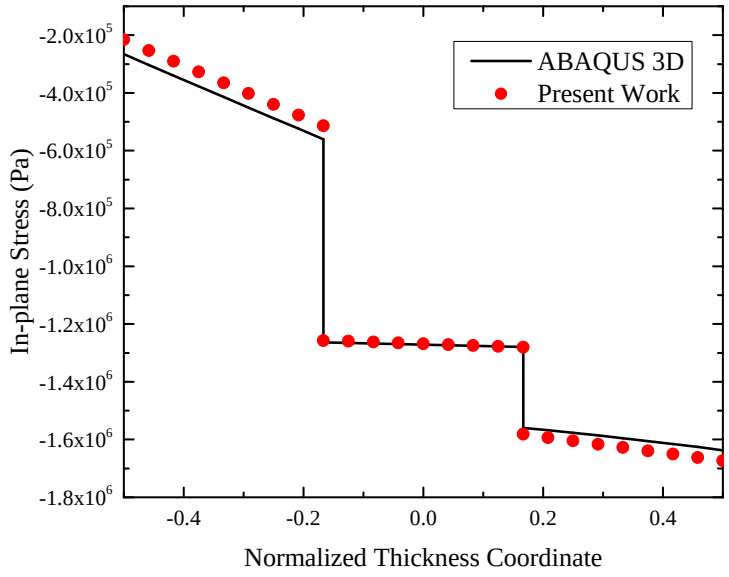

Figure 4.58. Distribution of stress σ_{11} through thickness at the center.

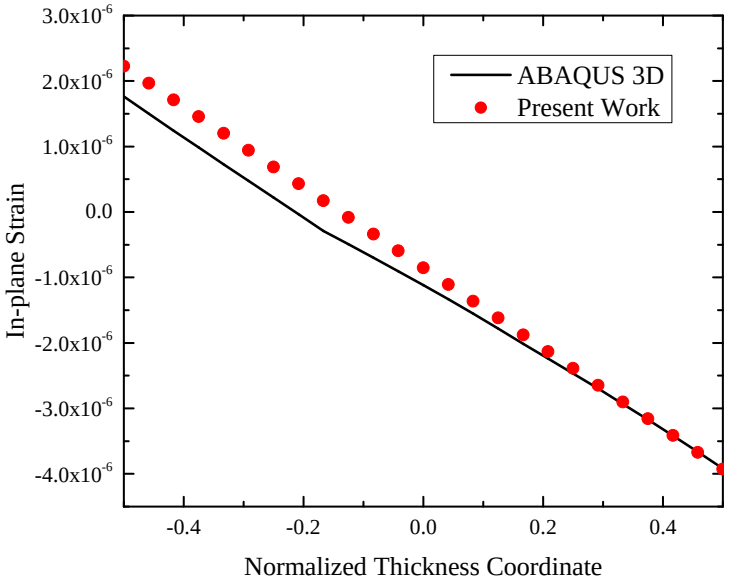

Figure 4.59. Distribution of strain Γ_{22} through thickness at the center.

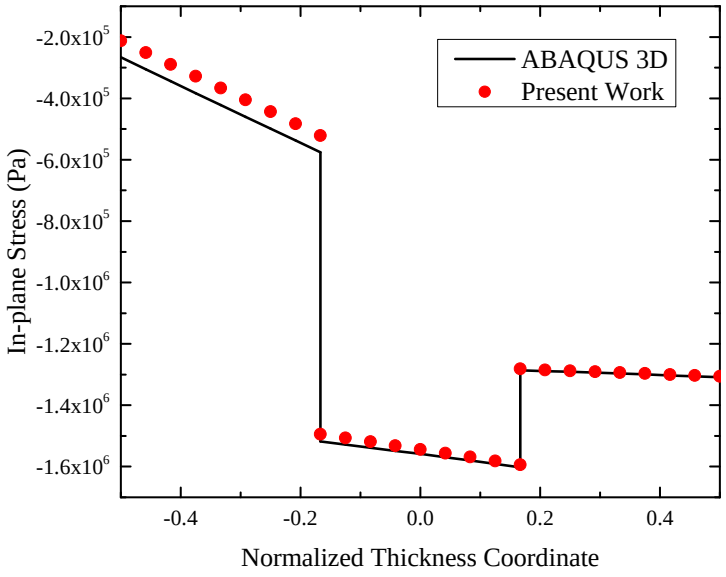

Figure 4.60. Distribution of stress σ_{22} through thickness at the center.

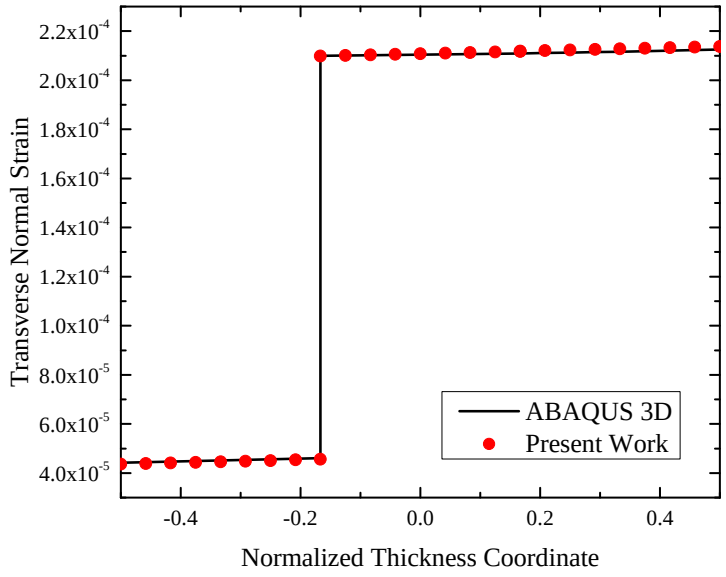

Figure 4.61. Distribution of strain Γ_{33} through thickness at the center.

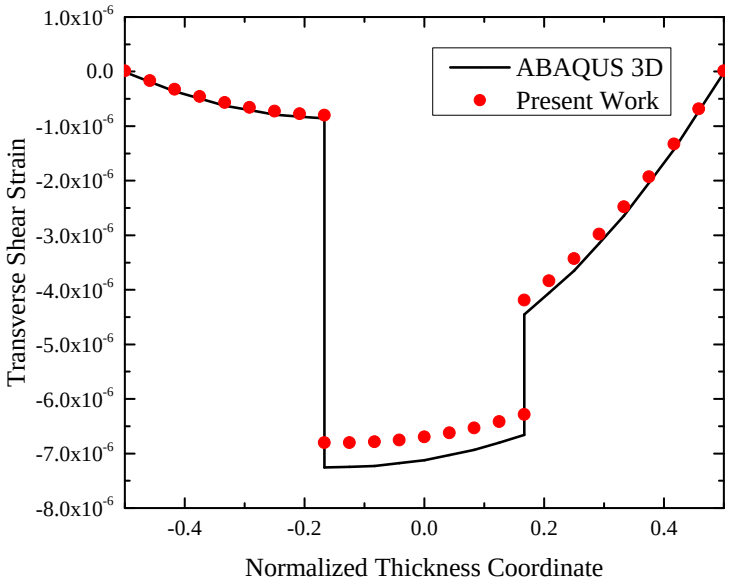

Figure 4.62. Distribution of strain Γ_{13} through thickness at $x_1 = 0.035$ m, $x_2 = 0.07$ m.

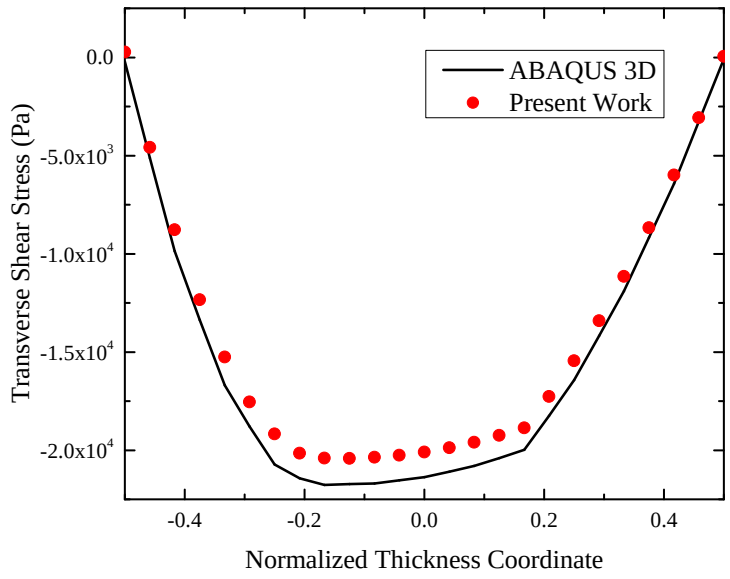

Figure 4.63. Distribution of stress σ_{13} through thickness at $x_1 = 0.035$ m, $x_2 = 0.07$ m.

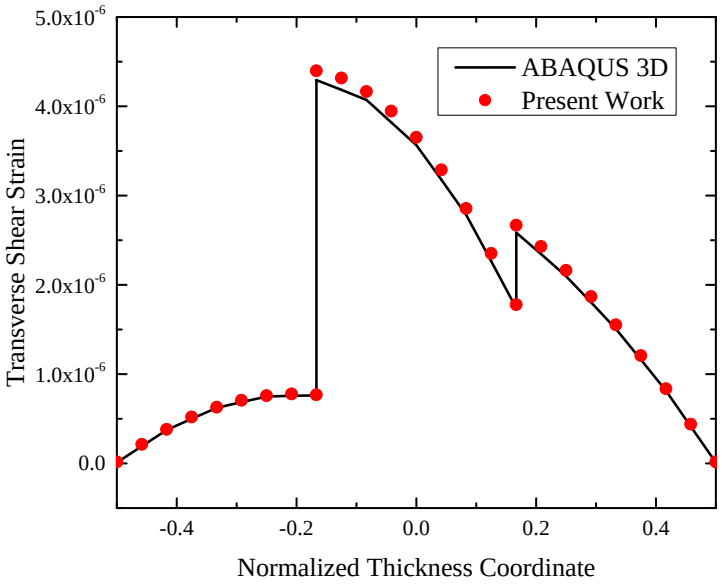

Figure 4.64. Distribution of strain Γ_{23} through thickness at $x_1 = 0.07$ m, $x_2 = 0.105$ m.

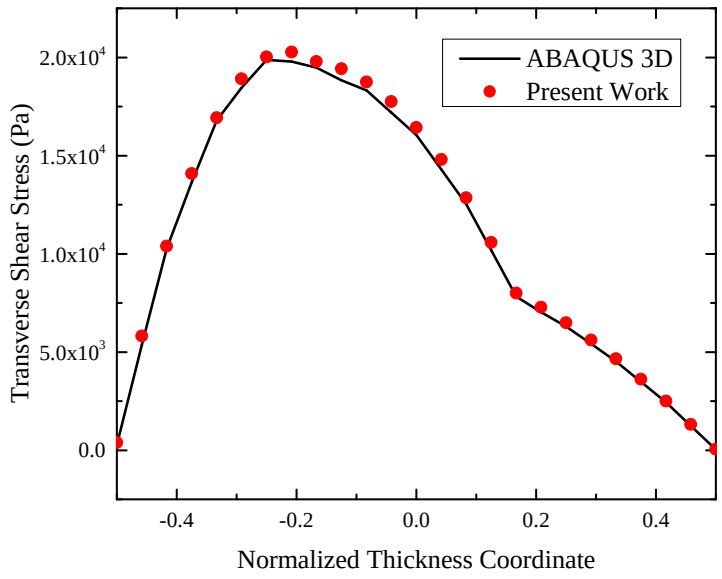

Figure 4.65. Distribution of stress σ_{23} through thickness at $x_1 = 0.07$ m, $x_2 = 0.105$ m.

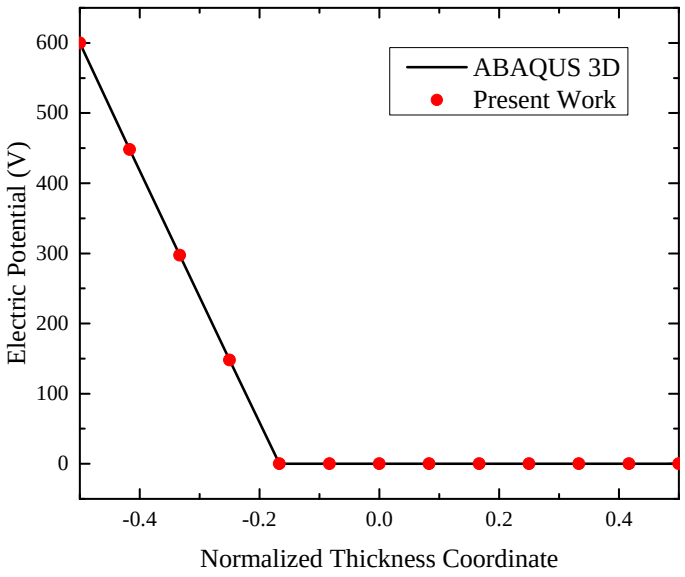

Figure 4.66. Distribution of electric potential ϕ through thickness at the center.

It can be observed from Figures 4.56 to 4.66 that for a fixed plate under distributed mechanical load, electric load and thermal load, the present work can still provide an accurate prediction for deflection, 3D strains and stresses and electric potential. However, from Figures 4.57 and 4.59, it can be seen that the accuracy of in-plane strains is worse than previous examples. This is caused by the limitation of the first-order model as in-plane strains up to this order are still linear distribution through the thickness while fixed boundary condition may lead the in-plane strains to distribute as higher order polynomials. If the strains are further expanded to the second-order, this defect can be largely overcome because in-plane strains up to the second-order contain cubic terms. Overall, the accuracy of the present work is better than widely used plate theories such as CLPT and FSDT, while still keeps a low computational cost compared to 3D finite element analyses.

5. Summary

In this thesis, in order to analyze multi-layered smart plates in engineering applications, a laminated anisotropic plate model with thermal expansion and piezoelectric effect is constructed based on the variational-asymptotic method. The main focus is on the interior constitutive model of the thermopiezoelastic plate. For modelling, the original 3D plate problem is separated into a 1D through the thickness analysis and a 2D reference surface analysis. Recovery of 3D fields using 2D plate solution is also made possible in the model. Following accomplishments are achieved during the study:

1. In formulating the 3D strain field, firstly warping functions are introduced to describe every possible shape in the deformed state. Based on this deformation configuration, 3D strains containing 2D generalized strains and partial derivatives of warping functions are obtained using the concept of decomposition of rotation tensor [47].

2. Based on the Hamilton's principle, total energy of the plate contains internal potential energy, kinetic energy and virtual work done by external loads. Specifically, the internal potential energy is expressed in terms of 3D strains, electric field described as derivatives of electric potential, and prescribed temperature change, along with material constants; the kinetic energy is deduced from time derivative of the deformation configuration; virtual work includes body force as well as surface tractions while loads on lateral boundaries are not considered.

3. Beginning from the energy expression, the dimensional reduction is implemented by first dropping terms asymptotically smaller than a certain order. Then, variation of the energy is taken to solve for warping functions and electric potential,

based on which equivalent constitutive relation of the plate can be derived. In this study, the warping functions are perturbed twice resulting a zeroth-order model and a first-order model. The zeroth-order model, resembling the CLPT in its form, is asymptotically correct and capable of recover the 3D in-plane strains and stresses as well as transverse normal strain that is assumed to be zero in the Kirchhoff-Love assumption. The first-order model is transformed into a Reissner-Mindlin like model with the price of losing the asymptotic correctness, while optimization ensures a minimum loss and the model is able to predict quadratic transverse shear deformation.

4. Several numerical examples are studied for validating both the zeroth-order model and the first-order model. The zeroth-order model is proved to have high fidelity when analyzing plates with a large aspect ratio and negligible transverse shear deformation. The first-order model can keep a good accuracy even though the aspect ratio of the plate goes smaller. Different laminations, plate shapes, boundary conditions and load combinations in the examples verify the robustness of the model.

It should be emphasized that the mathematical derivation of the present work follows a rigorous procedure that does not involves any ad hoc assumptions. Terms dropped in the current model are because of their smallness in order and will appear if the model is further derived into a higher order.

6. Recommendations

Although lots of theoretical derivation and numerical validation are implemented in this study, there are still many aspects that can be further developed in this topic.

1. In the validation of the zeroth-order approximation, a linear relation between 2D generalized strains and displacement is adopted for simplifying computation. However, plates with an aspect ratio so large such as a space reflector often deform into a state with small strain but large deflection, so adopting 2D nonlinear kinematics may provide a prediction closer to reality.

2. Though expressions are provided in chapter 3, examples for transverse normal stress are not available yet. Besides, layups in current examples are too simple compared with composite laminates in real applications. Examples with more complicated plate structures can be analyzed.

3. Current examples are all static problems, while dynamic and buckling problems of plates are also important topics especially for very thin plates. Case studies on these topics are necessary to verify the generality of the present work.

4. Thermal field in this study is prescribed and assumed to be unchanged during the deformation, but in space application, severe thermal environment makes it necessary to have a two-way coupling of the thermal field with electric field. In this case, temperature is changing when the plate is deformed and heat transfer problem should be considered. In addition, inverse effect of pyroelectricity should also be included, making the electric field generates a temperature change. Temperature field can be solved in a similar way as the elastic field in this work.

REFERENCES

REFERENCES

[1] Q. Luo and L. Tong. High precision shape control of plates using orthotropic piezoelectric actuators. *Finite Elements in Analysis and Design*, 42(11):1009–1020, 2006.

[2] K. Chandrashekhara and A. N. Agarwal. Active vibration control of laminated composite plates using piezoelectric devices: a finite element approach. *Journal of Intelligent Material Systems and Structures*, 4(4):496–508, 1993.

[3] H. Irschik. A review on static and dynamic shape control of structures by piezoelectric actuation. *Engineering Structures*, 24(1):5–11, 2002.

[4] R. Angel. Future very large space telescopes. In *AIAA Space 2000 Conference and Exposition*, 2000.

[5] C. G. Cassapakis, A. W. Love, and A. L. Palisoc. Inflatable space antennas-a brief overview. In *Aerospace Conference, 1998 IEEE*, volume 3, pages 453–459. IEEE, 1998.

[6] J. W. Martin, J. M. Redmond, P. S. Barney, T. D. Henson, J. C. Wehlburg, and J. A. Main. Distributed sensing and shape control of piezoelectric bimorph mirrors. *Journal of Intelligent Material Systems and Structures*, 11(10):744–757, 2000.

[7] A. K. Maji and M. A. Starnes. Shape measurement and control of deployable membrane structures. *Experimental Mechanics*, 40(2):154–159, 2000.

[8] M. J. Shepherd, R. G. Cobb, G. A. Peterson, and A. N. Palazotto. Quasi-static optics-based surface control of an in-plane actuated membrane mirror. *Journal of Spacecraft and Rockets*, 44(4):953–963, 2007.

[9] H. Fang, E. Im, U. O. Quijano, K. W. Wang, J. Hill, J. Moore, J. Pearson, C. Lui, and F. Djuth. High-precision adaptive control of large reflector surface. *Earth Science*, 2008, 2008.

[10] K. Patterson, S. Pellegrino, and J. Breckinridge. Shape correction of thin mirrors in a recongurable modular space telescope. In *Proc. SPIE 7731*, pages 773121–1, 2010.

[11] M. C. Ray, K. M. Rao, and B. Samanta. Exact analysis of coupled electroelastic behaviour of a piezoelectric plate under cylindrical bending. *Computers & Structures*, 45(4):667–677, 1992.

[12] J. S. Lee and L. Z. Jiang. Exact electroelastic analysis of piezoelectric laminae via state space approach. *International Journal of Solids and Structures*, 33(7):977–990, 1996.

[13] Z. Zhong and E. T. Shang. Three-dimensional exact analysis of a simply supported functionally gradient piezoelectric plate. *International Journal of Solids and Structures*, 40(20):5335–5352, 2003.

[14] K. Xu, A. K. Noor, and Y. Y. Tang. Three-dimensional solutions for coupled thermoelectroelastic response of multilayered plates. *Computer Methods in Applied Mechanics and Engineering*, 126(3):355–371, 1995.

[15] D. Ricketts. Model for a piezoelectric polymer flexural plate hydrophone. *The Journal of the Acoustical Society of America*, 70(4):929–935, 1981.

[16] C. K. Lee. Theory of laminated piezoelectric plates for the design of distributed sensors/actuators. part i: Governing equations and reciprocal relationships. *The Journal of the Acoustical Society of America*, 87(3):1144–1158, 1990.

[17] Q. Wang, S. T. Quek, C. T. Sun, and X. Liu. Analysis of piezoelectric coupled circular plate. *Smart Materials and Structures*, 10(2):229, 2001.

[18] I. M. N. Figueiredo and C. M. F. Leal. A piezoelectric anisotropic plate model. *Asymptotic Analysis*, 44(3):327–346, 2005.

[19] J. H. Huang and T. L. Wu. Analysis of hybrid multilayered piezoelectric plates. *International Journal of Engineering Science*, 34(2):171–181, 1996.

[20] Z. Q. Qu. An efficient modelling method for laminated composite plates with piezoelectric sensors and actuators. *Smart Materials and Structures*, 10(4):807, 2001.

[21] P. F. Pai, A. H. Nayfeh, K. Oh, and D. T. Mook. A refined nonlinear model of composite plates with integrated piezoelectric actuators and sensors. *International Journal of Solids and Structures*, 30(12):1603–1630, 1993.

[22] J. A. Mitchell and J. N. Reddy. A refined hybrid plate theory for composite laminates with piezoelectric laminae. *International Journal of Solids and Structures*, 32(16):2345–2367, 1995.

[23] J. N. Reddy. A simple higher-order theory for laminated composite plates. *Journal of Applied Mechanics*, 51(4):745–752, 1984.

[24] S. Kapuria and G. G. S. Achary. Nonlinear coupled zigzag theory for buckling of hybrid piezoelectric plates. *Composite Structures*, 74(3):253–264, 2006.

[25] S. Kapuria and G. G. S. Achary. Exact 3-D piezoelasticity solution for buckling of hybrid cross-ply plates using transfer matrices. *Acta Mechanica*, 170(1-2):25–45, 2004.

[26] R. G. Kepler and R. A. Anderson. Piezoelectricity and pyroelectricity in polyvinylidene fluoride. *Journal of Applied Physics*, 49(8):4490–4494, 1978.

[27] T. R. Tauchert. Piezothermoelastic behavior of a laminated plate. *Journal of Thermal Stresses*, 15(1):25–37, 1992.

[28] H. S. Tzou and R. Ye. Piezothermoelasticity and precision control of piezoelectric systems: theory and finite element analysis. *Journal of Vibration and Acoustics*, 116(4):489–495, 1994.

[29] M. Krommer and H. Irschik. A Reissner-Mindlin-type plate theory including the direct piezoelectric and the pyroelectric effect. *Acta Mechanica*, 141(1-2):51–69, 2000.

[30] M. Cho and J. Oh. Higher order zig-zag theory for fully coupled thermo-electric–mechanical smart composite plates. *International Journal of Solids and Structures*, 41(5):1331–1356, 2004.

[31] S. Kapuria and G. G. S. Achary. A coupled consistent third-order theory for hybrid piezoelectric plates. *Composite Structures*, 70(1):120–133, 2005.

[32] J. Oh, M. Cho, and J. S. Kim. Enhanced lower-order shear deformation theory for fully coupled electro-thermo-mechanical smart laminated plates. *Smart Materials and Structures*, 16(6):2229, 2007.

[33] S. Ueda. Thermally induced fracture of a piezoelectric laminate with a crack normal to interfaces. *Journal of Thermal Stresses*, 26(4):311–331, 2003.

[34] V. L. Berdichevskii. Variational-asymptotic method of constructing a theory of shells: Pmm vol. 43, no. 4, 1979, pp. 664–687. *Journal of Applied Mathematics and Mechanics*, 43(4):711–736, 1979.

[35] A. R. Atilgan and D. H. Hodges. On the strain energy of laminated composite plates. *International Journal of Solids and Structures*, 29(20):2527–2543, 1992.

[36] V. G. Sutyrin and D. H. Hodges. On asymptotically correct linear laminated plate theory. *International Journal of Solids and Structures*, 33(25):3649–3671, 1996.

[37] V. G. Sutyrin. Derivation of plate theory accounting asymptotically correct shear deformation. *Journal of Applied Mechanics*, 64(4):905–915, 1997.

[38] W. Yu. *Variational Asymptotic Modeling of Composite Dimensionally Reducible Structures*. PhD thesis, Georgia Institute of Technology, 2002.

[39] W. Yu, D. H. Hodges, and V. V. Volovoi. Asymptotic construction of Reissner-like composite plate theory with accurate strain recovery. *International Journal of Solids and Structures*, 39(20):5185–5203, 2002.

[40] D. H. Hodges, A. R. Atilgan, and D. A. Danielson. A geometrically nonlinear theory of elastic plates. *Journal of Applied Mechanics*, 60(1):109–116, 1993.

[41] W. Yu, D. H. Hodges, and V. V. Volovoi. Asymptotically accurate 3-D recovery from Reissner-like composite plate finite elements. *Computers & Structures*, 81(7):439–454, 2003.

[42] W. Yu and D. H. Hodges. A simple thermopiezoelastic model for smart composite plates with accurate stress recovery. *Smart Materials and Structures*, 13(4):926, 2004.

[43] L. Liao and W. Yu. Asymptotical construction of a fully coupled, Reissner–Mindlin model for piezoelectric composite plates. *Smart Materials and Structures*, 17(1):015010, 2008.

[44] L. Liao and W. Yu. An electromechanical Reissner–Mindlin model for laminated piezoelectric plates. *Composite Structures*, 88(3):394–402, 2009.

[45] H. Chen and W. Yu. A multiphysics model for magneto-electro-elastic laminates. *European Journal of Mechanics-A/Solids*, 47:23–44, 2014.

[46] D. A. Danielson. Finite rotation with small strain in beams and plates. In *Proceedings of the 2nd Pan American Congress of Applied Mechanics*, pages 2–4, 1991.

[47] D. A. Danielson and D. H. Hodges. Nonlinear beam kinematics by decomposition of the rotation tensor. *Journal of Applied Mechanics*, 54(2):258–262, 1987.

[48] J. N. Reddy. *Mechanics of Laminated Composite Plates and Shells: Theory and Analysis*. CRC press, 2004.

[49] V. L. Berdichevsky. *Variational Principles of Continuum Mechanics*. Springer, 2009.

[50] D. H. Hodges. Finite rotation and nonlinear beam kinematics. *Vertica*, 11(1/2):297–307, 1987.

[51] Y. Roh, V. V. Varadan, and V. K. Varadan. Characterization of all the elastic, dielectric, and piezoelectric constants of uniaxially oriented poled pvdf films. *Ultrasonics, Ferroelectrics, and Frequency Control, IEEE Transactions on*, 49(6):836–847, 2002.

[52] Q. Wang. *Asymptotic Multiphysics Modeling of Composite Beams*. PhD thesis, Utah State University, 2011.